SLAC-R-759

A Search for B+ -> tau+ nu tau Recoiling Against B- -> D0l- nu-l X

By Stephen Jacob Sekula

Ph.D. Thesis, University of Wisconsin, Madison

Stanford Linear Accelerator Center, Stanford University, Stanford, CA 94309

Work supported by Department of Energy contract DE–AC02–76SF00515.

A Search for $B^+ \to \tau^+ \nu_\tau$ Recoiling against $B^- \to D^0 \ell^- \bar{\nu}_\ell X$

by

Stephen Jacob Sekula

A dissertation submitted in partial fulfillment of the

requirements for the degree of

Doctor of Philosophy

(Physics)

at the

University of Wisconsin – Madison

2004

To Stephen and Annetta Sekula, who kept a smile on my face and joy in my heart.

Acknowledgments

This work would not be possible without years of support and help from many people whom I am proud to acknowledge. First, I would like to thank Professors Sau Lan Wu and Yibin Pan, who have given me endless support and guidance throughout my graduate career. Their dedication to physics has been a source of inspiration and affirmation.

I would also like to thank all the members of the Wisconsin *BABAR* group. You have all been a part of my life and especially of this work, and for that I cannot thank you enough. I would especially like to thank Mousumi Datta for the years of friendship and collaboration that led to a world-class search for $B^+ \to \tau^+\nu_\tau$ at *BABAR*.

I would also like to thank all the members of the *BABAR* collaboration, whose expertise built the experiment, ran the experiment, and produced world-class physics data and results. I would like to especially thank the conveners of the Leptonic Bottom and Charm working group, Gregory Dubois-Felsmann, Steve Robertson, and Rafe Schindler for their years of input and support. I'd also like to thank the members of the working group, too numerous to mention here. Know that each of you was and still is important to this work. I would like to thank the members of the committee which has tirelessly reviewed this work for *BABAR*: Dieter Best, Fabrizio Bianchi, Homer Neal, and Eli Rosenberg. I would also like to thank Gerry Abrahms for his guidance when this analysis was first developed, and Paul Jackson for his tireless devotion to semi-leptonic B reconstruction.

With all my heart I would like to thank my parents, Stephen and Annetta Sekula, and my sister, Katherine Sekula. They have always supported me in everything, and in this work I hope they find the product of all the delight and difficulty of raising me. My hopes and dreams have always been numerous, and they kept me to each and every one.

Finally, I would like to thank my wife, Jodi Cooley, whose love, friendship, support, and devotion are beyond description.

Contents

List of Tables

List of Figures

Chapter 1

Introduction

The fundamental pursuit of physics has always been a deeper understanding of nature's workings. In the last fifty years this pursuit has culminated in a view of the universe as a complex tapestry woven from only a few fundamental particles and interactions. This description of the universe, the *Standard Model of Particle Physics*, has been highly successful at predicting the behavior of these particles and interactions. However, the model leaves many questions unanswered and the hope is that many precise tests of its predictions will yield inconsistencies, windows into new physical principles. The search for processes that are allowed by the Standard Model but inherently rare provides fruitful ground for such a test. The large sample of B mesons available from the PEP-II/*BABAR* B-factory furnishes an opportunity to test Standard Model predictions via rare B meson decay modes.

1.1 The Standard Model

The Standard Model of Particle Physics is an excellent description of nature at the level of its building blocks. The model uses quantum field theory to describe the behavior of the known fundamental particles and forces. The Standard Model was developed by Glashow, Weinberg and Salam [1][2][3]. It describes the behavior of fermionic fields that represent the known building blocks of the universe: leptons and quarks. For unknown reasons there are three generations of quarks and leptons. These fermions and their properties are summarized in Table 1.1.

The gauge symmetry $SU(3) \otimes SU(2) \otimes U(1)$ describes the interactions experienced by quarks and leptons. The $SU(3)$ group represents the strong interaction mediated by eight gluons, g [1]. The $SU(2) \otimes U(1)$ group represents the weak interaction and electromagnetism as a single, unified *electroweak interaction*. This interaction is mediated by three massive vector bosons ($W^{\pm}$ and Z^0) and the massless photon (γ) [2].

1.1.1 Fermions and the Weak Interaction

For this work, a discussion of the behavior of the quarks in the context of the weak interaction is useful. The weak interaction couples quarks and leptons with a strength given by the Fermi constant, $G_F = 1.16639 \times 10^{-5}\,\mathrm{GeV}^{-2}$. However,

[1] The theory of the strong interaction is known as Quantum Chromodynamics, or QCD

[2] Gravity, the fourth and weakest of the known interactions, is not described by the Standard Model.

Table 1.1: The properties of the quarks and leptons. Each of these particles has a corresponding antiparticle of opposite charge. The masses of the quarks are difficult to determine because the quarks exist only in bound states and not as free particles. The top quark mass has been measured precisely because it decays before it can form a bound state with another quark.

QUARKS			
Particle Name	Symbol	Electric Charge	Mass (GeV/c^2) [4]
up	u	$+\frac{2}{3}$	0.0015 to 0.0045
down	d	$-\frac{1}{3}$	0.005 to 0.0085
charm	c	$+\frac{2}{3}$	1.0 to 1.4
strange	s	$-\frac{1}{3}$	0.080 to 0.155
top	t	$+\frac{2}{3}$	174.3 ± 5.1
bottom	b	$-\frac{1}{3}$	4.0 to 4.5

LEPTONS			
Particle Name	Symbol	Electric Charge	Mass (MeV/c^2) [4]
electron	e	-1	0.510999
electron neutrino	ν_e	0	< 0.000003
muon	μ	-1	105.658
muon neutrino	ν_μ	0	< 0.19
tau	τ	-1	$1776.99^{+0.29}_{-0.26}$
tau neutrino	ν_τ	0	< 18.2

in order to accomodate couplings between quarks from different generations it is necessary to postulate that the eigenstates of the weak interaction are not the same as the mass eigenstates. The general assumption can be made that the mass and weak eigenstates of all quarks are not the same. However the phases of the quark wavefunctions, which are not observable, can always be adjusted in such a way as to simplify this assumption. The simplification leads to the postulate that only the down-type quarks (d,s,b) have different weak and mass eigenstates. The weak eigenstates are denoted (d', s', b') while the mass eigenstates are denoted

(d, s, b). The relationship between the two sets of eigenstates is described by a unitary 3×3 matrix which was developed by N. Cabibbo, M. Kobayashi and T. Maskawa and is known as the *CKM matrix* [5][6]. The matrix is defined by the relationship

$$\begin{pmatrix} d' \\ s' \\ b' \end{pmatrix} = \begin{pmatrix} V_{ud} & V_{us} & V_{ub} \\ V_{cd} & V_{cs} & V_{cb} \\ V_{td} & V_{ts} & V_{tb} \end{pmatrix} \begin{pmatrix} d \\ s \\ b \end{pmatrix} \equiv V_{CKM} \begin{pmatrix} d \\ s \\ b \end{pmatrix}. \tag{1.1}$$

A 3×3 unitary matrix has four free parameters. One useful parameterization of this matrix was developed by L. Wolfenstein [7]. Due to the small value of $|V_{us}| = 0.22$, the matrix can be Taylor expanded in terms of $\lambda = |V_{us}|$ as follows:

$$V_{CKM} = \begin{pmatrix} (1 - \frac{\lambda^2}{2}) & \lambda & A\lambda^3(\rho - i\eta) \\ -\lambda & (1 - \frac{\lambda^2}{2}) & A\lambda^2 \\ A\lambda^3(1 - \rho - i\eta) & -A\lambda^2 & 1 \end{pmatrix} + \mathcal{O}(\lambda^4) \tag{1.2}$$

To excellent accuracy [3] the four parameters ρ, η, A and λ are related to the matrix elements in 1.1 by

$$V_{us} = \lambda, \qquad V_{cb} = A\lambda^2, \tag{1.3}$$

$$V_{ub} = A\lambda^3(\rho - i\eta), \quad V_{td} = A\lambda^3(1 - \rho - i\eta) \tag{1.4}$$

The assumption that the weak and mass eigenstates of the leptonic sector are not identical can also be made. However, the near masslessness of the neutrinos constrains the leptonic CKM matrix to be a unit matrix.

Determining the accuracy with which the Standard Model describes nature requires careful study of the particles and interactions both theoretically and

[3] The Wolfenstein approximation has a precision which is of the same order as current experimental uncertainties in the CKM parameters relevant to B meson physics.

experimentally. In particular, mesons are excellent systems in which to study the interplay of the quarks and the strong, weak and electromagnetic interactions. The B-meson ($B^+ = (\bar{b}u)$, $B^0 = (\bar{b}d)$) provides rich opportunities for such study. Its large mass ($5.279\,\mathrm{GeV}/c^2$), compared to the masses of other mesons, allows for a large number of final states into which it can decay. These final states can be sensitive to the internal dynamics of the B meson and thus the roles of the fundamental interactions.

A complete understanding of the B meson's internal structure has been limited in several ways. From the theoretical viewpoint, the structure of the meson has uncertainties due to the difficulty of treating the strong interaction perturbatively. While there exist theoretically cleaner decay modes of the B meson, they are often extremely rare, occuring in less than 0.01% of all B decays. From the experimental viewpoint, there has been a limited number of available B mesons. This fact makes many of the rarer decay modes difficult or impossible to access.

Recently, the PEP-II/*BABAR* B-factory at the Stanford Linear Accelerator Center (SLAC) and the KEKB/Belle B-factory at the KEK[4] laboratory in Japan have produced large numbers of B mesons. Consequently, there is an opportunity to pursue rare decays which are essentially free of theoretical uncertainty. This allows for predictions of the Standard Model to be directly compared to experimental observation.

[4]Translated, KEK stands for "The High Energy Accelerator Research Organization".

1.2 The Rare Decay $B^+ \to \ell^+ \nu_\ell$

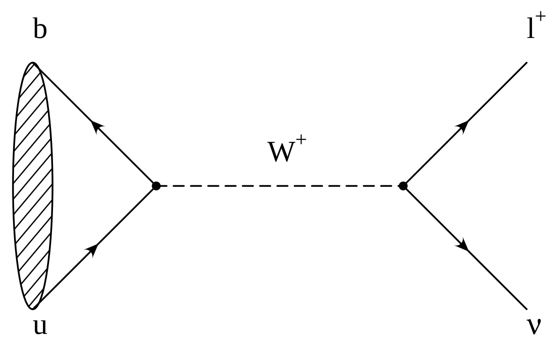

Figure 1.1: The Standard Model description of the decay $B^+ \to \ell^+ \nu_\ell$

One specific set of B meson decay modes which are relatively free of large theoretical uncertainties are of the form $B^+ \to \ell^+ \nu_\ell$, where the $\bar{b}$ and d quarks annihilate into a W^+ boson, which then produces a pair of leptons. One of the leptons is a neutrino and the other (ℓ^+) is either an electron, muon or tau. The primary diagram that illustrates this decay is shown in Figure 1.1. Though this process is allowed in the Standard Model, it is suppressed by helicity conservation and has never been observed. The calculation of the branching fraction in the Standard Model framework is given in the next section.

1.3 The Branching Fraction for $B^+ \to \ell^+ \nu_\ell$

In the Standard Model, the decay of the B^+ meson into $\ell^+ \nu_\ell$ is mediated by the weak interaction. The general form of the amplitude of this process is

$$\mathcal{M} = \frac{4G_F}{\sqrt{2}} \mathcal{J}^{\mu}_{(bu)} \mathcal{J}^{(\ell\nu)}_{\mu}, \tag{1.5}$$

where $\mathcal{J}^{\mu}_{(bu)}$ is the current describing the decay of the meson and $\mathcal{J}^{(\ell\nu)}_{\mu}$ is the current describing the production of the leptons. The b and u quarks cannot be treated independently, since they are bound in a meson. The spin-0 nature of the B^+ meson constrains $\mathcal{J}^{\mu}_{(bu)}$ to have a contribution only from the momentum of the meson. Given these restrictions, the quark current can be written

$$\mathcal{J}^{\mu}_{(bu)} = \frac{1}{2} q^{\mu} f(q^2) V_{ub}. \tag{1.6}$$

Since $q^2 = m^2_{B^+}$, $f(q^2)$ is frame-invariant and a constant of the meson, denoted simply f_B. The lepton current can be written as follows

$$\mathcal{J}^{(\ell\nu)}_{\mu} = \frac{1}{2} \bar{u}(p)\gamma_{\mu}(1-\gamma_5)v(k) \tag{1.7}$$

where $\bar{u}(p)$ is the particle spinor for the up-quark, $v(k)$ is the anti-particle spinor for the neutrino, γ_μ is the Dirac gamma matrix, and γ^5 is the product of Dirac gamma matrices, $\gamma^5 = \gamma^0\gamma^1\gamma^2\gamma^3\gamma^4$.

Thus, the full expression for the amplitude of the process in Fig. 1.1 is

$$\mathcal{M} = \frac{G_F}{\sqrt{2}} f_B V_{ub} (p^{\mu} + k^{\mu}) \bar{u}(p)\gamma_{\mu}(1-\gamma_5)v(k), \tag{1.8}$$

where the substitution by momentum conservation $q^{\mu} = p^{\mu} + k^{\mu}$ has been made. The Dirac equations of motion for the lepton and neutrino supply the following constraints,

$$\begin{aligned} \bar{u}(p)(p^{\mu}\gamma_{\mu} - m_{\ell}) &= 0 \qquad (1.9) \\ k^{\mu}\gamma_{\mu}v(k) &= 0 \qquad (1.10) \end{aligned}$$

which then simplify the amplitude,

$$\mathcal{M} = \frac{G_F}{\sqrt{2}} f_B V_{ub} m_\ell \bar{u}(p)\gamma_\mu(1-\gamma_5)v(k). \tag{1.11}$$

In the B meson's rest frame, the decay rate can be written as

$$d\Gamma = \frac{1}{2m_{B^-}}|\bar{\mathcal{M}}|^2 \frac{d^3p}{(2\pi)^3 2E}\frac{d^3k}{(2\pi)^3 2\omega}(2\pi)^4\delta(q-p-k) \tag{1.12}$$

where E and ω are defined by $p = (\vec{p}, E)$ and $k = (\vec{k}, \omega)$ and $\delta(q-p-k)$ is a four-dimensional Dirac delta function. Averaging over the final spins and applying the trace theorems yields the following expression for $|\bar{\mathcal{M}}|^2$:

$$|\bar{\mathcal{M}}|^2 = 4G_F^2 f_B^2 |V_{ub}|^2 m_\ell^2 (p\cdot k). \tag{1.13}$$

The width of the B meson can then be found by integrating over the four-momenta of the final state particles,

$$\Gamma = \frac{G_F^2 f_B^2 |V_{ub}|^2 m_\ell^2}{(2\pi)^2 2m_{B^-}} \int \frac{d^3p d^3k}{E\omega}\delta(m_{B^-} - E - \omega)\, \delta^{(3)}(\vec{k}+\vec{p})\, \omega(E+\omega) \tag{1.14}$$

where the substitution $\vec{p} = -\vec{k} \to (p\cdot k) = \omega(E+\omega)$ has been made and the Dirac delta function has been broken into a delta function in energy and in momentum. The integral over $\vec{p}$ is trivial, since it is just an integral over a delta function. The integral over $\vec{k}$ is simplified by the fact that the decay exhibits no angular dependence. The remaining integration,

$$\Gamma = \frac{4\pi G_F^2 f_B^2 |V_{ub}|^2 m_\ell^2}{(2\pi)^2 2m_{B^-}} \int \omega^2 d\omega (1 + \frac{\omega}{E})\delta(m_{B^-} - E - \omega), \tag{1.15}$$

is performed by using the identity $\delta(f(x)) = \sum_i \delta(x)/|\frac{\partial f}{\partial x}|_{x=x_i}$, where the x_i are the zeros of the function $f(x)$. The branching fraction, the relative rate at which the B meson decays to $\ell^+\nu_\ell$, is defined as

$$\mathcal{B}(B^+ \to \tau^+\nu_\tau) \equiv \Gamma/\Gamma_{total} = \frac{G_F^2 f_B^2 |V_{ub}|^2 m_{B^+}^3 \tau_{B^+}}{8\pi} \frac{m_{\ell^+}^2}{m_{B^+}^2}[1 - \frac{m_{\ell^+}^2}{m_{B^+}^2}]^2 \qquad (1.16)$$

All the parameters in 1.16 are well known except f_B, which has never been directly measured, and $|V_{ub}|$, which though measured has a large uncertainty. A precise measurement of $|V_{ub}|$ and a measurement of $\mathcal{B}(B^+ \to \tau^+\nu_\tau)$ will allow for the extraction of f_B from Equation 1.16.

The mechanism by which this process is suppressed in the Standard Model is clear from Equation 1.16. The ratio m_ℓ/m_{B^+} expresses the *helicity supression* of the process.

Of the three possible final states ($B^+ \to e^+\nu_e, \mu^+\nu_\mu, \tau^+\nu_\tau$) the process $B^+ \to \tau^+\nu_\tau$ is selected for study in the present work. This is because it is the least helicity suppressed of the three leptonic final states. It is thus the most accessible of these final states at existing experimental facilities. Compared to $\tau^+\nu_\tau$, $\mu^+\nu_\mu$ and $e^+\nu_e$ are suppressed by factors of 300 and 10^7, respectively. Despite the experimental challenges of a number of undetectable neutrinos in the final state, a search for this decay mode holds great promise with the existing data set at the PEP-II/*BABAR* B factory.

1.3.1 Standard Model Estimate of the Branching Fraction

The parameters in equation 1.16 and their current experimental or theoretical values and uncertainties are given in Table 1.2. Inserting these values into Equation 1.16 and propagating the errors from the two dominant sources ($|V_{ub}|$

Table 1.2: The values and relative uncertainties of the parameters that enter into the Standard Model branching fraction calculation. The values are taken from [4].

Parameter	Value	Uncertainty (%)	Known From...
$\lvert V_{ub}\rvert$	3.6×10^{-3}	19.4440	Experiment
f_B	0.198 GeV	15.1520	Theory
B^+ lifetime	$2.54 \times 10^{12}\,\mathrm{GeV}^{-1}$	1.0753	Experiment
τ^+ Mass	1.77699 GeV	0.0155	Experiment
B^+ Mass	5.2790 GeV	0.0095	Experiment
G_F	$1.16639 \times 10^{-5}\,\mathrm{GeV}^{-2}$	0.0009	Experiment

and f_B) yields a Standard Model estimate of the central value and its uncertainty,

$$\mathcal{B}(B^+ \to \tau^+\nu_\tau) = (0.92 \pm 0.45) \times 10^{-4} \tag{1.17}$$

1.3.2 Numerical Branching Fraction Estimate

It is instructive to evaluate the branching fraction numerically to see its distribution in a large number of toy experiments. It is assumed that in a large number of toy experiments the values of the input parameters would be normally distributed about their means. One million such "experiments" are generated and the distribution of the branching fraction is shown in Fig. 1.2. From this the mean value of the branching fraction is determined to be 0.97×10^{-4}, but the distribution spans an order of magnitude. The point below which 68.3% of the experiments lie is 1.1×10^{-4}. Integrating the number of possibilites lying above 1.0×10^{-4}, there is a 40% probability that the value of the branching fraction lies in that region. There is only a 3.6% probability that the value lies above

2.0×10^{-4}.

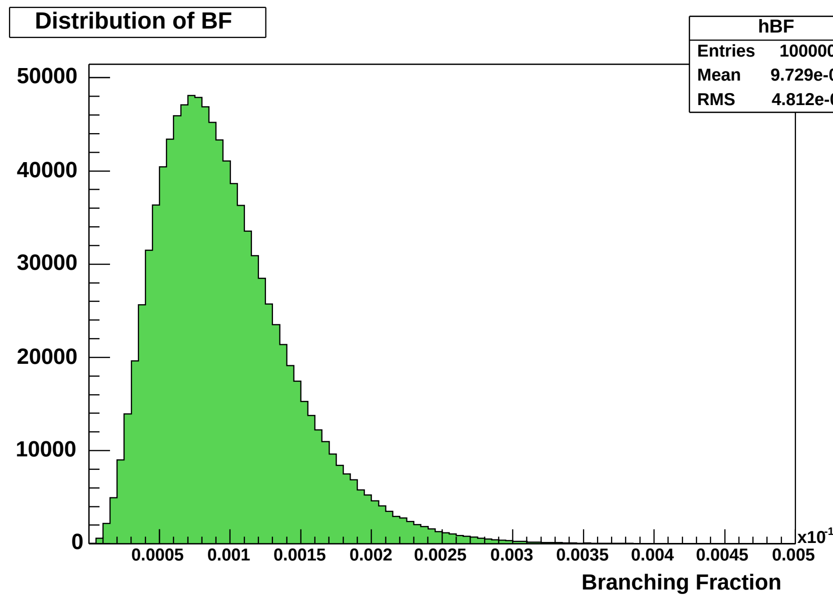

Figure 1.2: The distribution of the Standard Model branching fraction prediction for one million toy experiments, where for each experiment the values of f_B, $|V_{ub}|$, and the B^+ lifetime are Gaussian fluctuated by their uncertainties about their means.

1.3.3 Previous Searches for $B^+ \to \tau^+\nu_\tau$

Several experiments have conducted searches for $B^+ \to \tau^+\nu_\tau$. These include DELPHI, L3, and ALEPH at the Large Electron-Positron (LEP) collider and CLEO at the Cornell Electron Storage Rings (CESR). The results of these searches are summarized in Table 1.3.

The search using the ALEPH detector at LEP searched for $B^+ \to \tau^+\nu_\tau$ by reconstructing events as $e^+e^- \to Z^0 \to b\bar{b}$. Given the large center-of-mass energy at LEP, the b quarks would tend to form back-to-back jets of particles. The analysis divided the event into two hemispheres along the jet axis. The energy

Table 1.3: The results of other searches for $B^+ \to \tau^+\nu_\tau$. No experiment has ever observed $B^+ \to \tau^+\nu_\tau$ and only limits have been set on its branching fraction.

Experiment	Limit on $\mathcal{B}(B^+ \to \tau^+\nu_\tau)(\times 10^{-4})$
ALEPH	< 18 (90% CL) [8]
DELPHI	< 11 (90% CL) [9]
CLEO	< 8.4 (90% CL) [10]
L3	< 5.7 (90% CL) [11]

in one hemisphere was required to be half the Z^0 mass. In the other hemisphere, a single lepton or no lepton (from $\tau^+ \to \ell^+\nu_\ell\overline{\nu}_\tau$ or $\tau^+ \to hadrons + \overline{\nu}_\tau$) was required, with energy and momentum consistent with the expected signal process. This analysis had large backgrounds from $Z^0 \to q\overline{q}$ and $b\overline{b}, c \to (e^+, \mu^+)\nu X$. This search at ALEPH obtained a limit of $\mathcal{B}(B^+ \to \tau^+\nu_\tau) < 1.8 \times 10^{-3}$ at the 90% confidence level (CL).

The L3 and DELPHI experiments searched for $B^+ \to \tau^+\nu_\tau$ using the same expeimental method as ALEPH. They set 90% confidence level limits on its branching fraction at 5.7×10^{-4} and 1.1×10^{-3}, respectively.

The search using the CLEO detector at CESR started with a sample of 10 million $B\overline{B}$ events. It then proceeded by reconstructing one of the two B mesons in an event as $B^- \to D^{(*)0}(n\pi^-)$. They then tried to determine if the second B meson decayed as $B^+ \to \tau^+\nu_\tau$ via either $\tau^+ \to \ell^+\nu_\ell\overline{\nu}_\tau$ or $\tau^+ \to \pi^+\overline{\nu}_\tau$. This search yielded an upper limit of $\mathcal{B}(B^+ \to \tau^+\nu_\tau) < 8.4 \times 10^{-4}$ at the 90% confidence level.

The present work uses the experimental facilities at the PEP-II/*BABAR* B-Factory to search for $B^+ \to \tau^+\nu_\tau$. While CESR also collided electrons and positrons and produced pairs of B mesons, the B-Factory operates at a higher luminosity and accelerates the electrons and positrons to different energies. The asymmetric collision energies Lorentz boosts the resulting B mesons in the detector's reference frame. The result of these two key differences is that the B-Factory has a much larger sample of B mesons (90 million) which have traveled from their point of origin, making them more easily resolvable.

1.4 The Importance of $B^+ \to \ell^+\nu_\ell$

There are several reasons to pursue a measurement of the branching fraction for $B^+ \to \tau^+\nu_\tau$. The most straight-forward reason to search for this process is simply that it has never been observed. However, a measurement or limit on the branching fraction contributes other benefits. The branching fraction can be combined with other B meson properties to place indirect constraints on parameters in the Standard Model. The example given in 1.4.1 is the use of the branching fraction and B meson mixing measurements to constrain the CKM matrix. Additionally, $B^+ \to \tau^+\nu_\tau$ is potentially sensitive to new physics which could enhance or suppress its branching fraction. The example given in 1.4.2 uses SuperSymmetry to illustrate how new physics can be constrained using a measurement or limit on the branching fraction.

The other leptonic final states, $B^+ \to \mu^+\nu_\mu$ and $B^+ \to e^+\nu_e$ can also be used to help constrain the Standard Model. Since $B^+ \to \tau^+\nu_\tau$ is the focus of the present work it will be used as an example in the following sections.

1.4.1 Constraints from $B^+ \rightarrow \tau^+\nu_\tau$ and B mixing on the Wolfenstein $\bar{\rho}-\bar{\eta}$ plane

In addition to providing information about the B meson decay constant, a branching fraction measurement can be used together with B mixing results to obtain constraints on the Wolfenstein $\bar{\rho}-\bar{\eta}$ plane. The mass difference between the heavy-light B_d meson states, measured with high precision [12][13], is calculated in the Standard Model to be

$$\Delta m_d = \frac{{G_F}^2}{6\pi^2} \cdot \eta_B \cdot m_B \cdot m_W^2 \cdot {f_B}^2 \cdot \hat{B}_B \cdot S_0(x_t)|V_{td}|^2. \tag{1.18}$$

In 1.18, the following terms arise from QCD contributions to the B mixing process:

- $\hat{B}_B$ is the "Bag Parameter", a quantity which arises from applying renormalization to the perturbation theory expansion of the QCD contributions.
- η_B is the QCD correction factor that depends on Λ_{QCD} and the masses of the top and bottom quark. Here, η_B is given by 0.55 ± 0.01 [14].
- $S_0(x_t)$ is the Inami-Lin function [15]. Here, $x_t \equiv m_t^2/M_W^2$ and $S_0(x_t) \equiv 2.46 \left(\frac{m_t}{170\,\mathrm{GeV}}\right)^{1.52} \approx 4.$

While the $B^+ \rightarrow \tau^+\nu_\tau$ branching fraction equation and the above heavy-light mass difference both depend on f_B, their ratio does not. The ratio is

$$\frac{\mathcal{B}(B^+ \rightarrow \tau^+\nu_\tau)}{\Delta m_d} = \frac{|V_{ub}|^2}{|V_{td}|^2}\left(\frac{3\pi}{4}\frac{\tau_B \cdot m_\tau^2 \cdot \left[1-\frac{m_\tau^2}{m_B^2}\right]^2}{\eta_B \cdot m_W^2 \cdot B_B \cdot S_0(x_t)}\right) = \frac{|V_{ub}|^2}{|V_{td}|^2} \cdot A, \tag{1.19}$$

Table 1.4: The values of the QCD parameters used in Fig. 1.3.

QCD Parameter	Value
$\hat{B}_B$	1.34 ± 0.03
η_B	0.55 ± 0.01
$S_0(x_t)$	3.9 ± 0.11

where A contains all of the non-CKM terms in the expression. This equation can be re-written in the context of the Wolfenstein parameterization of the CKM matrix:

$$\frac{\mathcal{B}(B^+ \to \tau^+\nu_\tau)}{\Delta m_d} = \left(\frac{\bar{\rho} - i\bar{\eta}}{1 - \bar{\rho} - i\bar{\eta}}\right)^2 \cdot \frac{1}{(1-\lambda^2/2)} \cdot A \tag{1.20}$$

For the branching fraction limit obtained by the L3 experiment ($\mathcal{B}(B^+ \to \tau^+\nu_\tau) < 5.7 \times 10^{-4}$), the allowed region in the Wolfenstein $\bar{\rho} - \bar{\eta}$ plane is given in Fig. 1.3. The constraints obtained from this previous measurement are compatible with other constraints on the plane derived from other measurements. The QCD parameters and their values used in this figure are given in Table 1.4.

1.4.2 Constraints from $B^+ \to \tau^+\nu_\tau$ on SuperSymmetry

While the description of $B^+ \to \tau^+\nu_\tau$ has so far been in the context of the Standard Model, physics due to processes outside the model may affect the branching fraction. SuperSymmetry is one example of new physics and is used here to explore effects on $B^+ \to \tau^+\nu_\tau$.

The Standard Model mediates the process $B^+ \to \tau^+\nu_\tau$ via a W^+ boson. If supersymmetry (SUSY) is an allowed symmetry of nature, then there is the

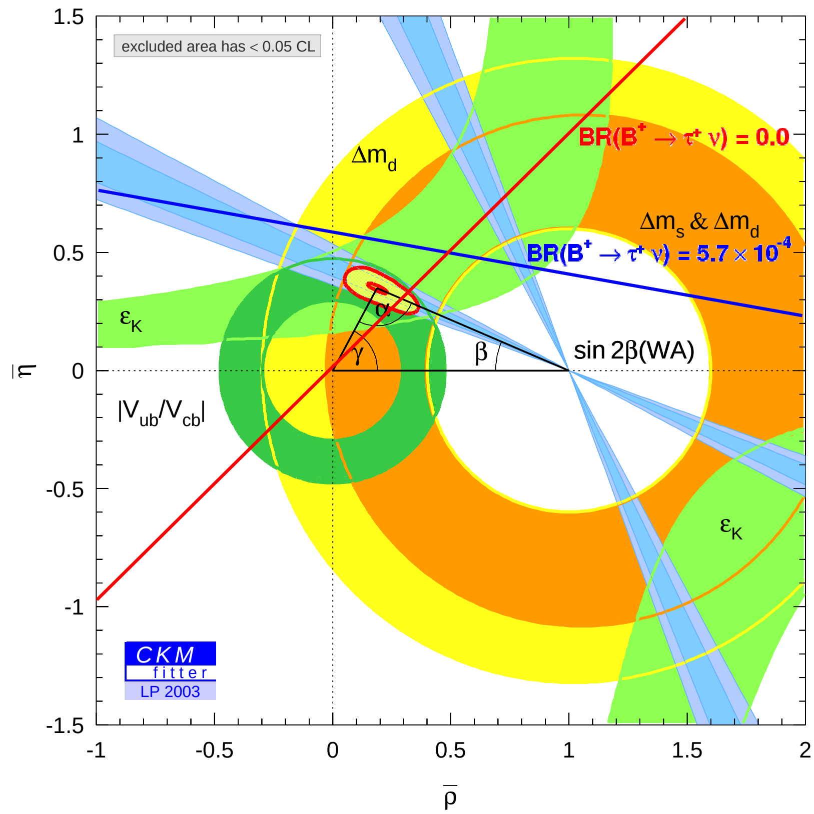

Figure 1.3: The region in the $\bar{\rho}-\bar{\eta}$ plane allowed by combining the L3 limit on the $B^+ \to \tau^+\nu_\tau$ branching fraction with the results from B mixing. The region in the $\bar{\rho}-\bar{\eta}$ plane which is allowed by the L3 limit lies between the red and blue solid lines and includes the region which other measurements have also constrained (the apex of the triangle).

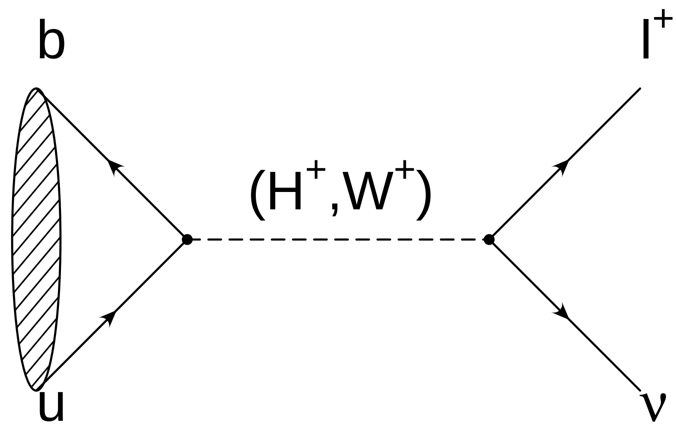

Figure 1.4: The Feynman diagram representing the process $B^+ \to \tau^+\nu_\tau$ mediated by the W^+ or, as allowed by supersymmetry, the charged Higgs (H^+)

possibility for enhancement or suppression of the branching fraction [16]. In the Minimal SuperSymmetric extension of the Standard Model (MSSM), there are two Higgs doublets. One of the doublets, H_u, gives mass to the up-type quarks (up, charm, top) while the second doublet, H_d, gives mass to the down-type quarks (down, strange, bottom) and the massive leptons. The vacuum expectation value (VEV) for each doublet is denoted v_u and v_d. The ratio of the VEVs is used to define a single parameter in the MSSM, denoted $\tan\beta \equiv v_u/v_d$ [17].

The introduction of a diagram involving charged Higgs exchange modifies the branching fraction formula as follows:

$$\mathcal{B}(B^+ \to \tau^+\nu_\tau)_{measured} = \mathcal{B}(B^+ \to \tau^+\nu_\tau)_{SM} \times \left[1 - m_B^2\left(\frac{\tan\beta}{M_{H^+}}\right)^2\right] \tag{1.21}$$

The measured value of the branching fraction can then be used to place restrictions on $\tan\beta/M_{H^+}$.

Chapter 2

The *BABAR* Detector at PEP-II

The facilities which produce and detect the B mesons used in this search for $B^+ \to \tau^+\nu_\tau$ are located at the Stanford Linear Accelerator Center in Menlo Park, California. The B mesons are produced in electron-positron (e^+e^-) collisions in the PEP-II electron-positron storage rings. The decay products of the B mesons are detected by a particle detector called *BABAR* (which stands for "B and B-bar"). This experimental apparatus is described in the following sections. A more complete description of the collider and detector is available in reference [18].

2.1 The Requirements of the SLAC B Factory

The main purpose of the SLAC B-factory is to study the time evolution of the B meson and search for evidence of CP violation. The secondary goals of the B-factory include precision measurements of decays of bottom and charm mesons and of τ leptons, and searches for rare processes that become accessible with the high luminosity of the B-Factory [19]. This goal imposes important physical considerations of the design of the B-factory. Modes which are expected to exhibit CP violation are typically rare (occurring less than 0.01% of the time). To obtain the large data samples needed to precisely study CP violation, the B-Factory must produce a large number of B mesons. To meet this requirement, the facility operates at a very high luminosity (interactions/ cm^2/s) for a typical ten month period.

CP violation measurements also require that the B mesons be resolvable, since accurate measurements of the temporal separation of the meson decays are required. To achieve this, PEP-II accelerates electrons to 9.0 GeV and positrons to 3.1 GeV. In the center-of-mass frame, the energy of their collision is $E_{cm} = 10.58\,\mathrm{GeV}$. This produces the $\Upsilon(4S)$ resonance, which decays exclusively into a pair of B mesons (50% B^+B^- and 50% $B^0\overline{B}^0$). In the detector's reference frame, the pair of B mesons travel in the direction of the electron beam. Because of this asymmetric collision, the decay products of the B mesons also tend to travel in the direction of the electron beam. Consequently, the *BABAR* detector is designed with more instrumentation and angular coverage in the forward direction (that of the electron beam).

Many of the physics goals of the *BABAR* collaboration require full reconstruction of at least one of the B mesons. Consequently, the *BABAR* detector has excellent particle tracking and identification and energy resolution.

2.2 The PEP-II Asymmetric Collider

PEP-II[1] is an asymmetric e^+e^- collider operating at a center-of-mass energy at the $\Upsilon(4S)$ resonance (10.58 GeV). Due to the fact that the $\Upsilon(4S)$ mass is only slightly larger than twice the mass of the B meson, the remaining energy in the $\Upsilon(4S)$ center-of-mass frame is not large enough to induce the B mesons to travel far from their production site. The PEP-II accelerator overcomes this feature by colliding the electrons and positrons at different energies and Lorentz-boosting the $\Upsilon(4S)$ system in the laboratory frame. The electrons are given an energy of 9.0 GeV and the positrons an energy of 3.1 GeV, resulting in a Lorentz boost of $\beta\gamma = 0.56$. This boost provides a mean separation for the B mesons of $\sim 250\,\mu$m.

Important parameters of the PEP-II storage ring system are listed in Table 2.1. The machine was originally designed to achieve an instantaneous luminosity of $3 \times 10^{33}\,\mathrm{cm}^{-2}\mathrm{s}^{-1}$. The machine currently operates above the design luminosity, typically at $5.5 \times 10^{33}\,\mathrm{cm}^{-2}\mathrm{s}^{-1}$. To achieve such high instantaneous luminosities, the machine is operated with a large number of bunches (1034) with relatively small spacing (5.0 ns). Although the number and spacing of bunches is typically below the design level, the luminosity has exceeded design because of improvements in the electron beam current.

PEP-II is shown in Fig. 2.1. Due to the asymmetric beam energies two distinct rings are required, one to store positrons (the Low Energy Ring, or LER)

---

[1] PEP-II stands for "Positron-Electron Project II". The original PEP was built at SLAC in 1980. It was intended as an upgrade to SPEAR for further study of fundamental particles. PEP-II and the asymmetric B-Factory were initiated in 1994.

Table 2.1: The parameters of the PEP-II e^+e^- asymmetric storage rings

Parameters	Design	Typical
Energy (HER/LER) (GeV)	9.0/3.1	9.0/3.1
Current HER/LER (A)	0.75/2.15	1.2/1.5
No. of Bunches	1658	1034
Bunch Spacing (ns)	4.2	5.0
σ_{Lx} (μm)	110	120
σ_{Ly} (μm)	3.3	4.5
σ_{Lz} (mm)	9	9
Luminosity ($10^{44}\,\mathrm{cm}^{-2}\mathrm{s}^{-1}$)	3	5.5
Luminosity (pb^1/day)	135	191

and one to store electrons (the High Energy Ring, or HER). The rings are stacked, with the LER located above the HER. Particles are injected into the PEP-II rings from the SLAC linear accelerator at the desired energies, and no further acceleration is done in the storage rings.

The *BABAR* detector is located at the interaction point of PEP-II. In order to bring the bunches into collision and diverge them again before they reach the first parasitic collision point (located 63 cm away) it is necessary to place magnets close to the interaction point (IP). Figure 2.2 shows a schematic of the interaction region. The vertical scale of the figure is exaggerated to help separate the components of the interaction region. The interaction point, where the electron and positron beams are brought into collision, lies at the center of Fig. 2.2. Permanent dipole magnets (labeled **B1** in Fig. 2.2) are located ± 20 cm away from the IP. These tapered permanent magnets separate the beams after collision. Permanent samarium-cobalt quadrupole magnets (labeled **Q1** in Fig. 2.2) are positioned at

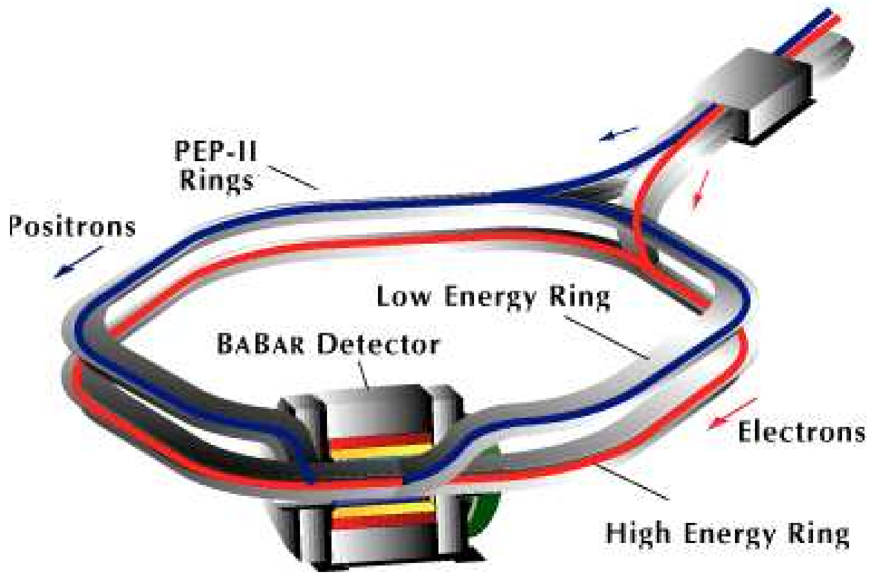

Figure 2.1: The PEP-II e^+e^- asymmetric collider. The facility consists of a pair of stacked rings. The electrons are stored in the lower ring and the positrons are stored in the upper ring.

± 80 cm from the IP inside the *BABAR* solenoid. A standard set of iron quadrupoles (labeled **Q2**, **Q4** and **Q5** in Fig. 2.2) lies on the fringe fields of *BABAR*'s solenoid. Together, these quadrupole magnets provide a final focus for the electron and positron beams before they collide.

Since the B1 and Q1 magnets are within the active region of the detector, their presence has some impact on the geometrical acceptance of *BABAR*. In addition, the interaction region is enclosed by a water-cooled beam pipe of 27.9 mm outer radius, composed of two layers of beryllium (0.83 mm and 0.53 mm thick) with a 1.48 mm water channel between them. To attenuate synchrotron radiation the interior surface of the pipe is coated with a 4 μm thin layer of gold. In addition, the beam pipe is wrapped with 150 μm of tantalum foil on either side of the IP.

The total thickness of the central beam pipe cross-section at normal incidence corresponds to 1.06% of a radiation length.

2.3 An Overview of the *BABAR* Detector

The *BABAR* detector was completed in 1998 and has been collecting data for the past five years. It provides excellent charged particle tracking and identification, as well as excellent energy resolution. A cut-away picture of the detector is shown in Fig. 2.3, with the most salient features indicated by numbers.

1. The Silicon Vertex Detector (SVT) is a five double-sided layer silicon microstrip detector. It provides accurate position information for charged particles, and is the primary tracking system for particles with momenta below 130 MeV. It provides some particle identification information through ionization (energy loss per unit distance, or dE/dx) measurements.

2. The Drift Chamber (DCH) is a wire chamber filled with a helium-isobutane gas mixture. It is the primary tracking system for most charged particles and additionally provides particle identification information through dE/dx measurements.

3. The Detector of Internally Reflected Cherenkov Light (DIRC) is an imaging Cherenkov detector designed to provide charged hadron particle identification.

4. The Electromagnetic Calorimeter (EMC) is a cesium-iodide crystal calorime-

ter. It is designed to detect neutral electromagnetic particles and to provide particle identification information through the use of energy deposition and electromagnetic shower topology.

5. A super-conducting solenoid produces a $1.5\,T$ field which bends charged particles and allows for their momentum and charge to be determined.

6. An Instrumented Flux Return (IFR) serves both as a return yoke for the magentic field and as an identification system for muons and long-lived neutral hadrons. The iron in the return yoke is interspersed with active detector components.

In addition to these hardware components a significant amount of resources are required for the acquisition, processing, storage, and analysis of the data.

The coordinate system for the experiment is also shown in Fig. 2.3. The z direction is defined to be the direction of the electron beam. The *forward* region of the detector is that half which lies in the $+z$ direction from the IP. The y axis points toward the top of the detector, and the x axis is defined perpendicular to y and z as in a right-handed coordinate system (into the page, in Fig. 2.3).

There are several important angles which are also defined relative to the x, y and z directions. The *polar angle*, denoted θ, is defined as the angle off the $+z$ direction, and ranges between 0 and π. The *azimuthal angle*, denoted ϕ, is defined in the $x-y$ plane as the angle about the z axis. The azimuthal angle ranges between 0 and 2π.

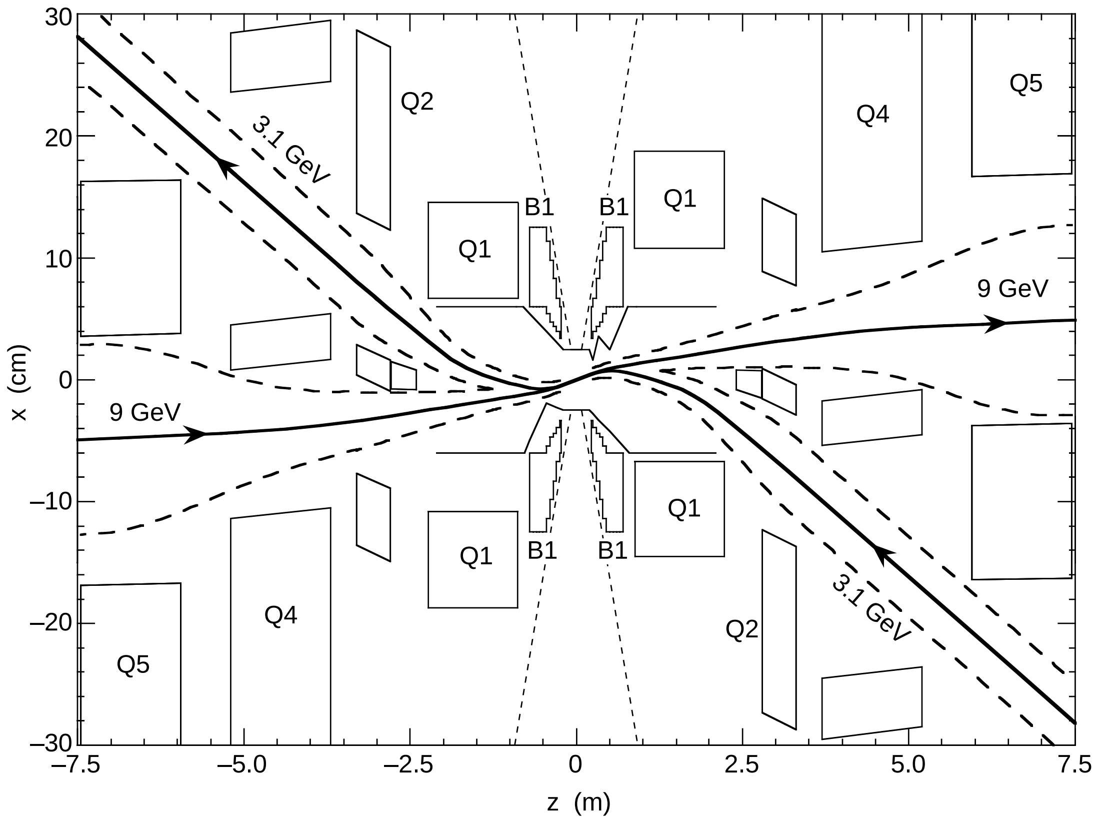

Figure 2.2: A plan view of the interaction region. The vertical scale is exaggerated. The interaction point (IP) where the electron and positron beams collide is located at the center of the plot. The boxes labeled **B**n indicate a dipole magnet, while the boxes labeled **Q**n indicate a quadrupole magnet. The thick dashed lines which follow the electron and positron beams (black arrows) indicate the stay-clear envelopes of the beams. The vertical dashed lines near the center of the plot indicate the *BABAR* detector acceptance cutoff at 300 mrad.

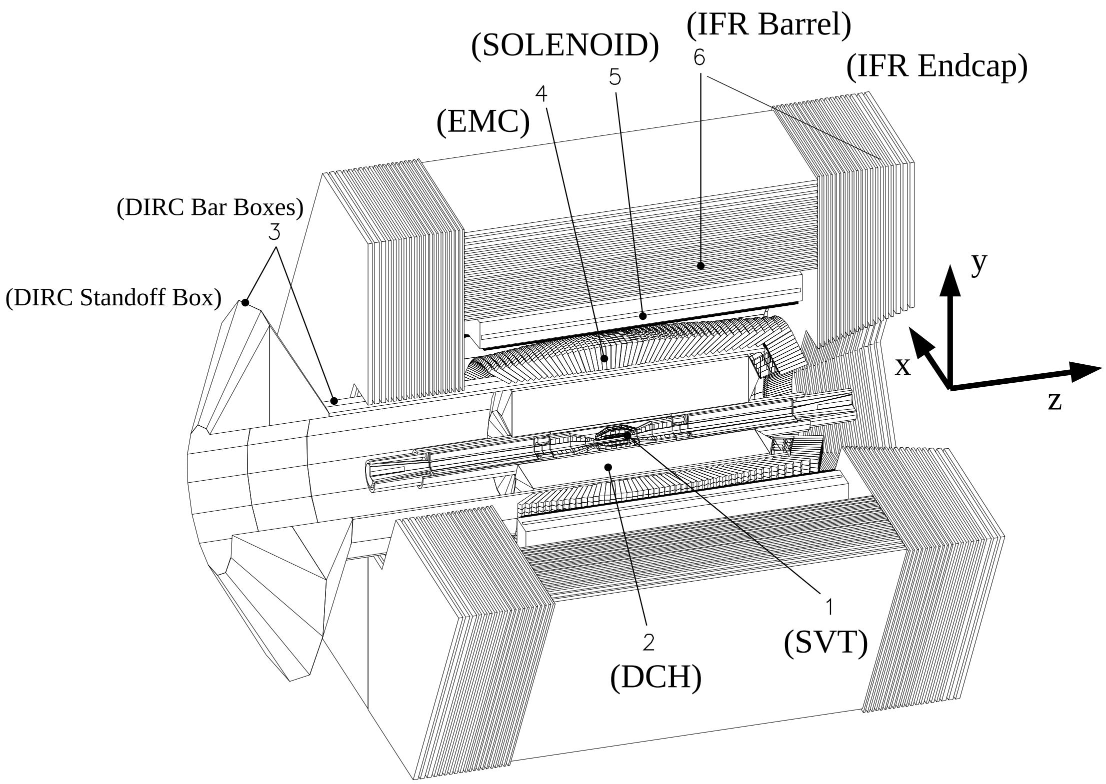

Figure 2.3: Layout of the *BABAR* detector. The detector is comprised of multiple subdetectors, each serving a different purpose (charged particle detection, energy reconstruction, etc.). The coordinate system is also indicated. The z-direction points in the direction of the electron beam and defines the *forward* direction of the detector. The x-axis points into the page and the y-axis up toward the top of the detector.

2.4 The Silicon Vertex Tracker

The innermost subsystem of the *BABAR* detector is the Silicon Vertex Tracker (SVT). It provides precise tracking information for charged particles from B meson decay. This allows for the reconstruction of the mesons and the determination of their decay vertex. The active elements of the detector are silicon microstrip detectors, and their layout is detailed in section 2.4.1. Because the SVT is the closest detector to the PEP-II collider it receives the most radiation. For this reason it is designed to withstand an integrated radiation dose of about 2 MRad over a period of 4-5 years.

In order to measure the displacement between the B mesons, the silicon microstrip detectors that comprise the SVT were designed with point resolutions of $10 - 40\,\mu$m. Since the B mesons are Lorentz boosted by a factor $\beta\gamma = 0.56$ and have a lifetime of 1.5 ps, their typical separation is $(\beta\gamma)c\tau = 258\,\mu$m. The design of the SVT allows provides good resolution for the decay vertices of the B mesons.

2.4.1 SVT Detector Layout

Transverse and longitudinal views of the SVT are shown in Fig. 2.4 and 2.5, respectively. The SVT consists of five concentric cylindrical layers of double-sided silicon detectors, as shown in Fig. 2.4. Each layer consists of several modules evenly spaced about the azimuth. The inner layers (1-3) are flat while the outer layers (4-5) are arch-shaped to increase coverage of the solid angle. This feature of the SVT design is clear from Fig. 2.5. In addition, the SVT is designed asymmetrically along the z axis, with longer arches in the $+z$ direction to cover more of the forward solid angle.

The inside of each silicon detector has strips running perpendicular to the beam direction to measure the z coordinate, while the outer sides have strips orthogonal to the inner strips to measure the ϕ coordinate. The silicon sensors are built in six sizes (see Fig. 2.5 for their positions, numbered with Roman numerals) and distributed according the the mechanical requirements of each section of the detector. In total, there are 340 detectors requiring 150,000 readout channels. The active silicon area covers $0.96\,\mathrm{m}^2$. The material traversed by particles is 4% of a radiation length. The geometrical acceptance of the SVT is 90% of the solid angle.

The SVT modules function by measuring current induced during the passage of ionizing charged particles through the silicon substrate. Each of the silicon microstrip sensors is $300\,\mu$m thick. A minimum-ionizing particle traversing the sensor deposits a charge of $3.5\,fC$.

The induced signals from the strips are amplified and shaped, then compared with a threshold. The time spent over the threshold (*Time-Over-Threshold*, or TOT) is approximately logarithmically related to the charge induced on the strip. Instead of reading out each and every channel, the threshold state of the channel is polled every 66 ns and buffered in anticipation of a transfer request from the Level

1 trigger. Prior to the trigger request, channel, timestamp and TOT information are digitized and transferred to off-detector electronics for use in the event-building process.

2.4.2 SVT Detector Performance

The SVT performance has been excellent throughout data-taking operations. The only significant performance problems correspond to broken electrical connections or static electricity damage to data-readout sections during installation. In all, 10 (out of 204) readout sections have failed during the period 1998-2002.

As can be seen from Fig. 2.6, the SVT has uniform performance in all layers and throughout the azimuthal angle (half-module number corresponds to the ϕ angle). The measured efficiency of 97% allows for standalone track reconstruction in the SVT. Figure 2.6 also shows the single hit resolution for z and ϕ hits, respectively. The SVT resolution varies as a function of a charged particle's incident angle to a layer. For an incident angle of 90°, the resolution is $10\,\mu$m, and ranges up to $40\,\mu$m for an incident angle of 50° (Fig. 2.6).

An important consideration for the SVT is the dosage of radiation that it receives from the PEP-II collider. The silicon mirostrip detectors were designed to be more resistant to radiation damage ("radiation hardened"). The SVT modules have been shown to function even after they undergo type inversion after receiving a dose between 1-3 MRad. Currently, the SVT is within its allotted radiation dose budget. A replacement of the SVT is planned for 2005.

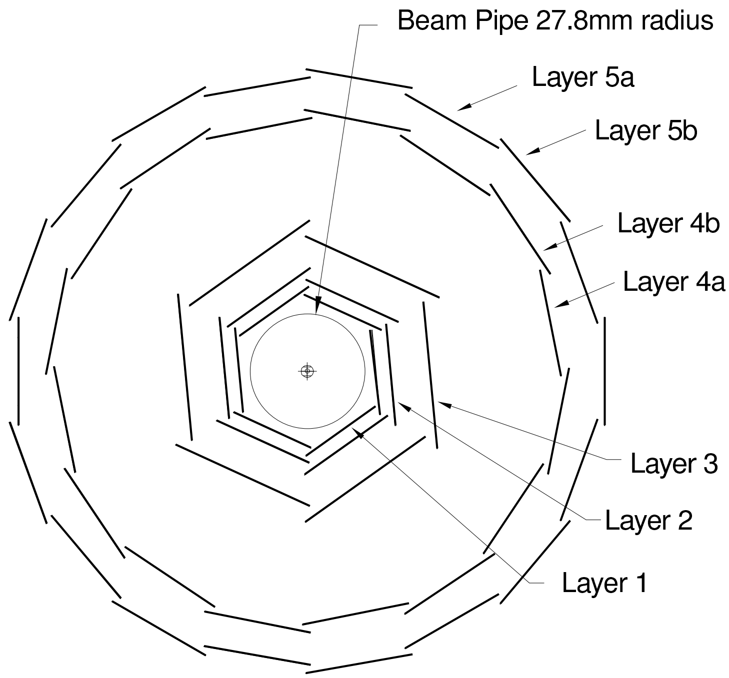

Figure 2.4: A schematic view of SVT showing the tranverse cross-section of the detector. The SVT is divided into five layers surrounding the interaction point. The sections in each layer overlaps slightly to prevent gaps in the azimuthal coverage of the SVT.

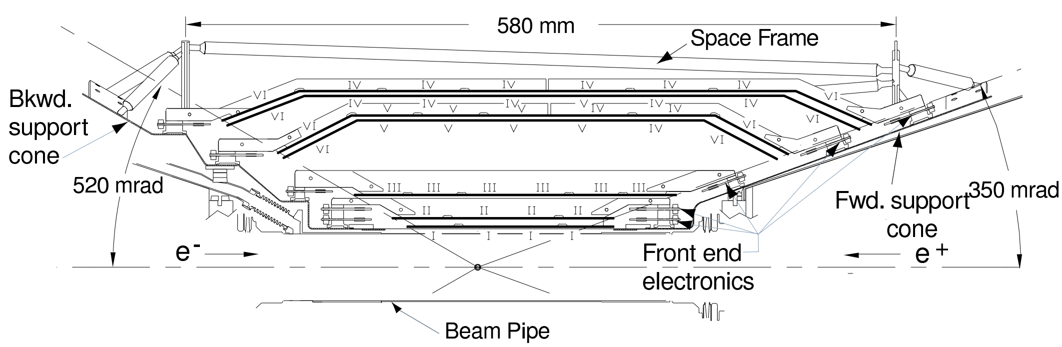

Figure 2.5: Schematic view of SVT: longitudinal section. The roman numerals label the six different geometrical designs of silicon sensor used in the SVT. The asymmetric design of the SVT is clear, with more angular coverage in the forward direction.

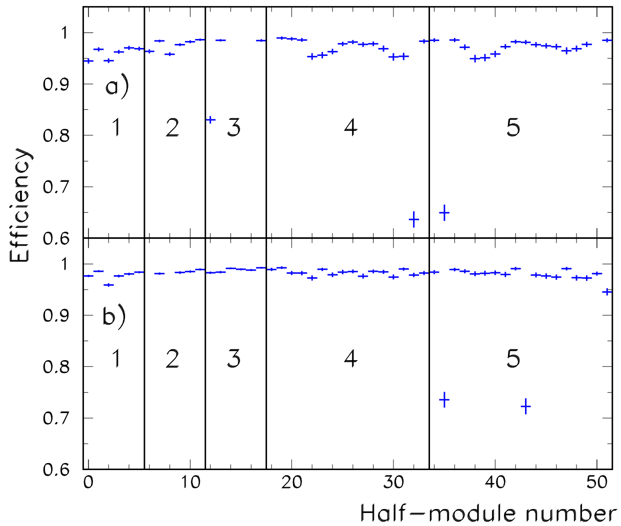

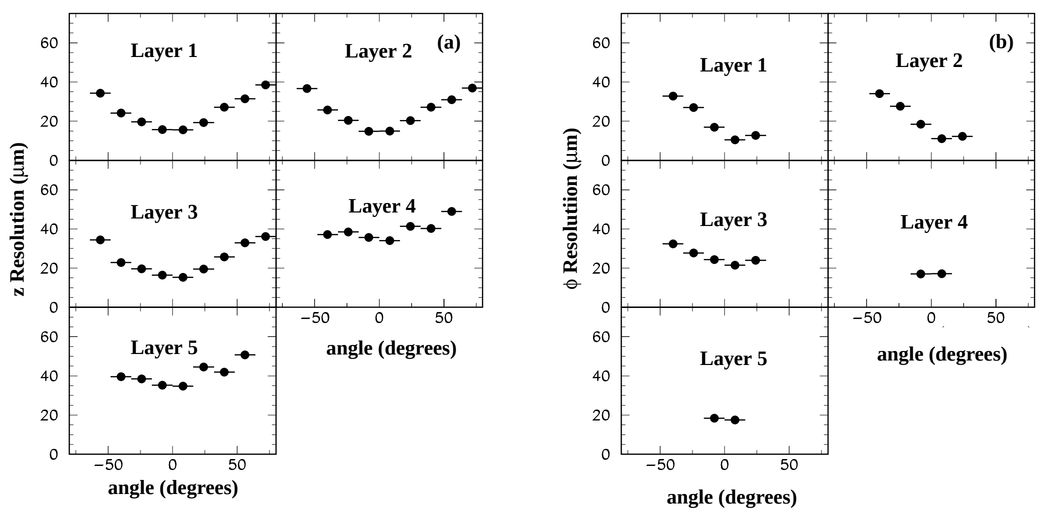

Figure 2.6: SVT performance plots. The top plot shows the single hit effiency across the SVT, while the bottom plots show the z (left) and ϕ (right) single hit resolutions by layer and incident angle. All three plots are from a typical run (14558). The efficiency of the SVT is flat across all layers and throughout the azimuthal angle. The average efficiency of the SVT is 97%, including both hardware and software performance.

2.5 The Drift Chamber

The *BABAR* drift chamber (DCH) is the primary tracking detector. A typical $B\overline{B}$ event can have as many as 12 charged particles, and in some cases many more. The DCH is capable of resolving the individual charged particles in high multiplicity events, even in the presence of PEP-II beam-related backgrounds. The DCH detects charged particles by collecting electrons produced as they ionize gas molecules in the tracking volume [20].

Challenges posed by the physics of $B\overline{B}$ events shaped the design of the DCH. There are often long-lived particles, such as K_S^0, which decay outside the SVT detector volume. For these particles the DCH is solely relied upon for vertex resolution. In addition, the DCH provides good particle identification information (via energy loss, denoted dE/dx) for low-momentum charged particles. Since multiple scattering effects were expected to dominate the tracking resolution, the active components of the DCH amount to 0.2% of a radiation length.

The layout and readout of the detector are described in Sec. 2.5.1 and the performance of the DCH is described in Sec. 2.5.2.

2.5.1 DCH Detector Layout

A schematic side-view of the *BABAR* DCH is shown in Fig. 2.7. The *BABAR* drift chamber is a 280 cm-long cylinder of inner radius 23.6 cm and outer radius 80.9 cm. Since *BABAR* events are Lorentz boosted in the forward direction, the center of the drift chamber is located ahead of the IP by 3.7 cm. The wires that form the active components of the DCH are grouped into 40 layers. Each layer

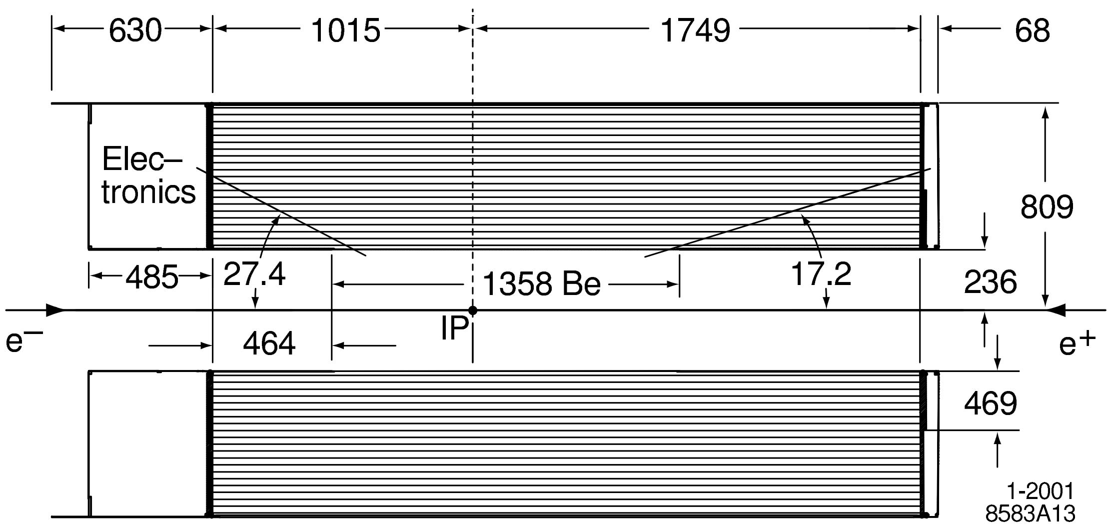

Figure 2.7: A longitudinal view of the DCH with principle dimensions; the chamber center is offset by 370 mm from the interaction point.

consists of small hexagonal cells (7,104 total cells). For particles with tranvserse momentum greater than 180 MeV/c this provides up to 40 spatial and ionization loss measurements[2]. The 40 layers are then additionally grouped into 10 *superlayers.* The chamber is filled with an 80 : 20 helium:isobutane mixture. This gas mixture provides a very stable ion drift velocity of 22 μm/ ns.

The drift chamber provides both azimuthal and longitudinal information about the position of a charged particle as it ionizes the gas. Longitudinal information is obtained by placing the wires in 24 of the 40 layers at small angles with respect to the z-axis. The offset angle increases from the inner radius of the DCH, where it is $45-57$ mrad, to the outer radius, where it is $65-76$ mrad. The 28,768 wires are attached to the endplates of the DCH through $2.5-4.5$ mm holes whose

[2]A particle which has $p > 180$ MeV/c will traverse at least half layers in the $x-y$ (transverse) plane. This is required to obtain an efficient reconstruction of the track in the DCH.

position are drilled to a 38 μm accuracy.

The drift cells, illustrated in Fig. 2.8, are hexagonal in shape, 11.9 mm by approximately 19.0 mm along the radial and azimuthal directions, respectively. Each cell consists of one sense wire surrounded by six field wires. The sense wires are made of tungsten-rhenium, while all other wires are made from aluminum; all are plated with gold. While the field wires are grounded, a positive high voltage (1930 V) is applied to the sense wires. The sense wires collect the electrons from the ionized gas molecules, while field wires shape the electric field around the sense wires. *Guard wires* help to match the gain of wires near a cell boundary to that of the inner wires. *Clearing wires* collect charge produced by photon conversions in the material of the chamber walls.

The drift chamber is housed by a robust mechanical assembly designed to minimize the amount of material while providing adequate strength to support the chamber. The inner cylindrical wall of the DCH is 5 mm-thick aluminum, except near the IP where the DCH wall is made from 1 mm-thick beryllium. The outer wall is made from two 1.6 mm-thick carbon-fiber skins covering a 6 mm-thick composite honeycomb core. The inner and outer cylindrical walls of the drift chamber are load-bearing to reduce the maximum stress carried by the endplates of the drift chamber. The inner and outer walls a carry 40% and 60% of the axial wire load, respectively. The endplates, made from 24 mm-thick aluminum, carry an axial load of $31,800$ kN. The total thickness of the DCH at normal incidence is 1.08% of a radiation length, of which the wires and gas mixture contribute 0.2%

and the inner wall 0.28%.

The DCH is read out by electronics which look for the leading edge of the signal from charge arriving on the sense wire. The time is then digitized with a resolution of 1 ns. For the purpose of dE/dx measurements, the total charge in the pulse is integrated. To reduce the amount of material in the path of charged particles, the readout electronics are mounted on the rear endplate of the DCH. The electronics provide the information from all 7104 channels to the trigger system. The readout electronics system is designed to deliver reliable performance even under high background conditions, with a single-cell efficiency for the trigger signal of greater than 95%.

2.5.2 DCH Detector Performance

The DCH has performed quite well from the beginning of data taking through the present. Only one significant period of performance problems occurred when the voltage across the chamber was lowered from 1960 V to 1900 V. This was done to address concerns about the longevity of the chambers, and the voltage change caused a 10% drop in efficiency in the central region of the detector. The voltage in the chamber was later raised to 1930V as a median between performance and longevity.

The typical spatial resolution of a cell and the overall dE/dx resolution are shown in Fig. 2.9. The top plot in Fig. 2.9 shows that the resolution of detecting ionization from tracks on either side of the sense wire (averaged over all cells in the layer) is typically 0.1 mm (The sense wire spacing between adjacent cells is

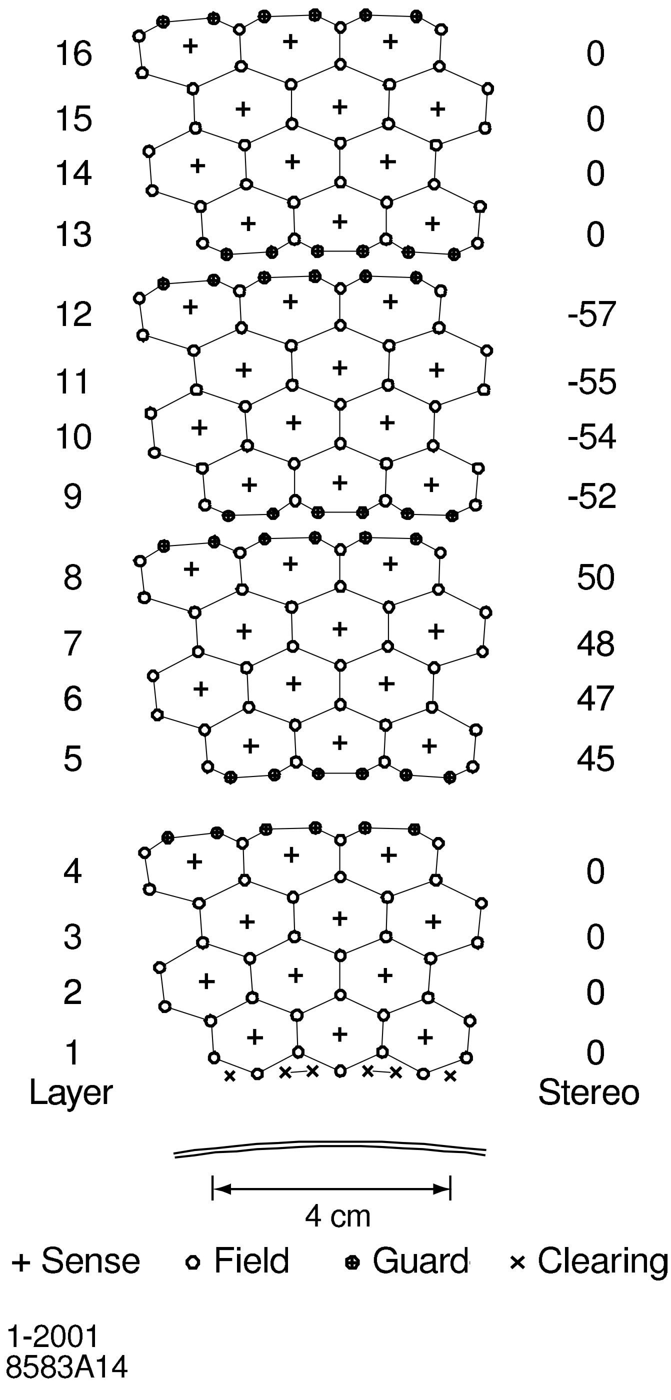

Figure 2.8: Schematic layout of drift cells for the four innermost superlayers. Lines have been added between field wires to aid in visualization of the cell boundaries. The numbers on the right side give the stereo angles (mrad) of sense wires in each layer. The 1 mm-thick beryllium inner wall is shown inside the first layer.

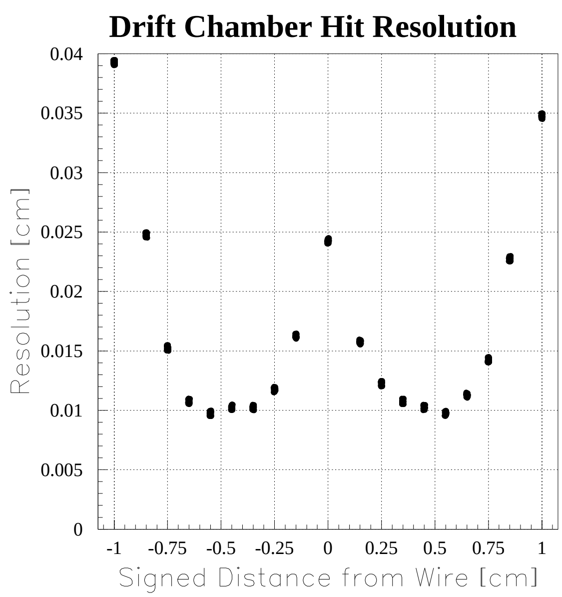

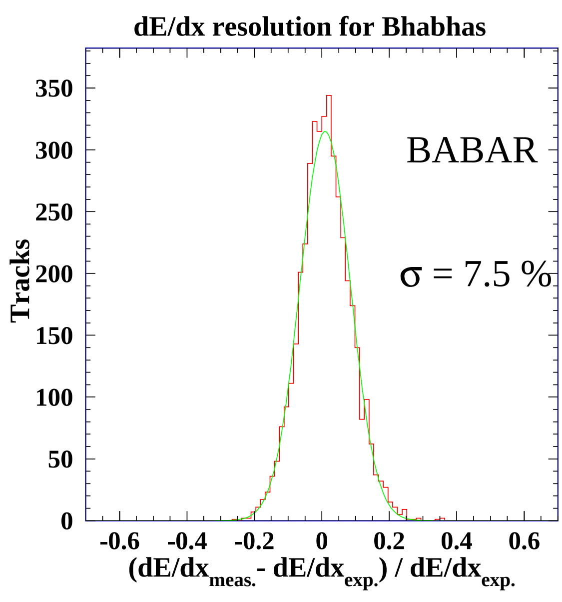

Figure 2.9: Drift chamber performance plots. The top distribution shows the DCH position resolution as a function of the drift distance in layer 18, for tracks on the left and right sides of the sense wire. The DCH dE/dx resolution (overall) is shown in the bottom plot.

about 1.5 cm, shown in Fig. 2.8). The bottom plot in Fig. 2.9 shows the dE/dx resolution determined using Bhabha events (7.5%).

2.6 The Detector of Internally Reflected Cherenkov Light

The Detector of Internally Reflected Cherenkov light (DIRC) is a novel particle identification device. The particle identification requirements of *BABAR* are based on the need to identify the flavor of the non-CP eigenstate B meson and to distinguish between different decay modes. The need to separate final states is of particular importance to analyses that use B decays such as $B^+ \to \pi^+\pi^-$, where contamination by kaons is a serious concern. Such distinction requires good kaon and pion separation up to $4\,\mathrm{GeV}/c$.

Particle identification is achieved in the DIRC by taking advantage of the fact that particles exceeding the speed of light in a medium will emit Cherenkov radiation at a characteristic angle. The DIRC operates by trapping Cherenkov photons using total internal reflection in the radiator material. This principle is illustrated in Fig. 2.10. The angle that the radiation makes with respect to the momentum of the particle is well-defined, $\theta_c = \cos^{-1}(1/\beta n)$, where n is the index of refraction of the radiator medium.

The layout and performance of the DIRC are described in Sec. 2.6.1 and 2.6.3, respectively.

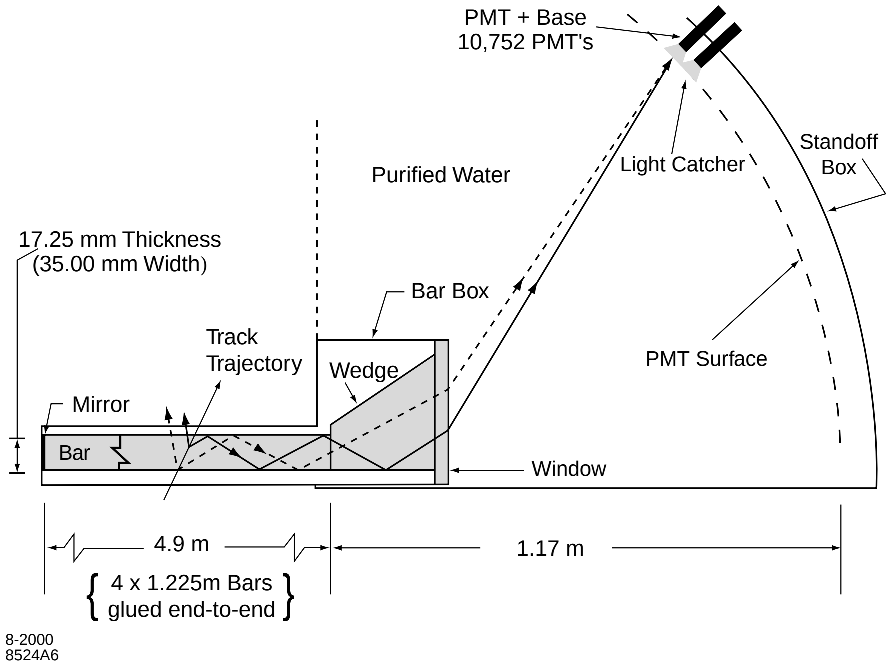

Figure 2.10: Schematic of a single DIRC radiator bar. The particle trajectory is represented as an arrow passing through the bar. The radiated Cherenkov photons are represented by lines reflecting inside the quartz bar.

2.6.1 DIRC Layout

The layout of the DIRC is illustrated in Fig. 2.11. The DIRC radiator consists of 144 synthetic quartz bars polygonally arranged in 12 boxes around the barrel of the detector. Each bar has a rectangular cross section with dimensions 1.7 cm × 3.5 cm × 4.9 m. The bars are made from synthetic quartz silica (Spectrosil[3], $n_{quartz} = 1.474$). This material was chosen because of its resistance to ionizing radiation, long attenuation length, large index of refraction, low chromatic dispersion within the wavelength acceptance of the DIRC, and because it

[3]Sprectrosil is the trademark of TSL Group PCL, Wallsend, Tyne on Wear, NE28 6DG, England; Sold in the USA by Quartz Products Co., Louisville, KY, USA.

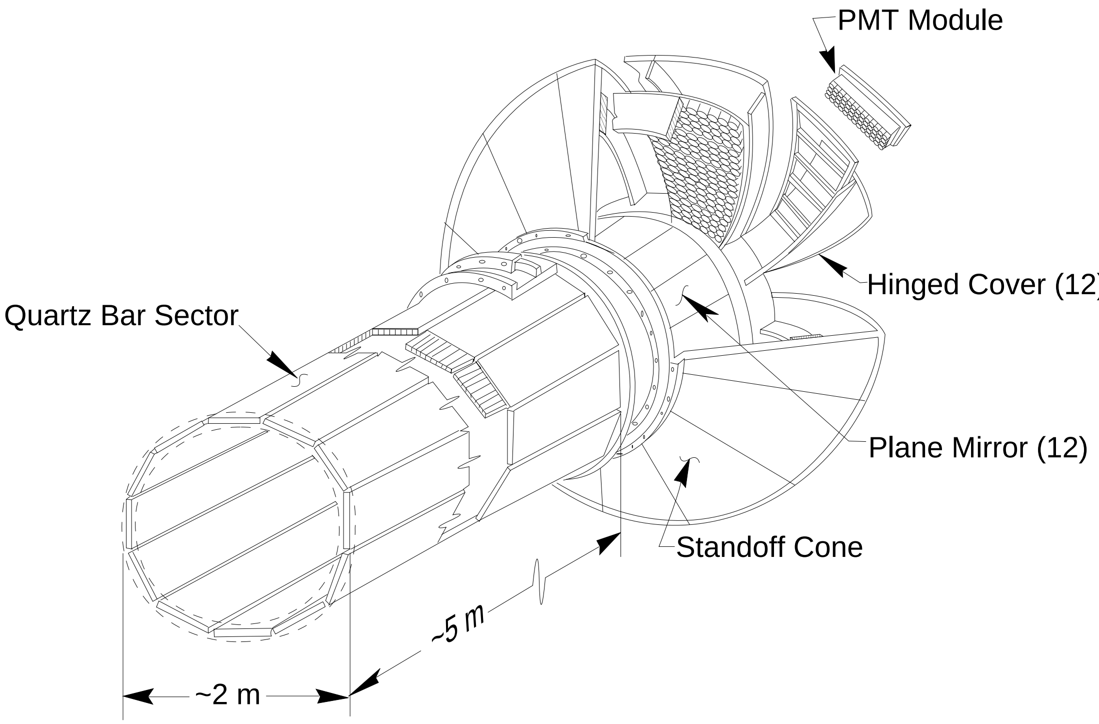

Figure 2.11: Schematic of the DIRC showing the mechanical elements. Included are the mirrors mounted inside the standoff cone, used to reflect Cherenkov light toward the photomultiplier tubes.

allows an excellent optical finish on the bar surface.

The bars extend through the magentic flux return in the backward direction in order to deliver the light outside the tracking and magnetic field volumes. Since particles tend to travel in the forward direction (due to the Lorentz boost), the readout electronics are located at the back of the detector. The DIRC radiator array covers 87% of the polar angle and 93% of the azimuthal angle. The bars have mirrors perpendicular to the bar axis at the forward end to reflect light toward the detector electronics at the back end. The back end of each bar is glued to a fused silica wedge, which helps direct the Cherenkov radiation toward the active detector components.

At the back of the DIRC, the detector components are housed in a *standoff cone*. The standoff cone consists of mirrors to reflect the Cherenkov light toward an array of 10,752 photomultiplier tubes (PMTs). After exiting the quartz bars, the light is allowed to expand in a tank containing 6000 liters of ultrapure, deionized water. The water is chosen because its index of refraction ($n \approx 1.346$) is a close match to the quartz, reducing internal reflection at the quartz-water interface.

The Cherenkov ring is imaged by the PMTs, each with a diameter of 2.82 cm. The PMTs are arranged on a toroidal surface so as to present a uniform 1.2 m pathlength over most of the angular range. Each PMT is held at a voltage of 1.1 kV. The detector electronics readout the PMTs in groups of 64 each by a single electronics board. The boards amplify and shape the pulses, as well as buffer the information in anticipation of a request from the Level 1 trigger system.

2.6.2 DIRC Reconstruction

The reconstruction of the Cherenkov angle is done in several steps. First, charged tracks are projected to their impact point in the DIRC. The expected pattern of hits in the DIRC is calculated for each of the five charged track hypotheses (π^-,e^-, K^-, p^+ and μ^-). Timing information is crucial for resolving the multi-fold ambiguity caused by the many possible reflections along the path of the Cherenkov light.

The best particle hypothesis is determined by performing a χ^2 fit using the expected and observed numbers of photons. The hypothesis with the best χ^2 is chosen; this has the effect of artificially forcing the fitting angle θ_c toward an expected value, though not always the correct one.

2.6.3 DIRC Performance

Although there was a delay in the completion of the DIRC very early on in *BABAR* (owing to delays in polishing the quartz to the required smoothness), it has performed very well since the beginning of data-taking. Figure 2.12 shows the angular and temporal resolutions of the DIRC. Gaussian fits of the two distributions yield resolutions of 10.2 mrad and 1.7 ns, respectively. The angular resolution for single photons is in agreement with the design expectations, and the timing resolution is extremely close to the intrinsic 1.5 ns transit time spread for the PMTs. The DIRC provides $> 90\%$ kaon identification efficiency for kaons with momenta up to $4\,\mathrm{GeV}/c^2$, with an average pion misidentification rate $< 5\%$ for the same range.

2.7 The Electromagnetic Calorimeter

The Electromagnetic Calorimeter (EMC) is a cesium-iodide crystal calorimeter and functions by measuring the light output from energy deposited by incident particles. The geometric layout of the EMC is presented in Sec. 2.7.1 and its performance is discussed in Sec. 2.7.3.

Many of the B meson decays studied at *BABAR* have at least one π^0 in their final state. The π^0 and B meson reconstruction efficiencies fall off quickly as

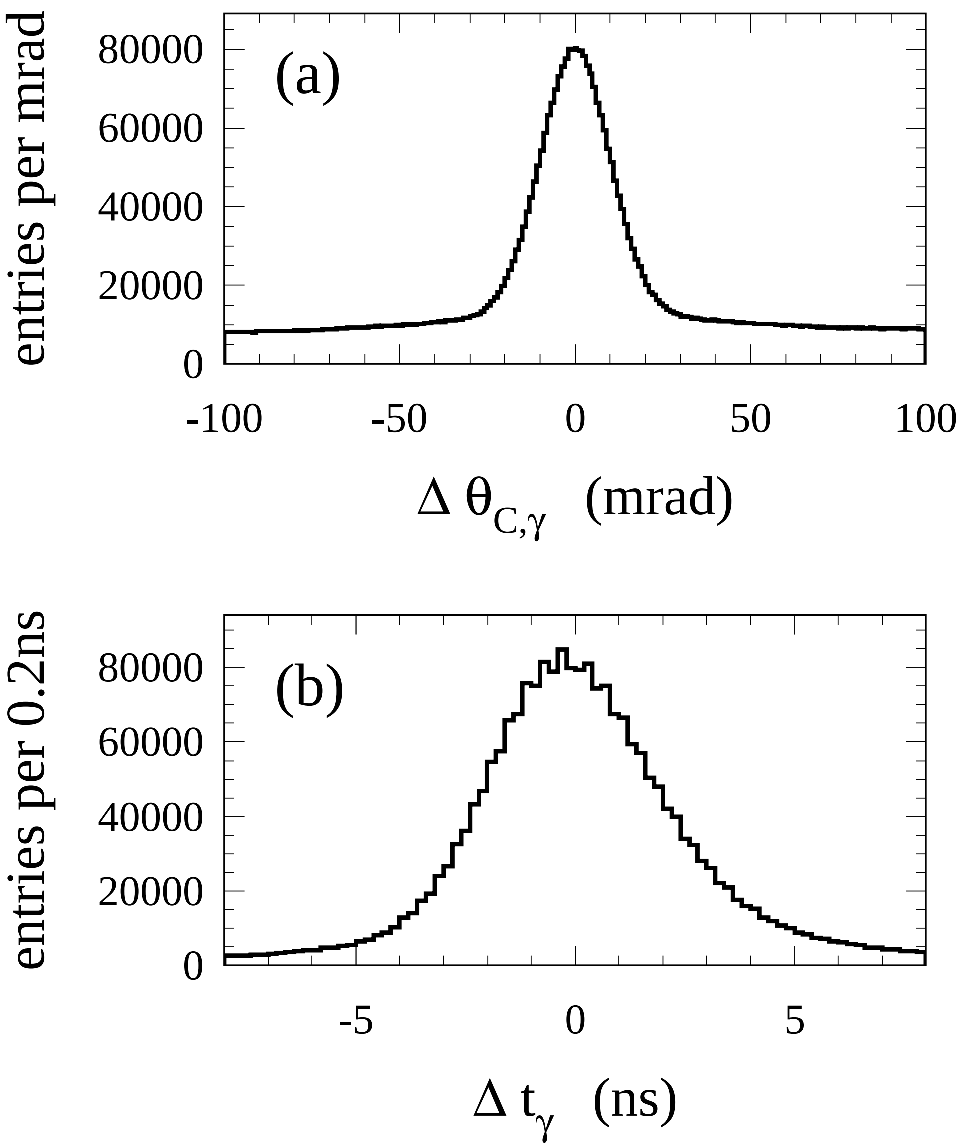

Figure 2.12: The difference between the measured and expected Cherenkov angle ($\Delta\theta_{c,\gamma}$, top) and the measured and expected photon arrival time (Δt_γ, bottom) for single photons. These have been determined from calibration events.

the minimum detectable energy increases. The EMC is highly efficient down to energies of $\sim 20\,\mathrm{MeV}$ and covers a large amount of the solid angle. In addition, to achieve high-purity B meson the energy reconstruction has a low uncertainty ($\sigma_E/E \simeq 3\%$) and an angular resolution of $\sigma_\phi \simeq \sigma_\theta = 3.9\,\mathrm{mrad}$.

In addition to neutral object identification, the EMC provides electron and muon identification using their unique cluster topologies. The EMC is also the other principle input (in addition to the DCH) to the trigger system.

2.7.1 EMC Detector Layout

The geometric layout of the EMC is illustrated in Fig. 2.13. It consists of a quasi-projective arrangement of thallium-doped cesium-iodide crystals. The cylindrical barrel and conical endcap together cover a center-of-mass solid angle of $-0.916 < \cos\theta < 0.895$.

The crystals are divided into two main regions:

- The *barrel region* covers the center-of-mass solid angle between $-.916 \leq \cos\theta \leq 0.715$. The barrel has an inner radius of 91 cm, and contains 5760 crystals arranged in 48 θ rows. Each row has 120 identical crystals position in the ϕ direction. The crystals are then additionally grouped into 280 modules of 7×3 in θ and ϕ, respectively. The crystals vary in length from 29.76 cm (16 radiation lengths) at the rear of the barrel to 32.55 cm (17.6 radiation lengths) at the front.

- The *endcap region* is a conic section with the front and back surfaces at an

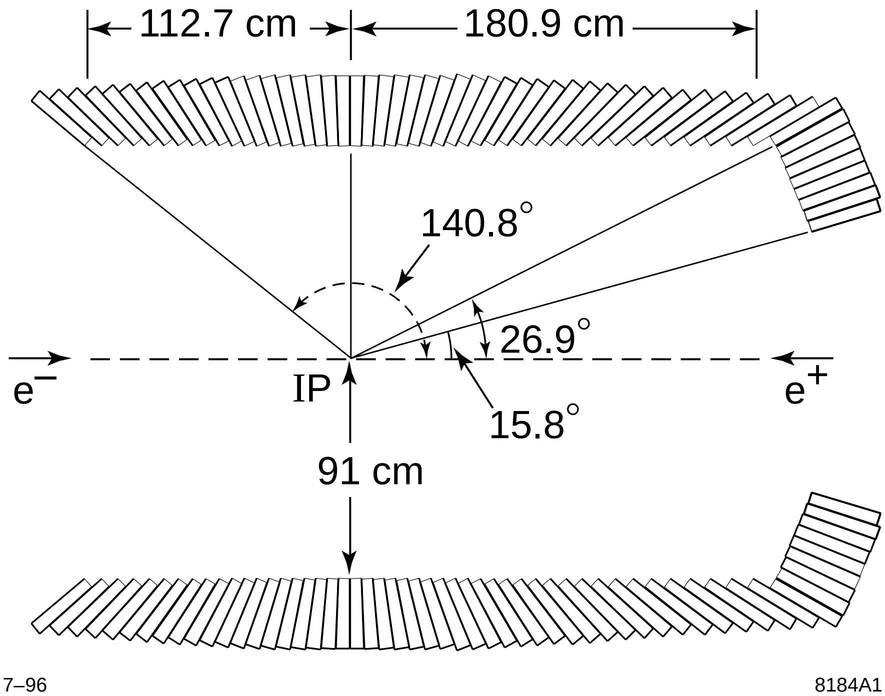

Figure 2.13: Layout of the EMC showing the barrel and forward endcap.

angle of 22.7° to the vertical and covers the center-of-mass solid angle region between $0.718 \leq \cos\theta \leq 0.895$. There are 820 endcap crystals arranged in 8 rings in θ and in modules so as to give a 20-fold symmetry in ϕ. The ϕ segmentation of the first three rings matches that of the barrel with 120 crystals each. The next three have 100 and the final two 80 crystals each. All the endcap crystals are 32.55 cm (17.6 radiation lengths) long except for those in the inner two rings; these are shorter by one radiation length due to space limitations.

All the crystals are trapezoidal in shape with typical dimensions of $47 \times 47\,\mathrm{mm}^2$ at the front face and $60 \times 60\,\mathrm{mm}^2$ at the back end. In order to minimize the loss of particles to inactive material between the crystals they are arranged in a slightly non-projective manner in θ. This non-projectivity ranges between ± 15 mrad and 45 mrad across the detector. The light yield in each crystal is uniform within 2% in the front half of the crystal and to within 5% at the rear face. The back of each crystal is instrumented with a pair of photodiodes and a preamplifier.

The entire calorimeter is surrounded by a Faraday shield composed of two 1 mm-thick aluminum sheets. This shield protects the diodes and preamplifiers that readout the crystals from external noise. The shield also serves as an environmental barrier, allowing the slightly hygroscopic crystals to reside in a dry, temperature controlled nitrogen atmosphere. The crystals are maintained at a constant, accurately controlled temperature. This cooling addresses two concerns: the stability of the photodiode leakage current, which is slightly temperature dependent, and the large number of diode-crystal epoxy joints that could experience stress due to differential thermal expansion.

2.7.2 EMC Readout and Reconstruction

The readout of the crystals begins by detecting the scintillation light produced by a particle incident on the EMC. For purposes of redundancy, this readout is performed using two $1\,\mathrm{cm} \times 2\,\mathrm{cm}$ photodiodes epoxied to the back of each crystal. The signals from the diodes are preamplified by electronics which are also affixed to the back of each crystal. The signals are then delivered to analog-to-digital converter boards (ADC), mounted in mini-crates at the front and back of the calorimeter. The digitized signal is then delivered to the data acquisition board in the *BABAR* electronics house, where the information is stored for use by the Level 1 trigger system.

The average light yield per crystal is 7300 pe/ MeV and varies between 5000 and 10000. The incoherent electronic noise has been measured to be ~ 900 pe or 150 keV per crystal. Such noise levels make a negligible contribution to the overall energy resolution.

Event reconstruction begins with a process called *feature extraction*, where the waveform of each crystal is read and used to integrate the total flow and detect the leading edge of the pulse. Offline calibration information and electronics are used to convert the charge information into the amount of deposited energy.

The next step involves clustering algorithms that group adjacent crystals with energies above a threshold of a few MeV into clusters. *Bump-finding algorithms* are then applied to each cluster to locate local maxima and resolve clusters formed by more than a single particle. The centroid and several moments are then calculated for each cluster, and a final energy rescaling is applied to high-energy clusters (due to leakage of energy through the back of the EMC for high-energy particles).

Tracks are then matched to clusters in the EMC using the χ^2 of the expected track impact point with respect to the cluster centroid. All unassociated clusters are then treated as neutral candidate particles.

2.7.3 EMC Performance

The energy resolution of a homogeneous crystal calorimeter can be described empirically as two terms added in quadrature,

$$\frac{\sigma_E}{E} = \frac{a}{\sqrt[4]{E(\,\mathrm{GeV})}} \oplus b, \tag{2.1}$$

where E and σ_E refer to the energy of a photon and its RMS error, measured in GeV. The energy-dependent term a arises primarily from the fluctuation in photon statistics but also includes electronic noise effects. The term b dominates at high energies ($> 1\,\mathrm{GeV}$) and arises from non-uniform light collection, leakage or absorption in the material between and in front of crystals, and uncertainties in the detector calibration.

A series of control samples are used to measure the response of the calorimeter over a range of energies (Fig. 2.14). Equation 2.1 is fit to the data to obtain the performance of the calorimeter as a function of energy,

$$\frac{\sigma_E}{E} = \frac{(2.32 \pm 0.30)\%}{\sqrt[4]{E(\,\mathrm{GeV})}} \oplus (1.85 \pm 0.12)\%). \tag{2.2}$$

A similar empirical formula is used to determine the angular resolution (Fig. 2.14). The resulting fit to data from the control samples yields

$$\begin{aligned} \sigma_\theta &= \sigma_\phi & (2.3)\\ &= \frac{(3.87 \pm 0.07)}{\sqrt{E(\,\mathrm{GeV})}} \oplus (0.00 \pm .04)\,\mathrm{mrad}. & (2.4) \end{aligned}$$

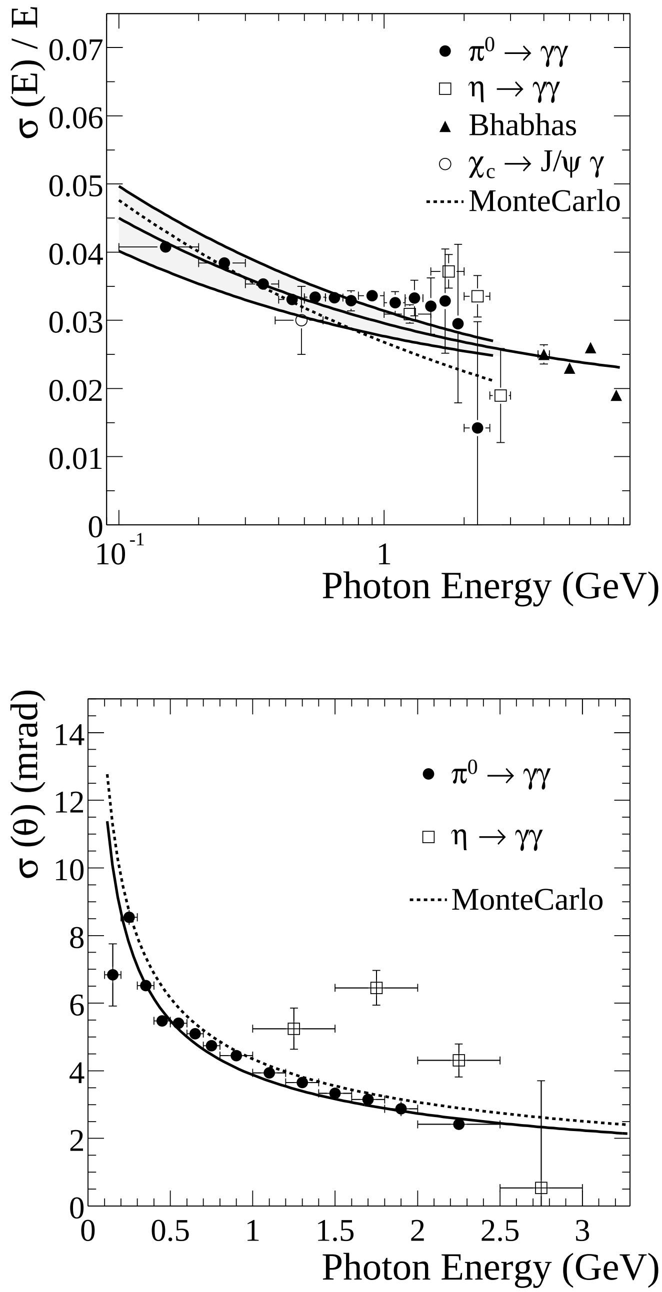

Figure 2.14: EMC performance plots. The EMC energy resolution is shown on the top, and the angular resolution on the bottom. Values are given from several calibration methods for comparison. The solid lines represent the fits (and fit uncertainty) of Eqn. 2.1 to the data.

Table 2.2: *BABAR* magnet parameters

Parameter	Value
Central Field	1.5 T
Maximum Radial Field	< 0.25 T
Mean Solenoid Diameter	3060 mm
Solenoid Length	3513 mm
Stored Energy	27 MJ

2.8 The Superconducting Solenoid

The *BABAR* solenoid provides a 1.5 T field to allow measurement of the transverse momentum of charged particles. The solenoid is manufactured from superconducting niobium-titanium (46.5% by weight Nb) filments. The filaments are wound into 0.8 mm strands, 16 of which are then formed into *Rutherford cable* measuring 1.4×6.4 mm. The final conductor consists of Rutherford cable coextruded with pure aluminum stabilizer measuring 4.93×20.0 mm for use in the outer, high current density portion of the solenoid, and 8.49×20.0 mm for the central, lower current density portion. The conductor is then wrapped in an insulating dry wrap fiberglass cloth which is vacuum impregnated with epoxy. The conductor has a total length of 10.4 km. The solenoid is indirectly cooled to 4.5K using a thermo-syphon technique. Liquid helium is circulated in channels welded to the solenoid support cylinder and maintains the low temperature.

The solenoid is located between the EMC and the Instrumented Flux Return

(IFR). The main magnet parameters are located in Table 2.2. The variation in the magnetic field is less than a few percent, which simplifies charged track reconstruction in the SVT and DCH. The field is large enough to provide sufficient momentum resolution; the 1.5 T field causes a 3 GeV/c particle to bend 3 cm before it reaches the outside of the DCH. The field uniformity is important since the tracks are assumed to move along helicies near the origin. Field non-uniformities are accounted in the track-fitting algorithms but not in the trigger and pattern recognition software.

2.9 The Instrumented Flux Return

The outermost *BABAR* detector system is the Instrumented Flux Return (IFR). It consists of layers of steel and resistive plate chambers (RPCs) and provides muon and neutral hadron identification. The iron of the magnet return yoke is used to filter charged hadrons and photons. The geometric layout and electronics of the IFR are described in sections 2.9.1 and 2.9.2, respectively. The performance of the IFR is summarized in section 2.9.3.

Several considerations were used in designing the IFR. Of highest importance is the fact that the IFR is the primary muon identification system, based on the assumption that they are the only charged particle capable of penetrating so far through the detector. This assumption arises from the fact that muons do not interact hadronically like pions or kaons and do not shower electromagnetically like electrons. In addition, the IFR provides detection of long-lived neutral hadrons, primarily K_L^0 and neutrons, which are observed as a small cluster of hits.

Penetration of the IFR varies with momentum, so the device is segmented non-uniformly. The RPCs are radially closer to the inner region of the detector than the outer region, improving performance for low momentum particles. To cover a wide range of solid angle, the IFR is divided into a barrel and two endcap regions. The endcaps allow the solid angle coverage to extend down to 300 mrad in the forward direction and 400 mrad in the backward direction.

2.9.1 IFR Layout

The geometric layout of the IFR is illustrated in Fig. 2.15. The primary unit of the IFR is the RPC, illustrated in Fig. 2.16. The electrodes are 2 mm plates of graphite-coated Bakelite, covered in PVC insulating film. One electrode is grounded while the other is held at 8 kV. The gap between each set of electrodes is filled with an argon-Freon-isobutane mixture. A charged particle entering the chamber ionizes gas molecules. This ionization induces pulses which are picked up by orthogonal aluminum strips on either side of the RPC.

The RPCs are interspersed between 18 layers of iron, yielding a total thickness of 65 cm in the barrel and 60 cm in the endcaps. The graded segmentation of the iron varies from 2 cm to 10 cm. The nine innermost plates are 2 cm, the next four are 3 cm, and the next three are 5 cm. The outer two plates are 10 cm thick in the barrel with one 5 cm and one 10 cm in the endcaps.

The barrel contains 21 active detector layers: two layers immediately outside the EMC and 19 layers alternating with the iron. The inner barrel layers are

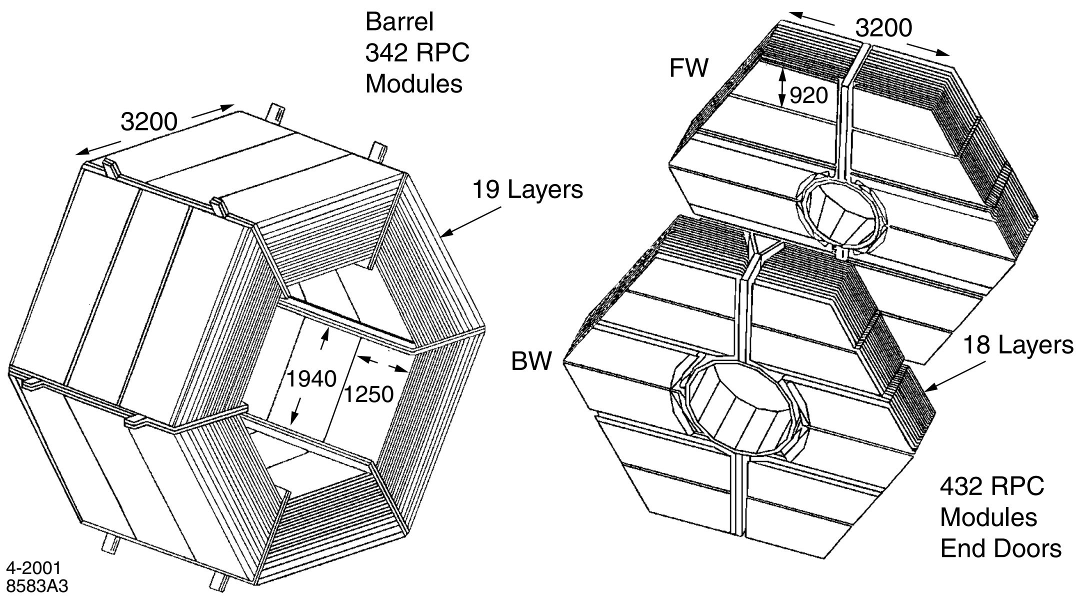

Figure 2.15: IFR schematic drawing, showing the gradation of the iron layers in the barrel (left) and endcaps(right). The measurements are given in units of centimeters.

cylindrical, consisting of eight chambers, arranged in two layers for maximum efficiency. They are intended to provide information about particles which lose most of their momentum in the calorimeter. Each cylindrical RPC covers one quarter of a 147 cm radius cylinder around the beamline.

All other RPCs are planar, each comprised of four chambers, and cover one sixth of the azimuth. The endcaps are hexagonal and are each divided into two vertical halves so that they can be separated and moved aside for detector access.

In the barrel, the readout strips that measure the z-coordinate have a pitch of 38.5 mm and those that measure the ϕ-coordinate vary from 19.7 mm to 33.5 mm. In the endcaps the strips measuring y position have a pitch of 28.4 mm and for

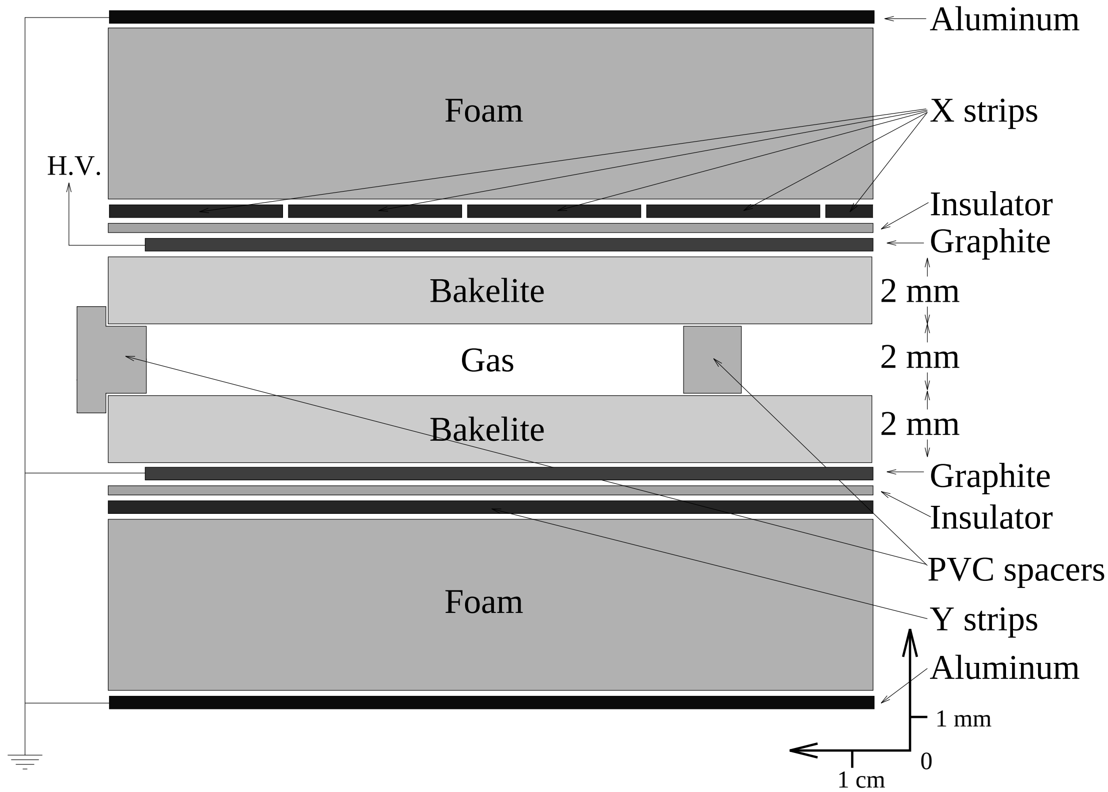

Figure 2.16: A schematic cross-sectional view of a *BABAR* RPC.

those that measure x position it is 38 mm.

2.9.2 IFR Readout and Reconstruction

The data from groups of 16 sixteen strips are passed to a Front End Readout Card (FEC), which then passes the data from active strips to a Time-to-Digital Converter (TDC). The TDC output is stored in buffers which allow for the trigger latency before being passed along optical fiber to the *BABAR* DAQ system.

Offline there are several steps that are performed on IFR data. As with other systems, feature extraction is performed to integrate the total charge and detect the leading edge of the pulse. A clustering algorithm joins pairs of adjacent chambers with hits into clusters. Clustering is done in both the $r-\phi$ and z views separately and then the 2D-clusters are joined into full 3D-clusters. Finally, a track-swimming algorithm is performed in which all charged tracks are projected into the IFR and cluster-matching is evaluated. Those clusters which do not associate with tracks are treated as neutral candidates.

2.9.3 IFR Performance

The performance of the IFR has degraded since the beginning of data-taking in *BABAR*, owing to several effects including early unchecked heating and response to PEP-II beam backgrounds. Fig. 2.17 shows the efficiency of the IFR modules. Some modules have completely failed while many others continue to degrade. A replacement of the front endcap occurred in late 2002 and complete replacement of the barrel with Limited Streamer Tubes (LST) [21] is planned for 2004-2006.

2.10 Online Electronics and Computing

Reliable and efficient recording of interesting events, which only occur at a rate of $\sim$ 100 Hz from a $\sim$ 250 MHz electron-positron collision rate, requires significant hardware instrumentation and software systems. Section 2.10.1 gives a brief overview of the data acquisition system, including the movement and processing of events by the system. Section 2.10.2 briefly outlines the trigger system, including both the hardware and the software triggers. A schematic overview of the online data processing system is shown in Fig. 2.18.

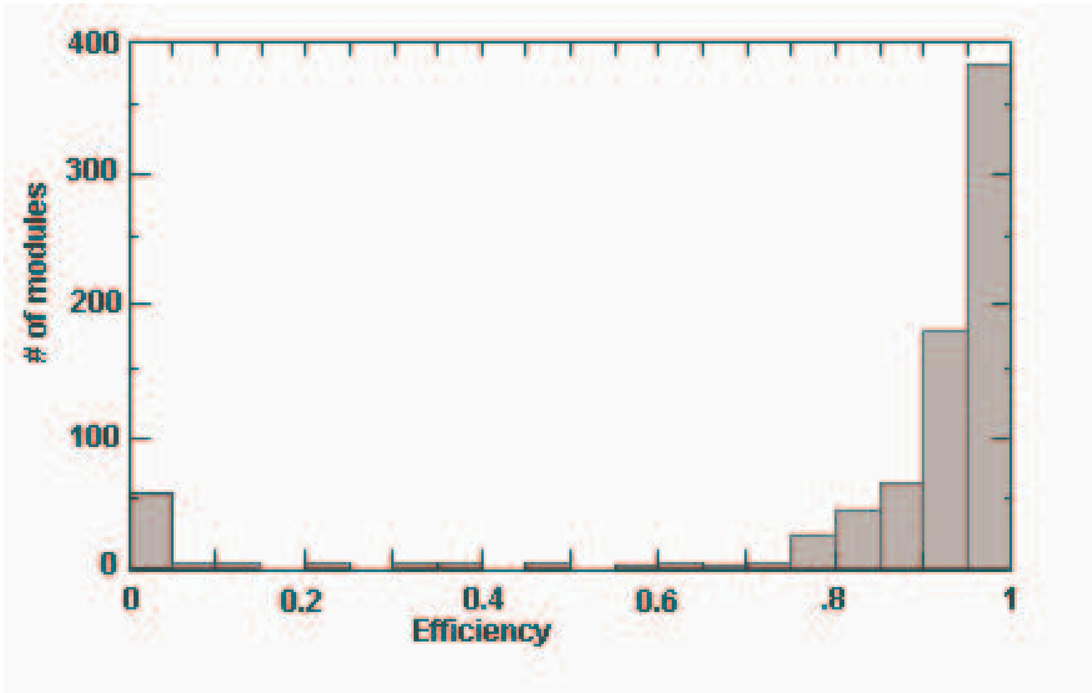

Figure 2.17: Histogram of the efficiency of IFR modules.

Each subsystem of the *BABAR* detector is instrumented with front-end electronics (typically a series of pre-amplifiers or digitizers that collect information from the active detector components). Information about a particular event is send from the front-end via fiber-optic cables from the detector, through the shielding wall to an *electronics house*. The electronics house contains processing systems for each subdetector as well as the Level 1 and Level 3 trigger systems. The digital information is collected and assembled for the trigger system, which decides whether the event contained interesting features. If the event is accepted, it is completely assembled (*event building*) and sent to the event store for use by physicists.

The main features of this data acquisition system are outlined in the following sections.

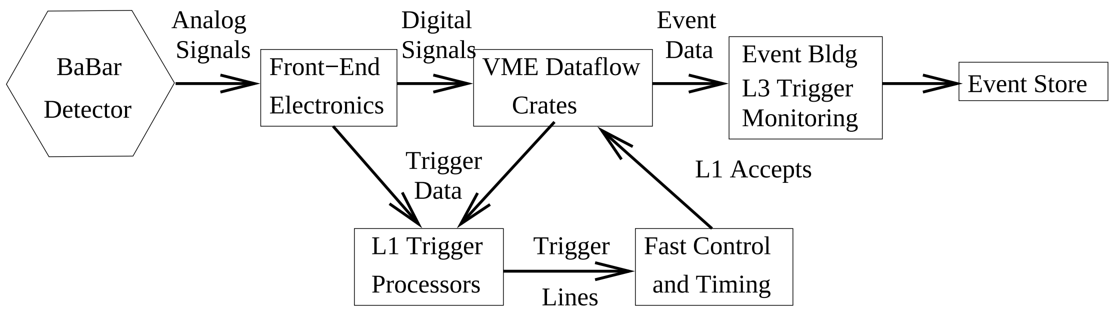

Figure 2.18: Schematic overview of the *BABAR* data acquisition and online systems.

2.10.1 The Data Acquisition System

An important feature of the B factory concept is that the high luminosity of the collider be complemented by low or little dead-time in the data acquisition system (DAQ). To this end the *BABAR* DAQ must work closely in concert with the trigger in order to insure low dead-times and efficient performance. The DAQ is made from several key systems, including those that insure rapid and error-free flow of data through the system (Online Dataflow) and those which receive events and process them for use in the Level 3 trigger decision (Online Event Processing).

2.10.1.1 Online Dataflow

The basic hardware unit of the DAQ system is the Read-Out Module (ROM), a VME-based[4] processor connected to the front-end electronics by 1.2 Gb/s fiber-optic links. The ROMs perform several tasks, including signal extraction from

[4]Versa Module EuroCard (VME), an open-ended bus standard.

raw data, gains and pedestal corrections, and regular calibrations of the front-end electronics. While the limit of the system's capabilities – due to bandwidth and processing speed – has been near 2 kHz, this limit has improved up to 4 kHz with enhancements such as higher bandwidth gigabit ethernet. These improvements are made in anticipation of the expected rapid increase in PEP-II luminosity over the next 3-5 years (from $5 \times 10^{33}\,\mathrm{cm}^{-2}\mathrm{s}^{-1}$ to $1 \times 10^{34}\,\mathrm{cm}^{-2}\mathrm{s}^{-1}$);

2.10.1.2 Online Event Processing

Data arrives in fragments to the ROMs, since each subdetector has a ROM that handles its electronics. The software trigger (Level 3) and eventual storage of events requires the combination of the information processed by the ROMs into a coherent whole. Online Event Processing (OEP) software is responsible for the coordinated assembly of an event from its fragments and communicates with the software trigger and the data logging management system. The requirements of its operations sets a limit of about 200 Hz on the data logging rate. Data is typically logged at 120 Hz, well below the limit.

2.10.2 The Trigger System

The trigger system is designed with two stages. The Level 1 trigger is performed in hardware using information collected from the front-end electronics. The Level 3 trigger is performed in software on a farm of 32 Personal Computers (PCs) [5]. Important features of these two systems are described in the following

[5] The original Level 3 computer farm consisted of 32 Sun PCs. The decision was made in 2001 to change to a farm of 32 Intel-based PCs using Linux. This has since scaled to 30 dual-

sections.

2.10.2.1 Level 1 Trigger

The Level 1 trigger system is a hardware-based trigger system. It uses information from three subsystems – the DCH, EMC and IFR – to make its decision. The trigger system is shown schematically in Fig. 2.19. The Level 1 trigger is broken into three trigger subsystems, one each for the DCH, EMC and IFR.

The Drift Chamber Trigger (DCT) uses all 7104 DCH channels to assemble clusters of cell hits into track segments (using the Track Segment Finder hardware, or TSF). The DCT then assembles track segments into full tracks (using the Binary Link Tracker, or BLT) and checks those tracks against preset transverse momentum thresholds (via the Drift Chamber PT Discriminator boards, or PTD). For tracks originating from the IP, the TSF is 97% efficient. For high-momentum tracks ($p_T > 0.8$GeV/c) the DCT is 94% efficient.

The Electromagentic Trigger (EMT) divides the EMC's crystals into 280 *towers* each containing 7×40 ($\theta \times \phi$) crystals. When the tower energy thresholds cross 20 MeV the bit for that tower is set and sent to the EMT. This occurs every 269 ns. Calorimeter Trigger Processor Boards (TPBs) convert the tower information into ϕ coordinate-based maps for use in the final trigger decision. The EMT is 99% efficient at triggering on energy clusters above 180 MeV, the

processor machines to stay ahead of the increasing luminosity. The online dataflow system has redesigned their data movement capabilities so that this farm's size can scale to accomodate PEP-II luminosity improvements.

average energy deposited by a minimum ionizing particle at normal incidence.

The IFR Trigger (IFT) is used primarily to trigger on $\mu^+\mu^-$ events and cosmic rays. The IFR is divided by the trigger system into 10 sectors: the six barrel sextants and the four half end doors. The IFT looks for groups of hits in IFR layers within 134 ns of each other. The IFT is 98% efficient at triggering on events with at least one track that crossed through the IFR and 73% efficient at triggering on events with two such tracks.

Information from the DCT, EMT and IFT is assembled and passed to the Global Level Trigger (GLT). Here, user-defined trigger masks selecting patterns of tracks, energy clusters and IFR hits are used to accept or reject events based on their pattern of trigger bits. These masks can be changed at any time to include new restrictions on track energy, neutral cluster energy and association with tracks and IFR hit matching to DCH tracks and EMC clusters. GLT information is sent to the Fast Control and Timing System (FCTS), where prescales can be applied to different trigger configurations in preparation for the final trigger decision. The FCTS makes the final trigger decision and informs the subsystems to send their event information to the Level 3 farm.

The Level 1 system delivers triggers at a rate of 1kHz. Out of this total rate, Bhabha and annihilation physics contributes 130Hz. Cosmic rays contribute 100Hz and random beam-crossing triggers contribute 20Hz. Much of the remaining triggers are due to lost particles interacting with the beam pipe or other components. For $B\overline{B}$ events the trigger is $> 99.9\%$ effient. For particular rare B

decay modes with low multiplicity, such as $B^0 \to \pi^0\pi^0$ or $B^+ \to \tau^+\nu_\tau$, the Level 1 trigger is 99.7% efficient.

2.10.2.2 Level 3 Trigger

The Level 3 trigger is a software-based trigger which performs a full event reconstruction and classification. The trigger is performed in three stages. In the first stage, events are classified according to the trigger information from the FCTS. In the second stage, a large set of *BABAR* event reconstruction algorithms are applied to the event to find quantities of interest. Filters are applied to determine whether the quantities satisfy a set of selection criteria. The last stage creates the Level 3 output information, a set of classifications for each event. Not only are events consistent with hadrons, charm, and τ kept, but also Bhabhas and $\mu^+\mu^-$, cosmic rays, and random triggers (for calibration purposes).

For a typical run on the $\Upsilon(4S)$ peak with a luminosity of $2.2 \times 10^{33}\mathrm{cm}^{-2}\mathrm{s}^{-1}$, the Level 3 event composition is tabulated in Table 2.3. The desired physics events contribute 13% of the total output (120Hz) while the calibration and diagnostic sample contributes 40%.

2.11 Charged Particle Identification

Each event collected by the *BABAR* detector contains lists of particles which can be used in physics analyses. The charged particles which interact with the *BABAR* detector are pions, kaons, electron, muons, and protons. The most abundant of these are the pions; most B decays produce at least one pion, if not many

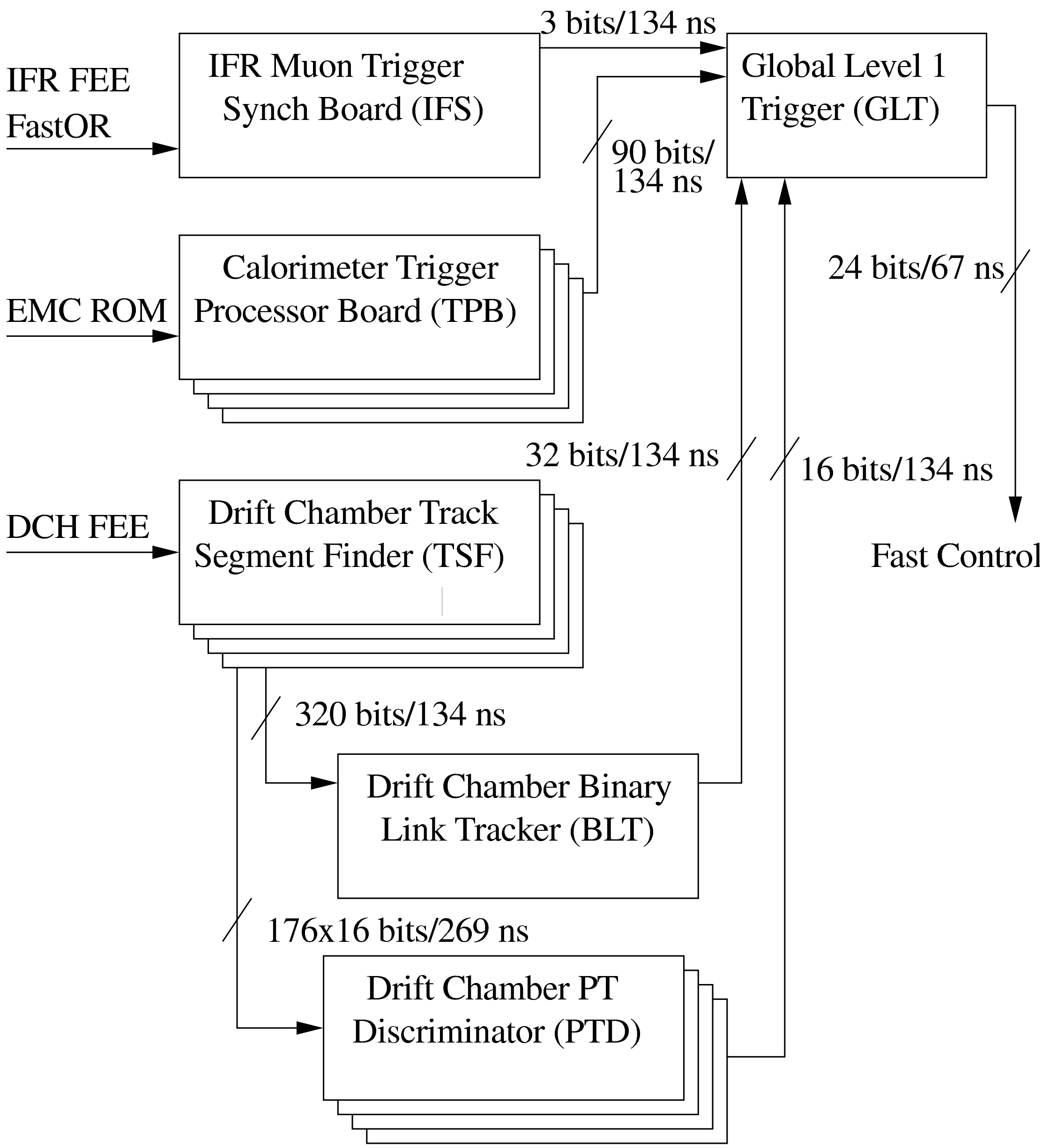

Figure 2.19: A schematic of the Level 1 trigger system. The DCH, EMC and IFR information is assembled by the trigger system and sent to the fast control and timing system (FCTS) to determine whether an individial event is passed to Level 3.

Table 2.3: The composition of the Level 3 physics trigger output.

Event Type	Rate (Hz)
Hadrons, $\tau\tau$ and $\mu\mu$	16
Other QED, 2-photon events	13
Unidentified Bhabha background	18
Beam-induced backgrounds	26
Total Physics accept	**73**
Calibration Bhabhas ($e^+ \ e^-$)	30
$\gamma\gamma$, Radiative Bhabhas ($e^+e^-\gamma$)	10
Random triggers and cosmic rays	2
L1, L3 pass through diagnostics	7
Total calibration/diagnostics	**49**

more. The default hypothesis for all charged tracks is the pion hypothesis. However, each charged track can be tested against any of the five particle hypotheses common to *BABAR*: electron, muon, kaon, proton, or pion. As described in the following sections, information from the various detector systems can be combined to aid in the testing of each hypothesis.

2.11.1 Kaon Identification

Kaon identification has been studied extensively by the *BABAR* collaboration[22]. Kaons have a distinctive dE/dx distribution in the momentum range below 0.7 GeV/c. This momentum region relies on the performance of the DCH in measuring dE/dx. Above 0.7 GeV/c, kaons have a distinctive Cherenkov cone angle. The use of both the DCH and the DIRC to identify kaons is critical to high quality kaon selection. As discussed in Section 2.6.3, the DIRC provides excellent $K-\pi$ for kaons with momenta up to 4 GeV/c^2.

Kaons are selected by comparing the likelihood ratios for kaons, pions and protons ($\mathcal{L}_K$, $\mathcal{L}_\pi$, and $\mathcal{L}_p$). These likelihood ratios use the predicted behavior of the detector components for each particle hypothesis to gauge the conistency of a particle with a given hypothesis. The momentum of the charged particle determines whether the SVT and DCH, only the DCH, or only the DIRC are used to construct the likelihood ratios. Table 2.4 lists the kaon selection criteria used in different parts of the analysis. Figure 2.20 illustrates the efficiency and purity of the "kVeryLoose" selection. Kaon identification is not possible below 300 MeV/c simply because there is insufficient dE/dx information to make a determination. The efficiency falls between 0.5 GeV/c and 0.9 GeV/c until the DIRC is able to contribute good information about the Cherekov angle. Above 2 GeV/c, the Cherenkov angles for kaons, pions, etc. become less distinguishable, resulting in a drop in efficiency. The pion misidentification rate is stable across all momenta, rising above 2 GeV/c for the reasons mentioned.

A neural network-based kaon identification is also used in parts of the present work. The particle identification tool, called "K-Net", is a track-based neural network that determines how compatible each track is with being a kaon. To make this decision it uses the momentum of the track and the likelihood ratios,

$$L = \frac{\mathcal{L}_K}{\mathcal{L}_K + \mathcal{L}_\pi}, \tag{2.5}$$

each calculated using the likelihoods from either the SVT, DCH or DIRC. The K-Net is trained with true kaons versus all other charged particles. After it has been trained the K-Net produces an output for a given track that ranges between

Table 2.4: Definition of the various kaon selection criteria.

Criteria	"kVeryLoose"		
Momentum (GeV/c)	< 0.5	[0.5,0.6]	> 0.7
Use SVT	yes	no	no
Use DCH	yes	yes	no
Use DIRC	no	no	yes
$\mathcal{L}_K/\mathcal{L}_\pi$	> 0.1	> 1	> 1
OR $\mathcal{L}_p/\mathcal{L}_\pi$	> 0.1	> 1	> 1

zero (not a kaon) and one (compatible with a kaon). Selecting different quality samples of kaons corresponds to placing a restriction at different points in the range of the K-Net's output. These restrictions are chosen so that the purity is the same as that of the cut-based selector described above for each category (e.g. "kVeryLoose"). The selection criterion for the K-Net used in this analysis is designated as "knnVeryLoose" and is defined by the requirement that the neural network output be > 0.45 for a kaon candidate.

2.11.2 Muon Identification

Muons are identified using several of the *BABAR* subsystems. Muons have a minimum ionizing signature in the EMC. They tend to lose about 200 MeV of energy, regardless of their momentum. Due to the intermittent performance of the IFR, this requirement is designated as "muMinIon" and only uses EMC information. Muons also leave a pattern of penetrating hits in the IFR. The identification of a muon using the IFR proceeds by calculating the likelihood of an observed pattern in the IFR under the hypothesis that the track was a muon.

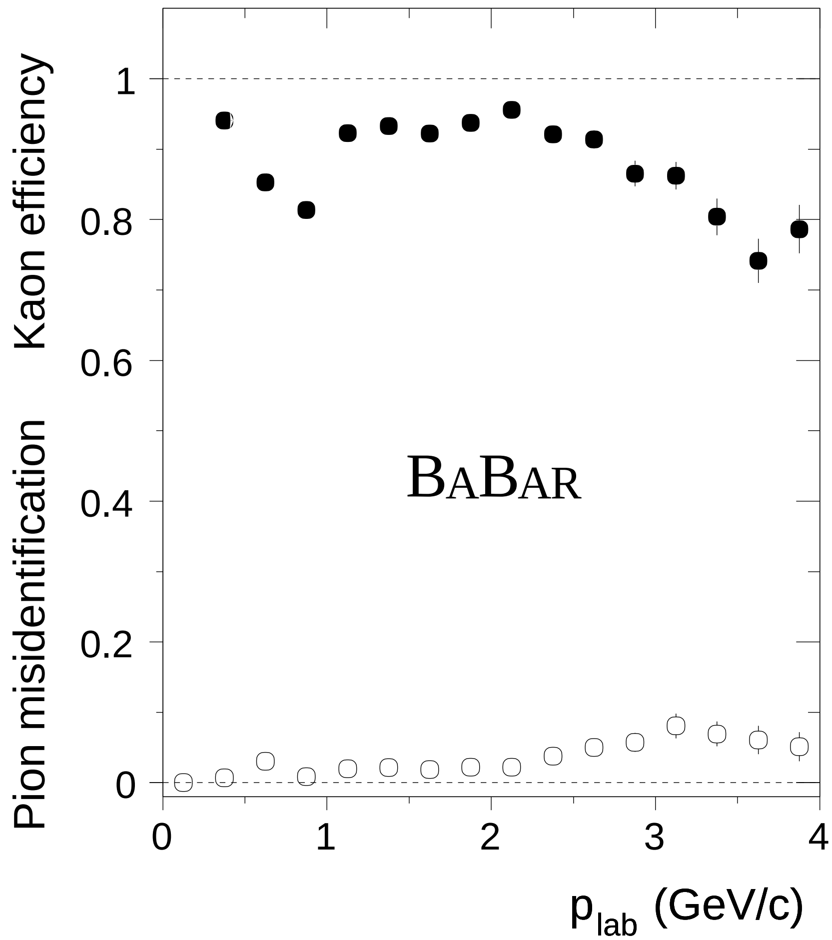

Figure 2.20: The efficiency and the pion misidentification rate of the "kVeryLoose" selection as a function of momentum in the laboratory reference frame.

The specific variables used are:

- n_λ and Δn_λ, the number of hadronic interaction lengths traversed by the candidate and the difference between that number and that expected for a muon of the same energy and momentum;

- $\bar{n}_{hits}$ and σn_{hits}, the mean and variance of the number of hits per RPC layer; these are used to reject hadronic interactions;

- the quality of the fit for fitting a track to the IFR hits (χ^2_{trk}) and fitting the hit pattern for self-consistency (χ^2_{fit})

Table 2.5: Definitions of muon selection criteria.

Criteria	"muMinIon"	"muVeryLoose"	"muLoose'	"muTight"	"muVeryTight"
E_{EMC}(GeV)	< 0.4	< 0.5	< 0.5	< 0.4	< 0.4
n_λ	-	> 2.0	> 2.0	> 2.2	> 2.2
Δn_λ	-	< 2.5	< 2.0	< 1.0	< 0.8
$\bar{n}_{hits}$	-	< 10	< 10	< 8	< 8
σn_{hits}	-	< 6	< 6	< 6	< 6
χ^2_{trk}/n_{lay}	-	-	< 7.0	< 5.0	< 5.0
χ^2_{fit}/n_{lay}	-	-	< 4.0	< 3.0	< 3.0

Table 2.5 lists the increasingly restrictive sets of criteria used to define muons in the present work. The efficiency for the "muLoose" selection is shown in Fig. 2.21. The efficiency of identifying muons drops significantly below 1 GeV/c, since they are unable to reach the IFR. The efficiency increases and then stabilizes at 86% above 2 GeV/c. The rate of pion mis-identification also increases above 2 GeV/c, since the pions are able to penetrate into the IFR (but tend to suffer

strong interactions with the material in the IFR, giving them a different pattern of hits).

The efficiency is shown as a function of polar angle in Fig. 2.21b. The effiency is flat over most of the angular coverage of the IFR. There are several points (notably $\theta \approx 90^\circ, 120^\circ$) where the efficiency suddenly drops due to gaps in the interface between sections of the IFR.

2.11.3 Electron Identification

Electron identification is performed by combining information from several subdetectors, including the DCH, EMC, and DIRC. Electrons tend to lose a significant amount of energy as they traverse the tracking system. They also tend to deposit all of their energy in the calorimeter. To isolate such behavior, the following quantities are constructed:

- Energy loss as measured by the DCH (dE/dx);
- The number of photons associated with the Cerenkov ring in the DIRC (N_γ);
- The lateral distribution of energy in the EMC (LAT);
- The (4,2) Zernike moment of the energy distribution ($A42$);
- The number of crystals occupied by the shower in the calorimeter (N_{Xtal});
- The ratio of the energy deposited in the calorimeter to the momentum of the track (E/p).

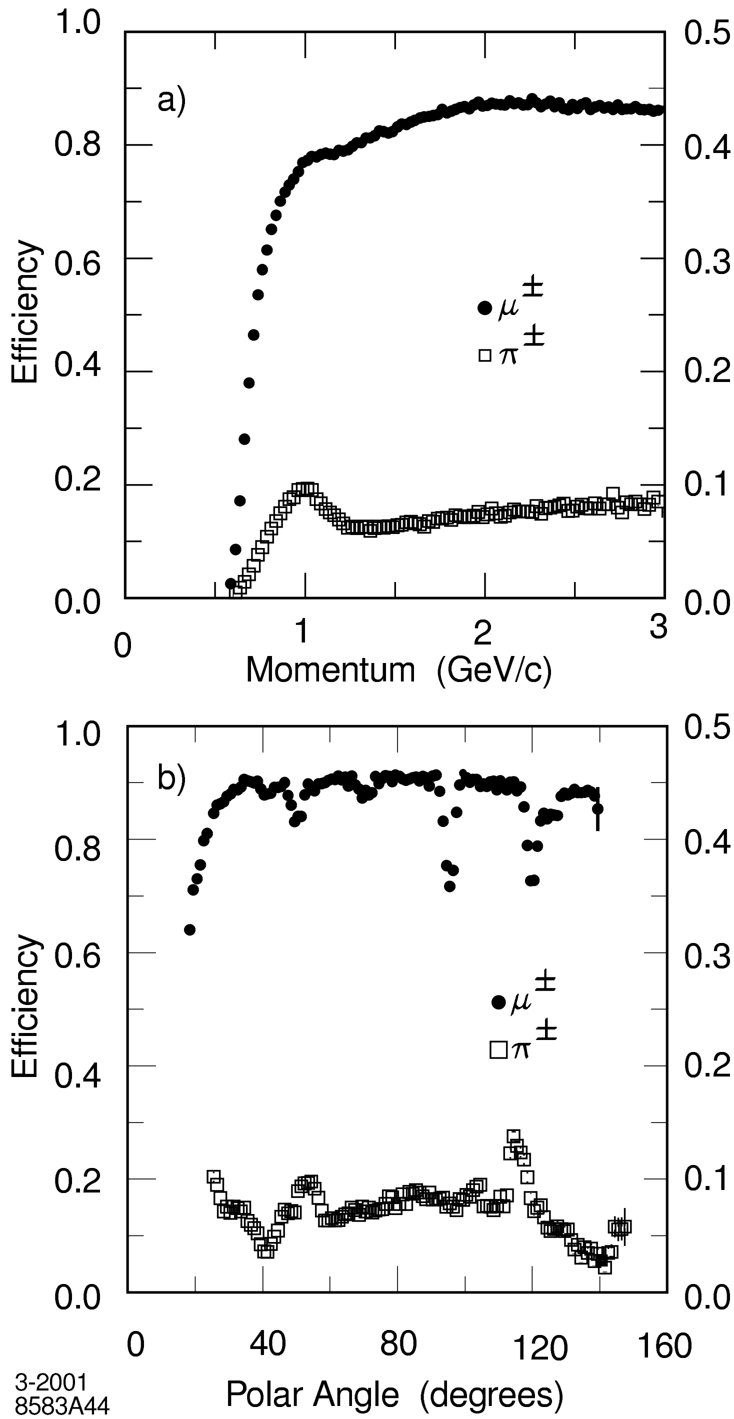

Figure 2.21: The efficiency and the pion mis-identification rate of the "muLoose" selection as a function of momentum (top) and polar angle (bottom). The left vertical scale is the muon selection efficiency and the right vertical scale is the pion mis-identification rate.

Electromagnetic showers in the EMC have a different signature than showers of hadronic interactions resulting in different longitudinal and lateral energy distributions. Two lateral shower shapes are currently in use, LAT and $A42$, described below.

The lateral energy distribution (LAT) was introduced at ARGUS [23] and is defined as

$$LAT = \frac{\sum_{i=3}^{n} E_i r_i^2}{\sum_{i=3}^{n} E_i r_i^2 + E_1 r_0^2 + E_2 r_0^2}, \quad E_1 \geq E_2 \geq ... \geq E_n \tag{2.6}$$

where the sum extends over all the crystals in a shower; $r_0 = 5\,\mathrm{cm}$, the average distance between two crystal frontfaces, and r_i is the distance between crystal i and the shower center (calculated as the center of gravity with *linear* energy-weighting of every crystal). Electromagetic showers tend to deposit most of their energy in one or two crystals, and LAT therefore tends toward smaller values for electromagentic showers.

Hadronic showers tend to be more irregular than electromagentic showers. This feature is exploited by expanding the lateral shower shape in terms of Zernike moments (first introduced at ZEUS [24]):

$$A_{n,m} = \sum_{r_i \leq R_0}^{n} \frac{E_i}{E} \cdot f_{nm}(\frac{r_i}{R_0}) \cdot e^{-im\phi_i}, \quad R_0 = 15\,\mathrm{cm} \tag{2.7}$$

$$f_{nm}(\rho_i \equiv \frac{r_i}{R_0}) = \sum_{s=0}^{(n-m)/2} \frac{(-1)^s (n-s)! \rho_i^{n-2s}}{s!((n+m)/2-s)!((n-m)/2-s)!}, \tag{2.8}$$

with $n, m \geq 0$ integers, $n-m$ even and $m \leq n$. Zernike moments are used because they provide an expansion independent of the orientation of the lateral coordinate system (in which ϕ_i is measured). The azimuthal variation in shower shape enters only for moments with $m \geq 2$, *e.g.*, in $|A_{42}|$, the only Zernike moment used in electron identifiction.

Energy loss is determined from the DCH as discussed in section 2.5. Electrons tend to have a dE/dx between 500 and 1000. Electrons also tend to have a shower shape (LAT) between 0.1 and 0.5 and a Zernike moment below 0.1. These showers typically include at least three crystals. Since electrons interact entirely within the calorimeter, depositing all of their energy, they have a typical energy-momentum ratio (E/p) peaking at 1.0.

The selection of electrons proceeds by making restrictions on the above quantities. Different quality levels are achieved by tightening or relaxing restrictions on the quantities. The two levels of electron selection used in this analysis are referred to as *eTight* and *eVeryTight*, defined in table 2.6.

Table 2.6: The restrictions placed on quantities that are used to select electrons.

Selector Level	dE/dx	N_{Xtal}	E/p	LAT	$A42$	$\Delta\phi$	DIRC
eTight	500 ... 1000	> 3	0.75 ... 1.3	0.0 ... 0.6	-10. ... 10.	no	no
eVeryTight	540 ... 860	> 3	0.89 ... 1.2	0.1 ... 0.6	-10. ... 0.11	yes	yes

The effiency and mis-identification rate for the eVeryTight electron selection are shown in Fig. 2.22. The average efficiency is 91.5% for electrons with $p > 1\,\mathrm{GeV}$ and the pion mis-identification rate is $\approx 0.13\%$.

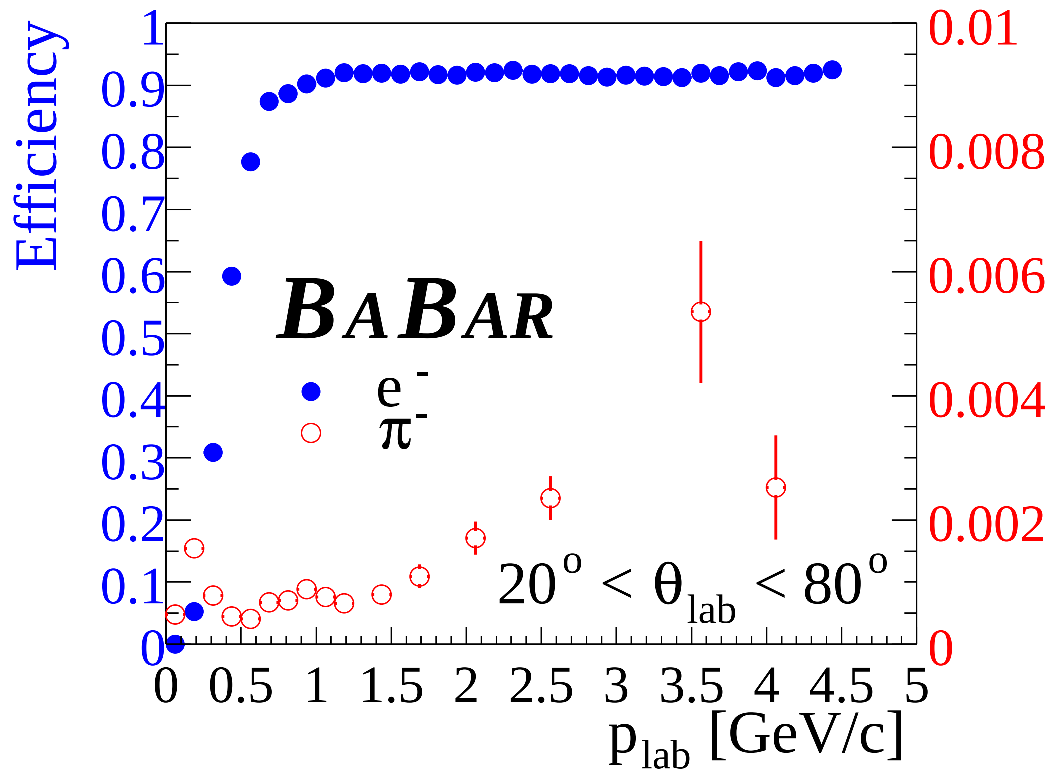

Figure 2.22: The selection efficiency (blue dots) and pion misidentification rate (red circles) as a function of lab momentum for the eVeryTight selection criteria. The control sample used to obtain electrons is radiative Bhabha events, while the pion control sample comes from 1-prong tau decay recoiling against 3-prong tau decay in $e^+e^- \to \tau^+\tau^-$.

Chapter 3

Data and Monte Carlo Samples

The *BABAR* detector began taking data in the summer of 1999. In the period between 1999 and the summer of 2002 the experiment collected $81.9\,\mathrm{fb}^{-1}$ of data at the $\Upsilon(4S)$ resonance ("on-resonance") and $9.7\,\mathrm{fb}^{-1}$ at a point 40 MeV below the $\Upsilon(4S)$ resonance ("off-resonance"). The cross-sections for different $e^+\,e^-$ reactions at the $\Upsilon(4S)$ resonance are listed in Table 3.2. The experiment takes data off the resonance to remove the contributions from $\bar{b}$ events, allowing for the study of contributions from other $e^+e^- \rightarrow f\bar{f}$ processes (where f is any fermion except the bottom quark).

The *BABAR* experiment also generates and maintains a large ensemble of Monte Carlo simulations. The ratio of Monte Carlo to data is typically 2 : 1 to reduce statistical uncertainty when developing an analysis using simulations. The present work is developed from a simulation of the signal process, as well as a generic ensemble of background processes. Comparisons are performed between data and simulation wherever possible to determine if there are systematic

Table 3.1: Data samples broken down by year

	Luminosity (fb^{-1})	
Year	On-Resonance	Off-Resonance
1999	0.47	0.0
2000	20.2	2.6
2001	35.6	3.8
2002 (Jan.-July)	25.6	3.2
Total	81.9	9.6

Table 3.2: Production cross-sections at $\sqrt{s} = M_{\Upsilon(4S)}$. The e^+ e^- cross- section is the effective cross-section, expected within the experimental acceptance.

$e^+e^- \rightarrow$	Cross-Section ($pb \times 10^6$)
$\bar{b}$	1.08
$c\bar{c}$	1.30
$s\bar{s}$	0.35
$u\bar{u}$	1.39
$d\bar{d}$	0.35
τ^+ τ^-	0.94
μ^+ μ^-	1.16
e^+ e^-	~ 40

differences between the two.

3.1 The *BABAR* Data Set

The data samples, divided by year, are listed in Table 3.1. The period from 1999-2000 is referred to as "Run 1", while the period from 2001-2002 (summer) is referred to as "Run 2". This work uses the complete on-resonance and off-resonance samples from Runs 1 and 2.

Data quality is maintained by the *BABAR* collaboration using a set of quality assurance criteria which operate at all stages of data-taking (during data-taking, during data processing, and during data storage). The experiment has collected much more data than is useable. There are occasional periods of data-taking when the detector encounters problems. This data is flagged by the shift crew for later examination by detector experts.

Often, problems with a period of data can be addressed at the time the data is processed. If the solution is too expensive or time consuming, then the data is not flagged as useable. After data processing, it is the job of the *BABAR* Run Quality Manager (RQM) to make final decisions regarding data quality. The sample which is deemed high quality is used by physicists for data analysis. For the period 1999-2002, $81.9\,\mathrm{fb}^{-1}$ of on-resonance and $9.7\,\mathrm{fb}^{-1}$ of off-resonance data are marked by the RQM for use in analyses.

The smallest unit of the data is an "event" (a single trigger stored to disk). Events collected durng a single, contiguous time period during which the *BABAR* DAQ was in constant operation is referred to as a "run". A run contains at least 10,000 events and usually lasts no more than two hours. The standards to which the data in a run are held in order to be considered useable are as follows:

1. The electron and positron beams are in collision for the duration of the run,
2. all *BABAR* detector subsystems are in operating nominally, meaning that no single system was suffering problems which prevented it from taking high-quality data,

3. the global data quality flag is set to ”good”, meaning that the shift crew and RQM determined that there was no detrimental circumstance during the run,

4. the recorded luminosity is > 0, and

5. the run was successfully processed and reconstructed.

A large ensemble of runs taken between two significant detector shutdown periods is referred to as a “Run”.

3.2 *BABAR* Monte Carlo Simulations

The simulation of physics processes is performed in a number of stages by the *BABAR* Simulation Production (SP) group. All Monte Carlo simulations (MC) which are to be used for official results must be performed by this group. Requests for specific simulations and sample sizes are made by the *BABAR* working groups to the SP group. The Monte Carlo produced from 2000-2002 for comparison with Run 1 and Run 2 data is referred to as SP4 (the fourth simulation production run).

The stages of the Monte Carlo production are described in the following sections.

3.2.1 Event Generation

The first stage of the simulation is to generate four-vectors for the physical process. This is done by a variety of `C++` and `FORTRAN` software packages which have been developed over several decades. This software is managed by a single *BABAR* application, called `GenFwkInt` (Generators Framework Interface) [25]. $B^0\overline{B}^0$ events, for example, are simulated by the routine `EvtGen` (*Event Generator*) which is part of the GenFwkInt framework package. Other events which are routinely generated are $\mu^+\mu^-$ and Bhabha scattering. The generator simulates the spread of energies allowed in the PEP-II beam collisions to determine the energy available to the resulting particles. The underlying four-vector generators are detailed in [25].

3.2.2 Detector Geometry Simulation

Once the four-vectors of the process are generated the particles are propagated through a material model of the *BABAR* detector. In addition to a simulation of interactions with material, the simulation of secondary decays are also performed during this stage. The simulation is performed by an application called `BOGUS` (*BABAR* Object-oriented Geant4-based Unified Simulation)[26], which as its full name implies is built on the `GEANT4` (GEometry ANd Tracking) simulation toolkit [27].

As the particles pass through sensitive regions of the detector, energy, charge and angle information is used to calculate positions and idealized energy deposits in the detector. These quantities, referred to as "GHits" are stored in persistent containers in the Objectivity database for later use in calculating the detector response. While `GEANT4` provides particle transport algorithms, the *BABAR* collaboration has developed its own routines.

3.2.3 Detector Response and Background Mixing

At this stage idealized GHits are retrieved from the database and digitized, that is, transformed into realistic signals which mimic those collected from the detector electronics. Real background events, stored in the database, may be mixed in with the simulated event to more closely reproduce signal data. The digitized background event is aligned in time with the simulated signal event before they are combined. The final outcome from this stage is a set of raw data objects called "digis" which are stored in the database for the reconstruction phase. These functions are performed by the `SimApp` application. Once the detector response has been calculated and background mixed in, the Level 1 and Level 3 trigger conditions are applied to the event.

This stage produces an event containing raw subdetector hit information, much like real data coming from the real *BABAR* detector. The final stage of the simulation applies the full *BABAR* event reconstruction algorithms for finding charged particles and identifying neutral objects.

3.2.4 Monte Carlo Simulation Samples Used in this Analysis

The samples of Monte Carlo simulations used in this analysis are outlined in Table 3.3. The term "generic" means that the final state of the decay is not constrained, so any final state (with its proper branching fraction) is allowed. Signal Monte Carlo simulations contain one B meson which decays generically

Table 3.3: Monte Carlo simulation samples used in the work. The cross-sections for all species except $B\overline{B}$ are taken from *The BaBar Physics Book* [28]; the $B\overline{B}$ cross-section is obtained by dividing the number of data $B\overline{B}$ events by the data luminosity and assuming that the production of B^+B^- and $B^0\overline{B}^0$ is equal. To obtain the signal luminosity, a branching fraction of 1×10^{-4} is assumed.

Data set	Number of events	Luminosity [fb^{-1}]	Cross-section [nb]
B^+B^- generic	120M	224	0.54
$B^0\overline{B}^0$ generic	134M	249	0.54
$B^- \to X, B^+ \to \tau^+\nu_\tau$ (Signal Mode)	495k	4583	-
$c\overline{c}$	112M	86	1.30
$u\overline{u}, d\overline{d}, s\overline{s}$	165M	79	2.10
$\tau^+\tau^-$	77M	82	0.94

and a second B meson which decays to $\tau^+\nu_\tau$. The τ^+ is then allowed to decay into any of its final states.

3.2.4.1 Modeling Particle Identification Efficiencies ("PID Killing")

Particle identification has been studied by the *BABAR* collaboration using sets of control samples developed from data. The use of these control samples has led to the development of particle identification tables ("PID Tables") which contain the efficiency of the particle identification as a function of momentum (p_{lab}), zenith (θ_{lab}), and azimuthal (ϕ_{lab}) angle in the laboratory reference frame. There are tables for each particle type and for each level of selector quality. The PID tables are used to correct the MC particle selector efficiencies using a process called "PID Killing".

The PID killing method begins by determining the true identity of charged particles in a simulated event. It then loads the PID table relevant to that particle type. Using the reconstructed p_{lab}, θ_{lab}, and ϕ_{lab} the weight for that particular charged particle is determined from the PID table. A random number is then thrown between zero and one; if the number is less than the weight, the charged track is assigned to be identified as a particle of its true type at the selector level associated with the table.

Using this process, the particle identification quality in data should be reproduced in simulation. PID killing is applied directly to the all Monte Carlo samples (signal and background) after they are generated to reproduce the selector efficiency in data. This is critical in order to bring the Monte Carlo and data PID efficiencies into agreement. Time-dependent effects, such as the degradation of the IFR RPC efficiency (Section 2.9.3), is not directly modeled in the simulation. Such effects are included through the PID killing methodology.

Chapter 4

Tagging Events Using Semi-Leptonic B Meson Decays

4.1 The Strategy for the Search for $B^+ \to \tau^+\nu_\tau$

The PEP-II collider produces the $\Upsilon(4S)$ resonance which then decays exclusively to a pair of B mesons (either B^0 $\overline{B}^0$ or B^+ B^-). The challenge to the search for $B^+ \to \tau^+\nu_\tau$ is the presence of many neutrinos in the final state, since neutrinos cannot be detected by *BABAR*.

In order to reduce contributions from false positives, this analysis proceeds by first isolating a subsample of events where one of the B mesons decays into a reconstructable final state with nearly all particles accounted. This process is referred to as *tagging* the B meson using a particular final state or set of final states. After isolating this tag B meson, the remaining charged and neutral particles are required to be consistent with the process $B^+ \to \tau^+\nu_\tau$. In this work, the tag B meson is isolated in a semi-leptonic, open-charm mode $B^- \to D^0\ell^-\overline{\nu}_\ell X$ (where

X is either a photon, π^0 or nothing). The search for $B^+ \to \tau^+\nu_\tau$ then proceeds by attempting to identify a τ^+ decaying to $\ell^+\nu_\ell\overline{\nu}_\tau$, where ℓ^+ is either a muon or an electron.

The events of interest to this work are illustrated in Fig. 4.1. The first step in this analysis is to identify neutral D-mesons (D^0) by combining charged particles (pions and kaons) and composite light mesons (π^0 and K_S^0). The D^0 mesons are then paired with leptons (muons or electrons) and examined to determine their consistency with having come from B^- decay. After constructing this tagged subsample, constraints are placed on the remaining particles (referred to as the "recoil") to determine if it is consistent with $B^+ \to \tau^+\nu_\tau$. The particles which recoil against the $B^- \to D^0\ell^-\overline{\nu}_\ell X$ decay are said to be on the *signal side* of the event.

4.2 The Motivation for Using $B^- \to D^0\ell^-\overline{\nu}_\ell X$

Since the process $B^+ \to \tau^+\nu_\tau$ is predicted by the Standard Model to be rare, the sample of B mesons from which the search begins must have inherently high statistics. The choice of the final state(s) of the tag B meson is critical in obtaining a statistically meaningful sample size.

As discussed in 1.3.3, the search for $B^+ \to \tau^+\nu_\tau$ proceeded at CLEO by tagging one B meson in a set of hadronic final states and requiring the remainder of the event be consistent with $B^+ \to \tau^+\nu_\tau$ (See Section 1.3.3). There is also a search in parallel with this work performed at *BABAR* which uses a collection of

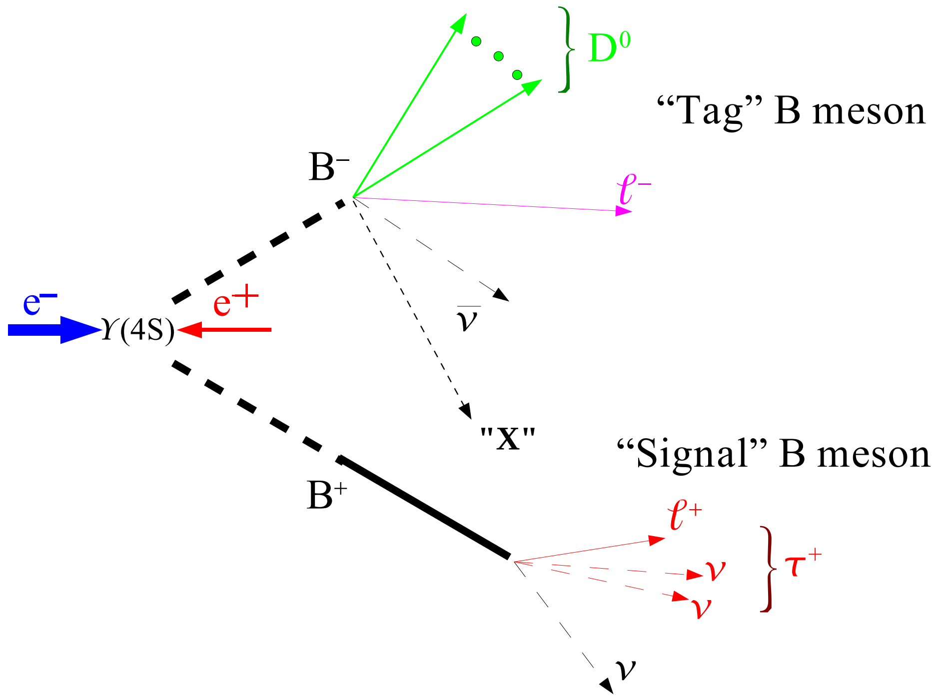

Figure 4.1: The events of interest to the present work. The *tag* B meson decays semi-leptonically, with its D-meson subsequently decaying into a number of hadrons. The *signal* B meson decays into $\tau^+\nu$. The τ^+ then decays into a charged lepton and a pair of neutrinos. The "X" can be a photon or π^0 from the decay of higher-mass D^0 states (as in $B^- \to D^{*0}\ell\nu$), or it can be nothing at all (as in $B^- \to D^0\ell\nu$).

fully-reconstructed hadronic B meson final states [29].

For this work, a completely unique approach is used to tag one of the B mesons. Here, the tag B meson is reconstructed using semi-leptonic, open-charm modes because of the high inherent branching fractions of these processes. They are referred to as "semi-leptonic, open-charm" states because only a part of the final state is a lepton and the other part is a D meson, which possesses net charm. As illustrated in Table 4.1 these modes account for $\sim 10\%$ of the B^- meson's

Table 4.1: Decay modes of the B meson that can contribute to $B^- \to D^0\ell^-\overline{\nu}_\ell X$.

Decay Mode	Fraction (%)
$B^- \to D^0\ell^-\overline{\nu}$	2.15 ± 0.22
$B^- \to D^{*0}\ell^-\overline{\nu}$	6.5 ± 0.5
$B^- \to D_1\ell^-\overline{\nu}$	0.56 ± 0.16
$B^- \to D_2^*\ell^-\overline{\nu}$	< 0.8
Total	10.0 ± 0.6

branching fraction.

The reconstruction of the tag B meson is semi-exclusive, meaning that that the neutrino cannot be detected and the D^0 meson is not required to be paired with a photon or π^0 to exclusively reconstruct higher-mass states of the D meson. The presence of higher-mass D meson resonances is allowed in this analysis by other means which are discussed in section 4.5. This choice was made because of the low efficiency of reconstructing these exclusive higher-mass D^0 states. They are not explicitly pursued in this work (due to the softness of the π^0 spectrum and the inefficiency of vertexing a π^0 with a D^0.)

To help efficiently isolate the decay process $B^- \to D^0\ell^-\overline{\nu}_\ell X$, the *BABAR* collaboration has developed a software package called `BToDlnuXUser` [30]. It is used to perform the reconstruction of the $D\ell$ candidates. Further constraints are then placed on these events (after processing the data and Monte Carlo with `BToDlnuXUser`) to improve the quality of the analysis. Events are first preselected based on some very loose criteria. The selection of $D\ell$ candidates proceeds by building up the D^0 mesons from charged particles (discussed in Section 2.11) and light mesons. The reconstruction of relevant light mesons is discussed in the next section, followed by a description of the event selection and the refinement process.

4.3 Light Meson Reconstruction

4.3.1 K_S^0 Reconstruction

The K_S^0 s used in this analysis are reconstructed entirely as $K_S^0 \to \pi^+\pi^-$. All pairs of oppositely charged tracks are vertexed, but no restriction is placed on vertex quality or convergence. The tracks are assigned the pion mass and the invariant mass of the tracks is calculated at the vertex. If the vertexing of the tracks did not succeed, then the invariant mass is calculated from the track four-vectors at the origin. The invariant mass of the pair is required to lie within 0.25 GeV of the nominal K_S^0 mass (497.648 MeV/c^2).

4.3.2 π^0 Reconstruction

The reconstruction of neutral pions in *BABAR* has been extensively studied by the collaboration [31]. There are two classes of neutral pions in the *BABAR* detector. In one case, π^0 are observed as a single cluster (*merged*) and occur at higher energy. In the other, the π^0s can be formed by combining two separate photons (*composite*).

4.3.2.1 Composite π^0

The composite π^0 selection begins by combining two distinct neutral clusters (assumed to be photons). The photons must each be well identified, with a lateral

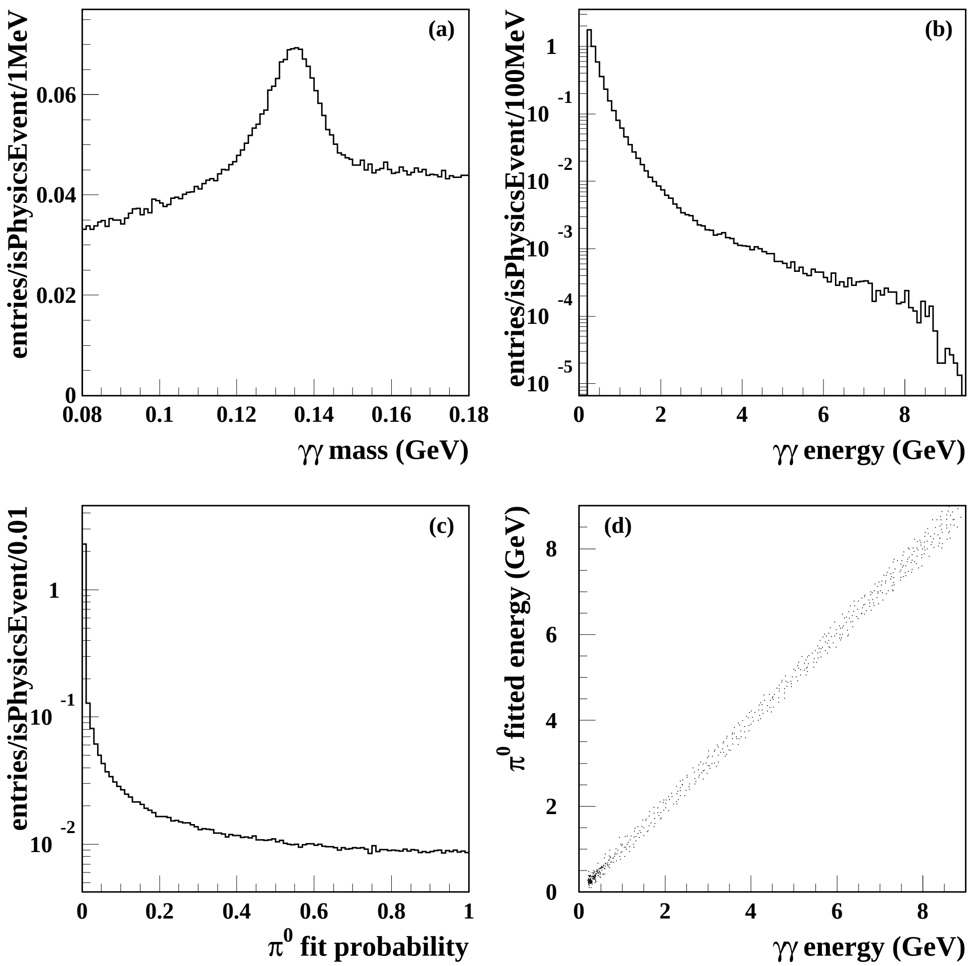

Figure 4.2: Distributions of (a) invariant mass, (b) total energy of pairs of neutral clusters, (c) mass-constrained fit χ^2 probability for a π^0 fit, and (d) a scatter plot of energies from a typical run (12917).

moment satisfying $LAT < 0.8$ and a minimum energy deposition of 30 MeV. The combination is required to have an invariant mass between 100 MeV/c^2 and 160 MeV/c^2 computed at the origin of the detector. Figure 4.2 shows the invariant mass and χ^2 distribution of the mass-constrained fit for a typical run.

The energy and momenta of π^0 candidates are recalculated with a constraint on the π^0 mass calculated at the beam spot position. This re-fitting technique improves the π^0 resolution from 3.0% to 2.5%. About 80% of all π^0s produced in generic Monte Carlo have both photons within the calorimeter's geometrical acceptance. The fraction of π^0s within the acceptance which pass the selection outlined above varies with π^0 energy; it is $65 - 70\%$ from 0.5-2.0 GeV and then falls linearly down to 25% at about 5 GeV due to a large fraction of overlapping showers. Details of the π^0 reconstruction can be found in reference [31].

4.3.2.2 Merged π^0

Merged π^0 selection proceeds by looking for local maxima in each EMC cluster and working from the assumption that local maxima correspond to the location of the decay photons. In particular the second moment (S_2) of the cluster energy distribution is used to define the estimated mass of the cluster,

$$m \equiv E \times \sqrt{S_2 - \bar{S}_2^{single}} \tag{4.1}$$

where E is the cluster energy and $\bar{S}_2^{single}$ is the average single photon cluster second moment. $\bar{S}_2^{single}$ is determined from simulation to be 0.0009945.

The cluster's mass estimate is then required to be within 20 MeV/c^2 of the nominal π^0 mass. This is a stronger restriction on the mass than for the composite π^0s because of the purity of the merged π^0 sample in inherently lower.

4.4 D Meson Reconstruction

4.4.1 D^0 Reconstruction

D^0 candidates are reconstructed in the modes $D^0 \to K^-\pi^+$, $D^0 \to K^-\pi^+\pi^-\pi^+$, $D^0 \to K^-\pi^+\pi^0$ and $D^0 \to K_S^0\pi^+\pi^-$. The branching fractions for these modes are given in Table 4.2. The following procedure is used to perform the reconstruction:

1. All kaons, pions, K_S^0 and π^0 with momentum $p > 100\,\mathrm{MeV}/c$ are vertexed according to the desired decay modes of the D^0. A mass cut is applied requiring consistecy of the vertexed object with the nominal D^0 meson mass ($1.865\,\mathrm{GeV/c^2}$). For $D^0 \to K^-\pi^+$, $D^0 \to K^-\pi^+\pi^-\pi^+$and $D^0 \to K_S^0\pi^+\pi^-$the mass must be within 90 MeV of the nominal mass. For the candidates reconstructed as $D^0 \to K^-\pi^+\pi^0$, a cut of 160 MeV is used due to the lower resolution of the π^0.

2. The charged kaon must satisfy the “KNNVeryLoose” kaon identification criterion (Section 2.11.1). Additionally, it must fail the “isEMicroTight” and “isMuMicroTight” lepton criteria. (Sections 2.11.3 and 2.11.2)

3. Charged pions must fail the “KNNVeryLoose”, “isEMicroTight” and “isMuMicroTight” criteria.

Table 4.2: Relevant branching fractions for the D^0 meson.

D^0 Modes	Branching Fraction
$K^-\pi^+$	3.83%
$K^-\pi^+\pi^-\pi^+$	7.49%
$K^-\pi^+\pi^0$	13.90%
$K^0_S\pi^+\pi^-(K^0_S \to \pi^+\pi^-)$	1.35%

4. The momentum of the D^0 candidate in the $\Upsilon(4S)$ reference frame must satisfy $0.5 < p^*_{D^0} < 2.5\,\mathrm{GeV/c}$. This requirement is based on the three-body dynamics of the process $B^- \to D^0\ell^-\overline{\nu}_\ell$, where the maximum momentum which the D^0 meson can have is half of the B^- meson mass and the minimum momentum is zero. Since D^0 mesons decaying at rest will produce low momentum charged particles with lower identification efficiency, the minimum momentum requirement on the D^0 is $0.5\,\mathrm{GeV/c}$.

The distribution of the reconstructed D^0 mass is shown in Fig. 4.4 from both data and the GEANT4 simulation.

4.4.2 D^{*+} Reconstruction

Although this search proceeds by first tagging a charged B meson as $B^- \to D^0\ell^-\overline{\nu}_\ell X$, the reconstruction of neutral B mesons as $\overline{B}^0 \to D^{*+}\ell^-\overline{\nu}_\ell X$ is also pursued. This is done for the purpose of an event veto. A misreconstructed $B^0\overline{B}^0$ event may have a correctly reconstructed D^0 meson which can additionally be paired with a low-momentum charged pion to form a D^{*-}. These mesons are therefore also reconstructed.

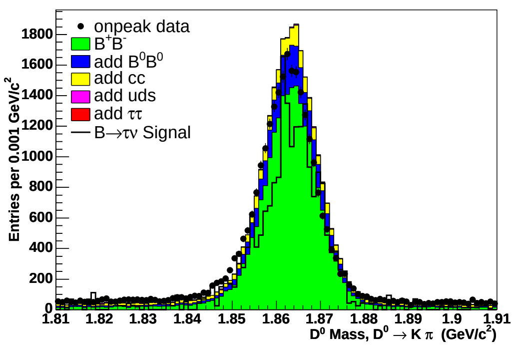

(a) $D^0 \to K^-\pi^+$

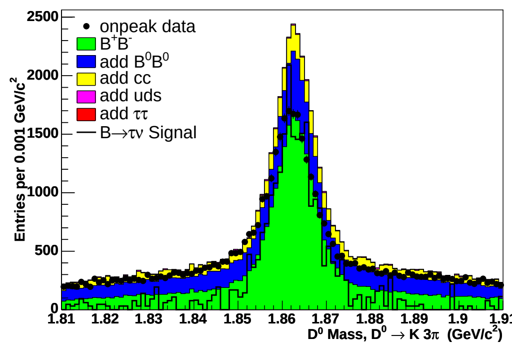

(b) $D^0 \to K^-\pi^+\pi^+\pi^-$

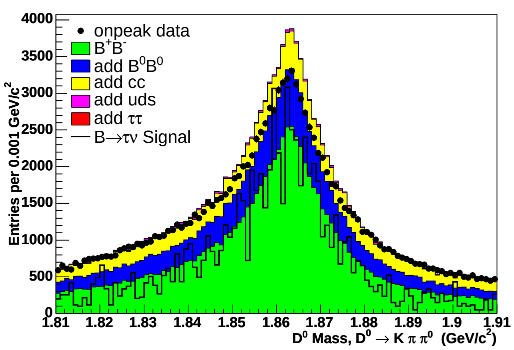

(c) $D^0 \to K^-\pi^+\pi^0$

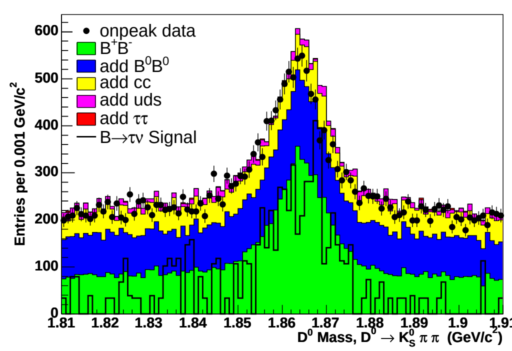

(d) $D^0 \to K^0_S\pi^+\pi^-$

Figure 4.3: The reconstructed D^0 mass for each of the four reconstructed modes. The comparison is performed between on-resonance data, generic MC and signal MC.

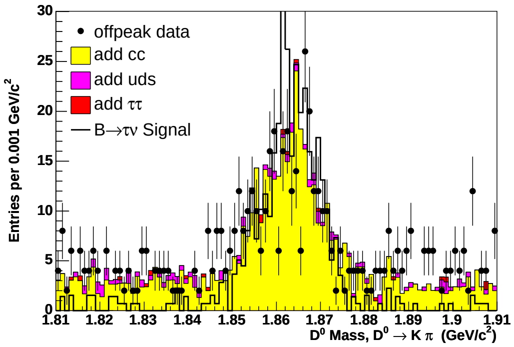

(a) $D^0 \to K^- \pi^+$

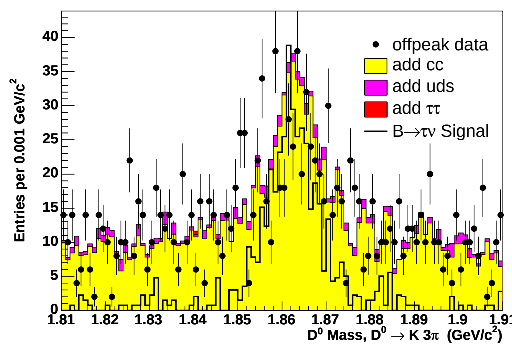

(b) $D^0 \to K^- \pi^+ \pi^+ \pi^-$

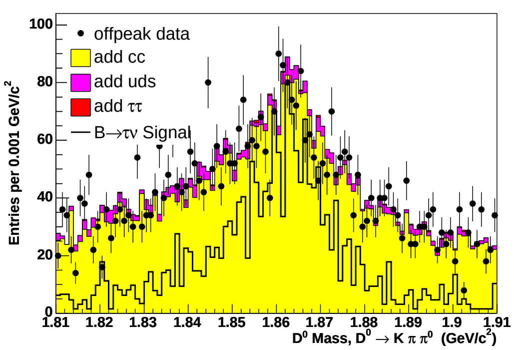

(c) $D^0 \to K^- \pi^+ \pi^0$

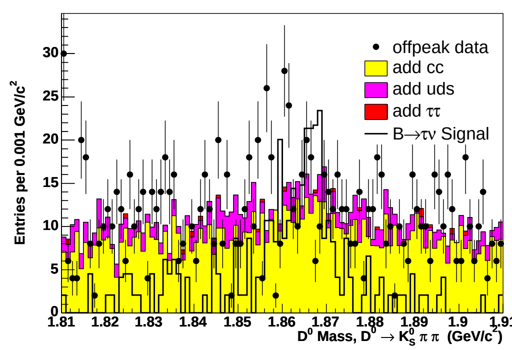

(d) $D^0 \to K^0_S \pi^+ \pi^-$

Figure 4.4: The reconstructed D^0 mass for each of the four reconstructed modes. The comparison is performed between off-resonance data, continuum MC and signal MC.

The D^{*-} candidates are reconstructed by pairing the D^0 candidates with charged pions and placing restrictions on the resulting object. These include:

1. Pairing the D^0 with a charged pion whose momentum is between $70\,\mathrm{MeV}/c$ and $450\,\mathrm{MeV}/c$.

2. The mass of the D^{*-} candidate is required to lie within $0.500\,\mathrm{GeV}/c^2$ of the nominal D^{*-} mass ($2.010\,\mathrm{GeV}/c^2$).

3. The difference between the D^{*-} candidate mass and the mass of the D^0 candidate used to construct it must satisfy $0.130 < \Delta M_{D^0,D^{*-}} < 0.170\,\mathrm{GeV}/c^2$. The nominal mass difference between these two particles is $0.145\,\mathrm{GeV}/c^2$.

4.5 $D\ell$ Candidate Reconstruction

After reconstructing D^0 and D^{*-} candidates, they are paired with leptons (muons and electrons) to form the highest-level reconstructed object, the $D\ell$ candidate. In order to be paired with a D^0 meson, the lepton must be identified as either an electron or muon and have a momentum in the center-of-mass frame satisfying $p^*_\ell > 1.0\,\mathrm{GeV}/c$. This momentum restriction is motivated by the particle identification performance discussed in Sections 2.11.2 and 2.11.3. In order to produce a high purity sample of $D\ell$ candidates it is necessary to start from a high purity sample of leptons. Such a sample can be obtained by requiring their momenta be above 1.0 GeV/c, as shown in Fig. 2.22 (electrons) and Fig. 2.21 (muons).

The D^0 meson and the lepton are required to meet at a common point near the origin of the detector. Further constraints are then placed on the $D\ell$ candidate to insure the quality of the candidate and to determine its consistency with having come from a B decay.

To determine the consistency of a $D\ell$ candidate with the hypothesis that it arose from B^- decay, the following assumption is made: the only particle missing from the tag B meson is the neutrino. With this assumption in mind, the energy of the tag B meson can be determined using the electron-positron beam information in the center-of-mass frame. If the four-vectors of the colliding electron and positron are P_e and P_p, respectively, then the energy and momentum magnitude of the B meson, E_B and $|\vec{p}_B|$ are defined as

$$E_B \equiv \frac{1}{2}\sqrt{(P_e + P_p)^2} \tag{4.2}$$

$$|\vec{p}_B| \equiv \sqrt{E_B^2 - m_B^2}. \tag{4.3}$$

If the only particle missing is a neutrino, then the angle between the $D\ell$ and the B^- meson (defined by $\cos\theta_{B,D\ell} \equiv \vec{p_B} \cdot \vec{p_{D\ell}}/|p_B||p_{D\ell}|$) can be written as

$$\cos\theta_{B,D\ell} \equiv \frac{2E_B E_{D\ell} - m_B^2 - m_{D\ell}^2}{2|\vec{p}_B||\vec{p}_{D\ell}|}. \tag{4.4}$$

In the case where the only missing particle is the neutrino, $\cos\theta_{B,D\ell}$ lies in the range $(-1, 1)$. However, due to feed down from higher-mass D^0 decay or detector effects (energy and momentum resolution) this variable can range outside $(-1, 1)$. For instance, for events with an extra photon or π^0 missing from higher-mass D meson decay this variable will tend toward values below -1.

A $D\ell$ candidate is required to satisfy $-2.5 < \cos\theta_{B,D\ell} < 1.1$. The asymmetry of the restriction is to accomodate the feed-down from higher-mass D meson decay (Fig. 4.6).

Finally, the D^0 mass for each decay mode is fitted to determine the mean and width (σ) of the mass distribution (Fig. 4.7 and Fig. 4.8). This is done separately for data and simulation, to account for differences between the two. The fit is performed using a Gaussian to fit the central peak and a Chebychev polynomial to fit the remaining distribution of events. The goal of this fit is only to define a mean and width for the peak, not to describe the physics of the shape of the distribution. Once the mean and width of the Gaussian are determined, the mass of a given candidate is required to lie within 3σ of the fitted mean for its decay mode.

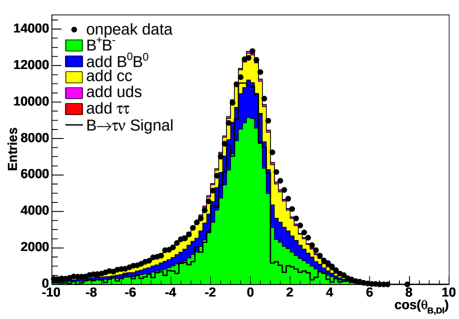

(a) On-resonance data is compared with generic MC and signal MC

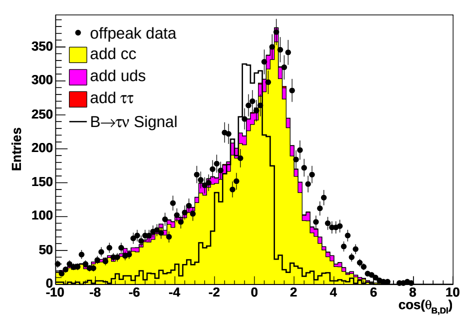

(b) Off-resonance data is compare with continuum MC and signal MC

Figure 4.5: The angle between the best $D\ell$ candidate and the B^- meson, as determined from the reconstructed $D\ell$ momentum and the beam parameters (used to represent the parent B^- meson), assuming in the calculation that only a neutrino is missing from the B^- decay.

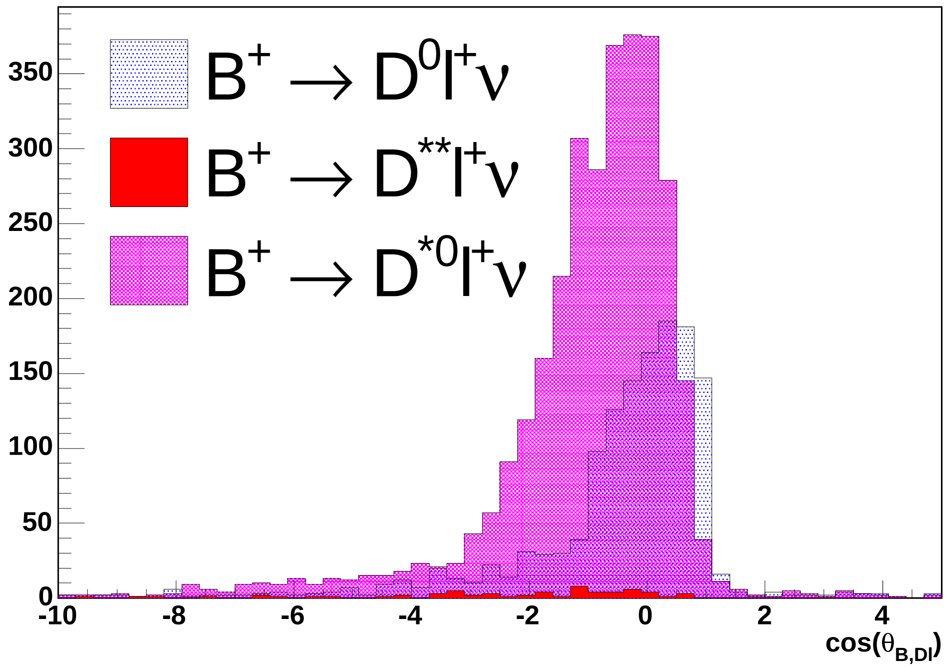

Figure 4.6: The distribution of $\cos\theta_{B,D\ell}$ for events with a true $B \to D^0\ell\nu X$ and $B \to D^{*0}\ell\nu X$, illustrating the asymmetric nature of $\cos\theta_{B,D\ell}$ for events with higher-mass D decay.

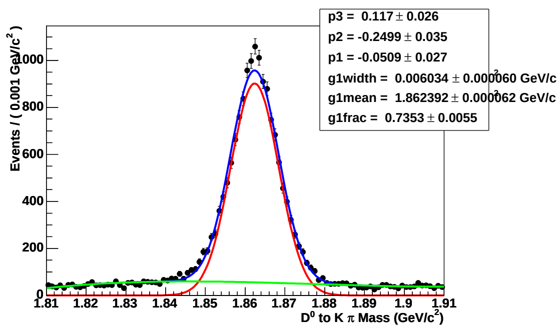

(a)

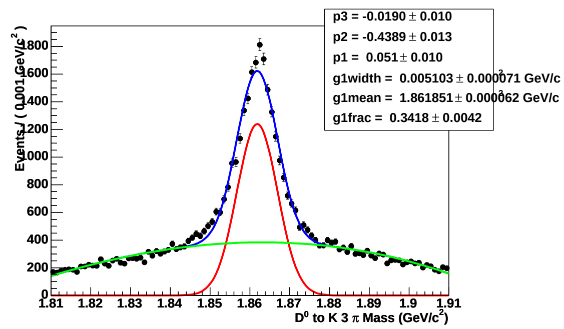

(b)

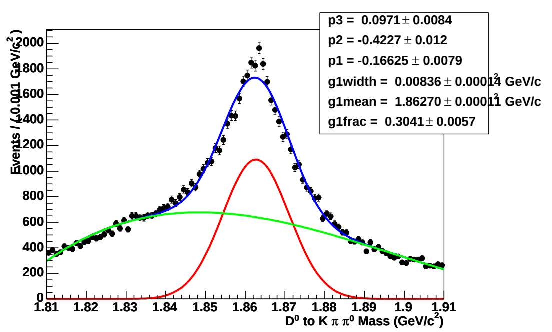

(c)

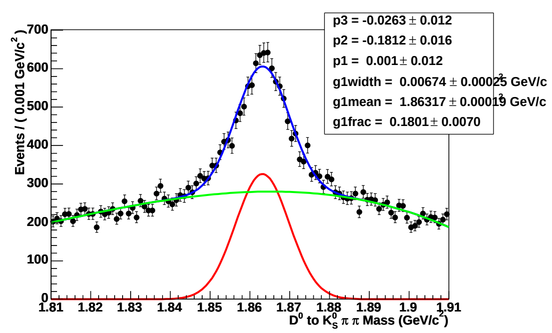

(d)

Figure 4.7: The fits to the D^0 mass peaks in 2000 onpeak data. The fit uses a Chebychev polynomial and a Gaussian.While the fits are not perfect, they provide an adequate definition of the width for use in the analysis.

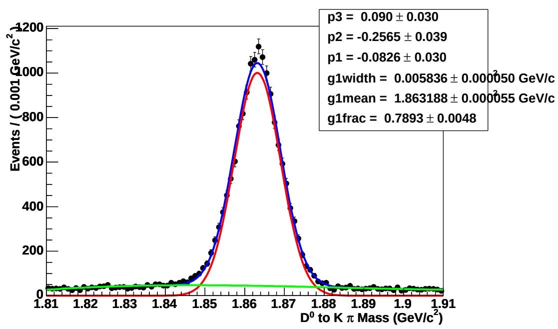

(a)

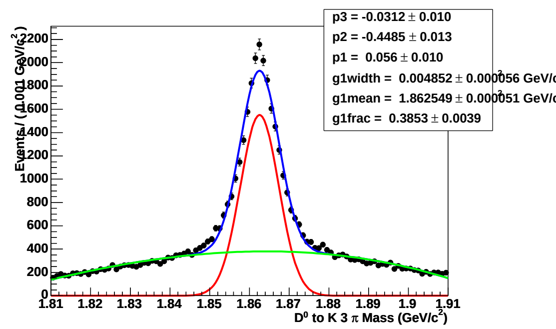

(b)

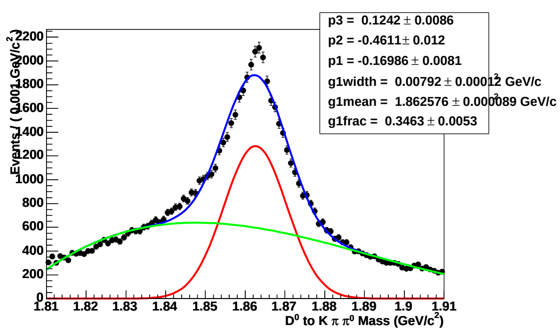

(c)

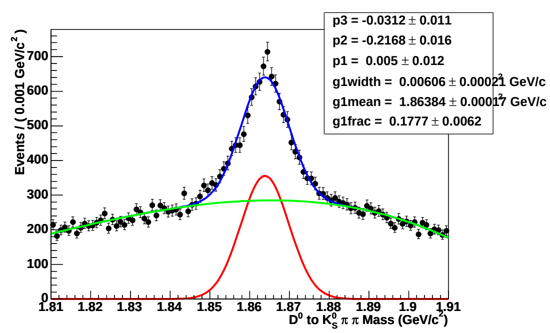

(d)

Figure 4.8: The fits to the D^0 mass peaks using Monte Carlo generated using year 2000 conditions. The fit uses a Chebychev polynomial and a Gaussian. While the fits are not perfect, they provide an adequate definition of the width for use in the analysis.

4.6 The Treatment of Multiple $D\ell$ Candidates

After forming pairs of D^0 mesons and leptons, there are often many candidates in an event. In fact, on average an event will contain 10 $D\ell$ candidates, illustrated in Fig. 4.9. To choose a best candidate, a probability density function (PDF) is defined. The PDFs are made for each of the four D^0 decay modes using the reconstructed D^0 mass for events with a true $D\ell$ candidate. The distribution of the mass is illustrated in Fig. 4.10. These distributions are normalized and converted into probability density distributions. The distributions are then fitted using Gaussians and a polynomial to obtain a smooth probability density function (Fig. 4.11).

The best $D\ell$ candidate is chosen to be the one which has a maximal value returned from its mass PDF. If the best $D\ell$ candidate is a $D^{*-}\ell$, then the event is assumed to have been a mis-reconstructed $B^0\overline{B}^0$ event and it is vetoed. The $D^0\ell$ candidate is then used to define the tagged semi-leptonic B-meson; the rest of the particles in the event not associated with the $D\ell$ are referred to as the *recoil* of the semi-leptonic B-meson and are associated with the signal B meson.

4.7 Global Event Quality Restrictions

Only a subset of the total available data is of interest to the present work. At a very early stage of this analysis, after building lists of D^0 mesons and leptons, loose, global restrictions are placed on events to reject those which are clearly not

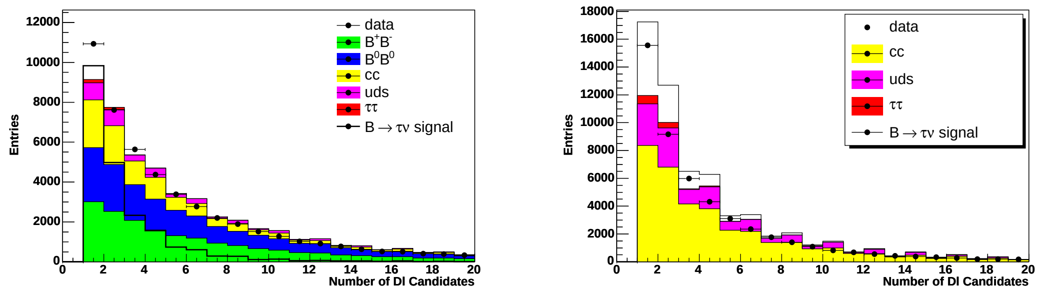

(a) Onpeak data is compared with generic Monte Carlo and signal simulation.

(b) Offpeak data is compared with continuum Monte Carlo and signal simulation.

Figure 4.9: The number of $D\ell$ candidates in each event. $1.1\,\mathrm{fb}^{-1}$ of onpeak data from 2001 and all 2001 offpeak data are used in the comparison.

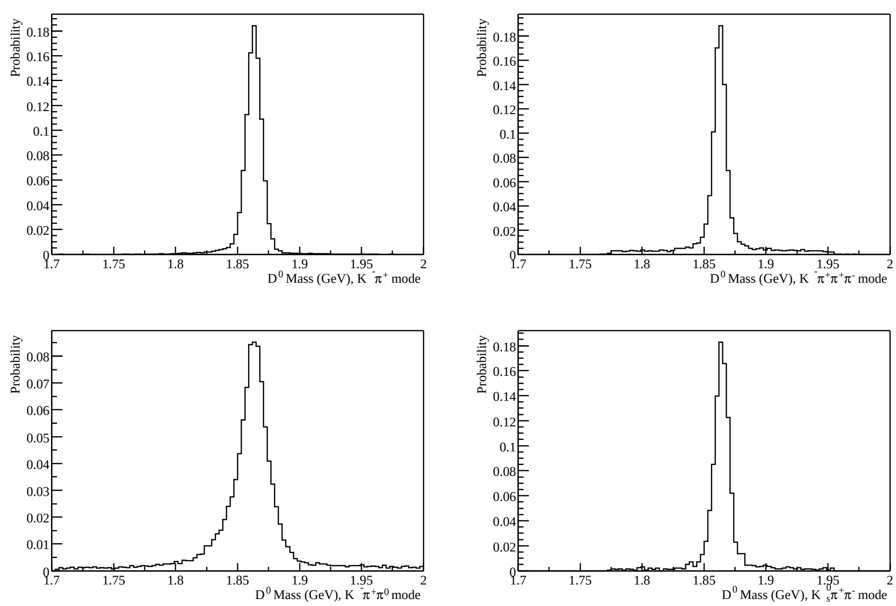

Figure 4.10: The reconstructed D^0 mass distribution for $D\ell$ candidates which have been matched to true $B^- \to D^0\ell^-(\nu X)$ decays. This distribution is shown for each of the reconstructed D^0 modes.

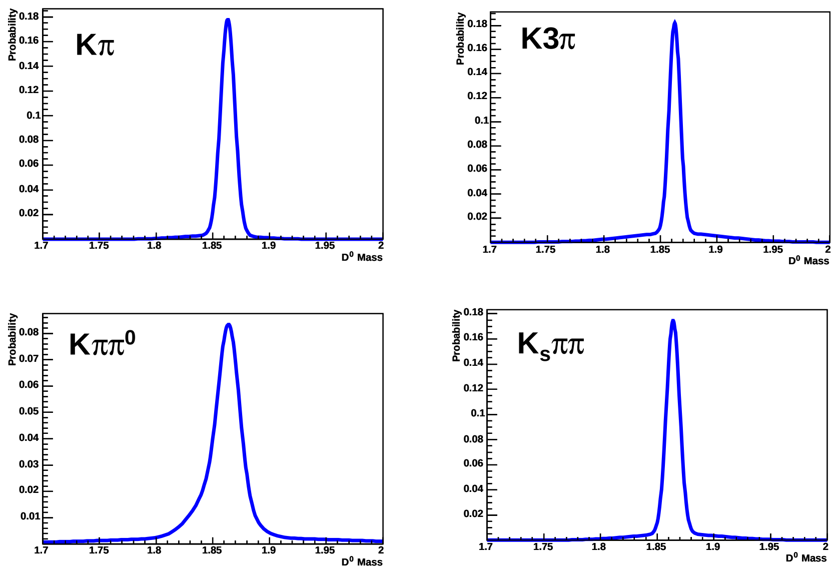

Figure 4.11: The fits to the reconstructed D^0 mass distribution for $D\ell$ candidates which have been matched to true $B^- \to D^0\ell^-(\nu X)$ decays. This distribution is shown for each of the reconstructed D^0 modes.

of interest to this search.

In particular, the event charge is required to balance (zero net charge). Such a balance is expected in correctly reconstructed B^+ B^- events. A restriction is also placed on the second Fox-Wolfram moment (R_2) [32] and the missing mass in the events. Events with B mesons tend to lead to a more uniform distribution of charged tracks and neutrals. This quality is reflected in lower values of R_2. In addition, events with many missing particles (in the form of neutrinos) will tend to have large values for the missing mass. Additionally, potential backgrounds from $e^+e^- \to f\bar{f}$ (where f is any fermion except a bottom quark) are largely removed even by a loose restriction on R_2, since they tend to be more collimated than $e^+e^- \to B\overline{B}$ events (Fig. 4.12).

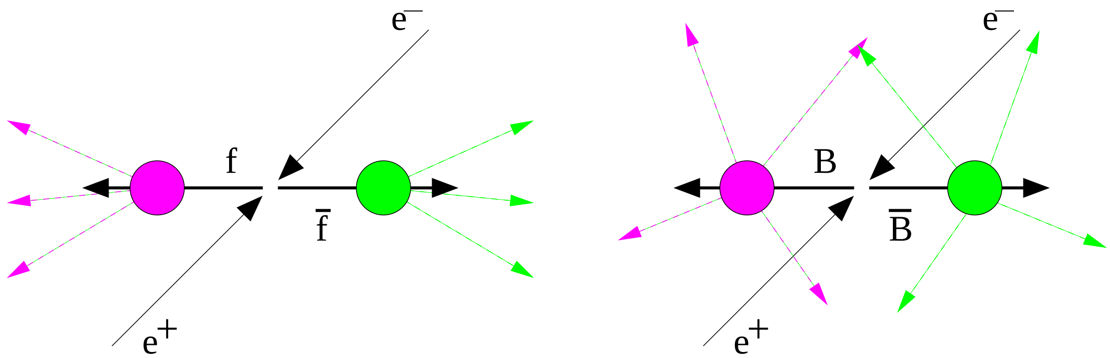

Figure 4.12: An illustration of the differences in particle distributions from $e^+e^- \to f\bar{f}$ and $e^+e^- \to B\bar{B}$ in the center-of-mass frame.

The degree of restriction on R_2 and missing mass are determined by the presence of a class of events with four fermions in the final state ($e^+e^- \to f^+f^-f^+f^-$). These events are not simulated in the *BABAR* Monte Carlo but are present in data. In particular, they are evident in off-resonance data. The evidence for the presence of these decays is available in Appendix A. The result of studying these events is to restrict R_2 and missing mass as follows: $R_2 < 0.9$ and $M_{missing} > 1.0\,\mathrm{GeV/c^2}$.

In addition, a restriction is placed on the number of particles recoiling against any given $D\ell$ candidate (denoted N^{recoil}_{track}). The charged particle multiplicity of τ final states does not exceed three particles for modes with significant branching fractions. Therefore, a restriction is placed on events requiring that there be at least one $D\ell$ candidate with $N^{recoil}_{track} \leq 3$. An exception to this requirement are events with two, non-overlapping $D\ell$ candidates. These events will be used in Section 4.9 to study the tag B efficiency in data and Monte Carlo simulations.

4.8 B Reconstruction Efficiency

The selection criteria outlined in the previous sections and their cumulative and marginal efficiencies are given in Table 4.3. The total efficiency of the tagging algorithm on signal simulation (where one B meson decays generically and the other always as $B^+ \to \tau^+ \nu_\tau$) is $(0.446 \pm 0.011) \times 10^{-2}$, where the error is purely statistical. Therefore, in the 88.9×10^6 B^+ mesons in the data used for this analysis $\sim 400,000$ semi-leptonic B-mesons are expected to be reconstructed for use as a basis for the rest of the analysis.

The order in which the selections are presented in this chapter is chosen for conceptual clarity. In the analysis itself, the selection criteria are applied in a slightly different order, as follows:

1. Events are required to contain at least one vertexed D^0 and lepton pair ("$B^- \to D^0 \ell^- \overline{\nu}_\ell X$ Preselection"),
2. there must at least one vertexed D^0 and lepton pair with no more than three charged tracks recoiling against them ("N_{trk} Recoil ≤ 3"),
3. the event charge must be zero,
4. the event must have lage missing mass and lower R_2 ("Four Fermion Veto"),
5. the best $D\ell$ candidate must be a $D^0\ell$ candidate,
6. the $D\ell$ candidate must pass the $\cos\theta_{B,D\ell}$ restriction (Sec. 4.5),
7. and the mass of the D^0 must be within 3σ of the fitted mean.

This is the order of the selection criteria presented in Tables 4.3, 4.4, and 4.5.

Table 4.3: The marginal and cumulative efficiencies of the semi-leptonic B-meson selection in signal simulation. The signal simulation has been normalized to the data luminosity assuming a branching fraction of 1×10^{-4}.

Selection	Number Passing (Cumulative Eff.) (Marginal Eff.)
Generator Level	8887.042
$B^- \to D^0 \ell^- \overline{\nu}_\ell X$ Preselection	427.942 (4.8153%)(4.82%)
N_{trk} Recoil ≤ 3	239.819 (2.6985%)(56.04%)
$\sum_i q_i = 0$	145.475 (1.6369%)(60.66%)
Four Fermion Veto	144.094 (1.6214%)(99.05%)
$D^0 \ell \nu$ Tag	83.050 ± 1.358 (0.9345%)(97.60%)
$-2.5 < cos\theta_{B,D\ell} < 1.1$	57.159 ± 1.130 (0.6432%)(68.83%)
3σ D^0 mass window	39.595 ± 0.937 (0.4455%)(69.27%)

Table 4.4: The effect of the semi-leptonic B-meson selection criteria as applied to generic Monte Carlo and onpeak Data. The B^+B^- events do not contain signal events.

Selection	Number Passing (Cumulative Eff.) (Marginal Eff.)						
	$B^+\ B^-$	$B^0\ \overline{B}^0$	$c\overline{c}$	uds	$\tau^+\ \tau^-$	Total MC	Onpeak Data
Generator Level	44435168.000	44435154.000	106433399.000	171112594.000	76959665.000	443375980.000	1108551025.000
$B^- \to D^0\ell^-\overline{\nu}_\ell X$ Preselection	5406634.400 (12.1675%)(12.17%)	5535024.982 (12.4564%)(12.46%)	3756112.862 (3.5291%)(3.53%)	2183582.874 (1.2761%)(1.28%)	46027.106 (0.0598%)(0.06%)	16927382.224 (3.8178%)(3.82%)	18384400.000 (1.6584%)(1.66%)
N_{trk} Recoil ≤ 3	1106724.094 (2.4906%)(20.47%)	1008776.239 (2.2702%)(18.23%)	828526.764 (0.7784%)(22.06%)	448663.022 (0.2622%)(20.55%)	30102.142 (0.0391%)(65.40%)	3422792.260 (0.7720%)(20.22%)	3428887.000 (0.3093%)(18.65%)
$\sum_i q_i = 0$	580385.316 (1.3061%)(52.44%)	424247.498 (0.9548%)(42.06%)	465424.543 (0.4373%)(56.17%)	253502.765 (0.1481%)(56.50%)	19857.761 (0.0258%)(65.97%)	1743417.882 (0.3932%)(50.94%)	1762538.000 (0.1590%)(51.40%)
Four Fermion Veto	513846.439 (1.1564%)(88.54%)	389599.165 (0.8768%)(91.83%)	335107.628 (0.3149%)(72.00%)	122536.204 (0.0716%)(48.34%)	17367.677 (0.0226%)(87.46%)	1378457.112 (0.3109%)(79.07%)	1303379.000 (0.1176%)(73.95%)
$D^0\ell\nu$ Tag	298578.339 (0.6719%)(97.37%)	176822.648 (0.3979%)(85.48%)	154043.590 (0.1447%)(96.46%)	15474.768 (0.0090%)(98.19%)	1071.530 (0.0014%)(98.01%)	645990.874 (0.1457%)(93.61%)	605074.000 (0.0546%)(94.50%)
$-2.5 < \cos\theta_{B,D\ell} < 1.1$	184857.356 (0.4160%)(61.91%)	91614.220 (0.2062%)(51.81%)	69132.093 (0.0650%)(44.88%)	6120.204 (0.0036%)(39.55%)	394.137 (0.0005%)(36.78%)	352118.010 (0.0794%)(54.51%)	328376.000 (0.0296%)(54.27%)
3σ D^0 mass window	110262.606 (0.2481%)(59.65%)	38743.255 (0.0872%)(42.29%)	23839.231 (0.0224%)(34.48%)	1698.793 (0.0010%)(27.76%)	79.901 (0.0001%)(20.27%)	174623.786 (0.0394%)(49.59%)	158539.000 (0.0143%)(48.28%)

Table 4.5: The effect of the selection criteria in continuum Monte Carlo and offpeak data. The offpeak data has been scaled to the onpeak data luminosity.

Selection	Number Passing (Cumulative Eff.) (Marginal Eff.)				
	$c\overline{c}$	uds	$\tau^+ \tau^-$	Total MC	Offpeak Data
Generator Level	106433399.000	171112594.000	76959665.000	354505658.000	117990000.000
$B^- \to D^0 \ell^- \overline{\nu}_\ell X$ Preselection	3756112.862 (3.5291%)(3.53%)	2183582.874 (1.2761%)(1.28%)	46027.106 (0.0598%)(0.06%)	5985722.842 (1.6885%)(1.69%)	7303184.000 (6.1897%)(6.19%)
N_{trk} Recoil ≤ 3	828526.764 (0.7784%)(22.06%)	448663.022 (0.2622%)(20.55%)	30102.142 (0.0391%)(65.40%)	1307291.927 (0.3688%)(21.84%)	1526040.000 (1.2934%)(20.90%)
$\sum_i q_i = 0$	465424.543 (0.4373%)(56.17%)	253502.765 (0.1481%)(56.50%)	19857.761 (0.0258%)(65.97%)	738785.069 (0.2084%)(56.51%)	835862.000 (0.7084%)(54.77%)
Four Fermion Veto	335107.628 (0.3149%)(72.00%)	122536.204 (0.0716%)(48.34%)	17367.677 (0.0226%)(87.46%)	475011.509 (0.1340%)(64.30%)	481270.000 (0.4079%)(57.58%)
$D^0 \ell \nu$ Tag	154043.590 (0.1447%)(96.46%)	15474.768 (0.0090%)(98.19%)	1071.530 (0.0014%)(98.01%)	170589.888 (0.0481%)(96.63%)	203643.000 (0.1726%)(96.83%)
$-2.5 < cos\theta_{B,D\ell} < 1.1$	69132.093 (0.0650%)(44.88%)	6120.204 (0.0036%)(39.55%)	394.137 (0.0005%)(36.78%)	75646.433 (0.0213%)(44.34%)	78982.000 (0.0669%)(38.78%)
3σ D^0 mass window	23839.231 (0.0224%)(34.48%)	1698.793 (0.0010%)(27.76%)	79.901 (0.0001%)(20.27%)	25617.925 (0.0072%)(33.87%)	26365.000 (0.0223%)(33.38%)

4.9 The Study of Semi-Leptonic B Reconstruction Efficiency using Double-Tagged Events

As suggested by several of the figures in this chapter, there is no guarantee that the reconstruction efficiency of $D\ell$ candidates is identical in data and simulation. Therefore, a technique called *double-tagging* is pursued to evaluate the effciency difference between data and simulation for the semi-leptonic B meson reconstruction.

A *double-tagged* event is one where both B^+ mesons are reconstructed as

$$B^+ \to \overline{D}^0 \ell^+ \nu X \;+\; B^- \to D^0 \ell^- \overline{\nu} X. \tag{4.5}$$

The reconstructed $D\ell$ candidates must not share any common daughter particles. Given a sample of N B^+B^- events, the number of double-tags (N_2) is given by

$$N_2 = \varepsilon^2 N, \tag{4.6}$$

where ε is the probability of reconstructing a B meson as $B^- \to D^0 \ell^- \overline{\nu}_\ell X$. Double-tags are defined as a pair of non-overlapping $D\ell$ candidates with no extra charged tracks in the event. In addition, the effects of pre-selections are removed by relaxing the four-fermion veto and the charge balance requirements (see Section 4.7).

The number of double-tags in the data set, as determined from the data and predicted from generic Monte Carlo simulation, are

$$N_2^{data} = 1047.00 \pm 32.36 \quad (4.7)$$

$$N_2^{MC} = 1241.94 \pm 21.63 \quad (4.8)$$

If an assumption is made that all double-tags come from charged B mesons, then the normalization N is defined solely by the number of B^+B^- mesons available in *BABAR* ($N = 44.45 \times 10^6$). The efficiency in data and Monte Carlo is calculated by solving equation 4.6 for ε. The ratio of the efficiency in data and simulation provides a correction to the tag B reconstruction efficiency in Monte Carlo:

$$\frac{\varepsilon_{data}}{\varepsilon_{MC}} = 0.918 \pm 0.018 \quad (4.9)$$

One problem with the above method is that the sample is assumed to derive purely from B^+B^- events. However, a survey of the Monte Carlo simulation reveals that nearly 10% of the double-tags come from $B^0\overline{B}^0$ events. In this situation, the normalization factor is therefore not clearly defined. Another assumption in Eqn. 4.6 is that the efficiency of reconstructing one B meson, then a second, is the same as simply squaring the single B meson reconstruction efficiency. To avoid these assumptions, double-tagged *and* single-tagged events are used to cancel some assumptions. A single-tagged event is defined as an event with one and only one B meson reconstructed as $B^- \to D^0\ell^-\overline{\nu}_\ell X$. The number of single-tagged events in a sample of N B^+B^- events is

$$N_1 = 2\varepsilon_A(1 - \varepsilon_B)N\alpha_1, \quad (4.10)$$

where ε_A is the probability of reconstructing one B meson as $B^- \to D^0\ell^-\overline{\nu}_\ell X$; ε_B is the probability of reconstructing a second B meson as $B^- \to D^0\ell^-\overline{\nu}_\ell X$ having already reconstructed the first in the same way; and α_1 is the effect of pre-selections on these events. The double-tags are similarly redefined to take into account the possible differences in B meson reconstruction and pre-selection effects,

$$N_2 = \varepsilon_A \varepsilon_B N \alpha_2. \tag{4.11}$$

The ratio of single-to-double tags is then taken to cancel out many of the unknowns in the above definitions of single and double tags. The only assumption made here is that $\alpha_1 = \alpha_2$ (that is, that preselections affect single and double tags in the same way). Since the only pre-selections that remain are the requirement that an event contain at least one high-momentum lepton and at least one D^0 meson, the effect is expected to be the same for events with either one or two real $B^- \to D^0\ell^-\overline{\nu}_\ell X$ decays. Having made this assumption, the ratio is then

$$\frac{N_1}{N_2} = \frac{2(1-\varepsilon_B)}{\varepsilon_B}. \tag{4.12}$$

The number of double and single tags in data and Monte Carlo simulation is given in Table 4.6. Using these results in the above equation and solving for the efficiencies in data and simulation, the correction factor which should be applied to the tag B efficiency in Monte Carlo is

$$\frac{\varepsilon_{data}}{\varepsilon_{MC}} = 0.882 \pm 0.031. \tag{4.13}$$

This result is in good agreement with the method outlined at the beginning of

Table 4.6: The yields of single and double tags in data and MC. Also given are the efficiencies, as derived from formula 4.12.

	MC	Data
N_1	371404.30 ± 439.73	355201.00 ± 595.99
N_2	1241.94 ± 21.63	1047.00 ± 32.36
ε_B	0.00664 ± 0.00012	0.00586 ± 0.00018

this section. This agreement suggests that the deviation from the assumption of a normalization dominated by B^+ B^- events is small. Despite this agreement, the single-tag/double-tag method is used because of its inherent independence from the absolute normalization.

Chapter 5

The Selection of $B^+ \to \tau^+\nu_\tau$

Once the semi-leptonic tag B has been identified, the recoiling particles are required to be consistent with the decay $B^+ \to \tau^+\nu_\tau$. The *recoil* refers to all charged tracks and neutral clusters which are not associated with the $B^- \to D^0\ell^-\overline{\nu}_\ell X$ decay. This search is restricted to the one-prong leptonic decay modes of the τ lepton, $\tau^+ \to e^+\nu_\tau\nu_e$ and $\tau^+ \to \mu^+\nu_\tau\nu_\mu$. The use of hadronic final states of the τ lepton are possible but introduces significantly more background processes into the analysis (owing to the large number of pions expected *a priori* in each event).

One-prong leptonic tau decay from $B^+ \to \tau^+\nu_\tau$ has a fairly unique signature, including

1. One charged track which originates near the interaction point, identified as either an electron or a muon,

2. a signal lepton momentum spectrum which should be softer than that of a lepton from direct B decay, and

3. very little neutral energy (neutral clusters) associated with the recoil, owing

to the lack of neutrals in the single-prong τ decay.

The following sections outline the selection criteria for $B^+ \to \tau^+\nu_\tau$, using these principles as guidance. The charged and neutral objects in the recoil are henceforth referred to as belonging to the *signal side*.

5.1 Signal Side Topology

The one-prong decay of the tau lepton provides a restriction on number of charged track remaining after reconstructing the tag B. The number of signal-side tracks in data, background and signal simulation is shown in Fig. 5.1. Events are required to contain only one charged particle in the recoil.

To select one-prong leptonic τ decay modes the track must be identified either as a muon or an electron. To exclude possible contamination from another rare decay, $B^+ \to K^+\nu\overline{\nu}$, or from misreconstrusted decays of the B meson to D^0 mesons (and subsequent kaons), the track must additionally fail kaon identification.

This single track must also have originated from the region near the interaction point. The distance of closest approach to the interaction point in the $x - y$ plane (D_{xy}) (Fig. 5.2) is required to satisfy $D_{xy} < 0.1\,\mathrm{cm}$. This requirement is only applied to tracks whose momentum in the laboratory frame is $> 0.6\,\mathrm{GeV/c}$. This momentum-dependent requirement is made because for charged tracks with momentum less than $0.6\,\mathrm{GeV/c}$ the tracking algorithms are less efficient.

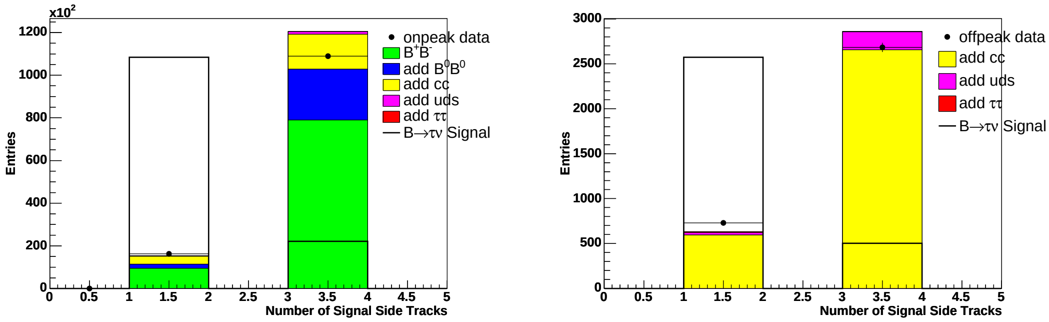

(a) On-resonance data, generic MC and signal MC.

(b) Off-resonance data, continuum MC and signal MC.

Figure 5.1: The number of charged particles in the recoil of the $D\ell$ candidate.

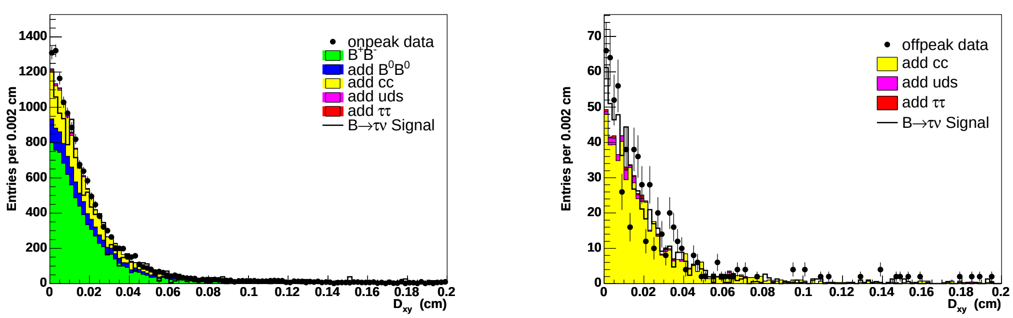

(a) On-resonance data, generic MC and signal MC.

(b) Off-resonance data, continuum MC and signal MC.

Figure 5.2: The distance of closest approach to the beam spot in the $x-y$ plane (D_{xy}).

5.2 Continuum Rejection

There are background processes which can mimic the signatures of the events so far considered. Apart from background from B decays, there can be contributions from continuum events ($e^+e^- \to u\overline{u}$, $d\overline{d}$, $s\overline{s}$, $c\overline{c}$, $\tau^+\tau^-$). The most significant potential contamination comes from two sources in the continuum events: $c\overline{c}$ events with correctly reconstructed D^0 mesons randomly paired with leptons; and $\tau^-\tau^+$ events with a fake $B^- \to D^0\ell^-\overline{\nu}_\ell X$ and real τ decay on the signal side.

There are topological differences between B decay and the decay of quark or lepton pairs produced by the collider. The main difference is the "jettiness" or collimation of tracks and neutrals in the events. Decays of pairs of B mesons tend to be more spherically distributed in the center-of-mass frame, while decays of $q\overline{q}$ or $\tau^+\tau^-$ tend to be more collimated along an axis (see Fig. 4.12).

A quantity called *thrust* is used to reject collimated events. The thrust vector, $\vec{t}$, is defined as the vector which maximizes the thrust magnitude, T,

$$T \equiv \frac{\sum_{i=1}^{N_{tracks}} |\vec{p}_i \cdot \vec{t}|}{\sum_{i=1}^{N_{tracks}} |\vec{p}_i|} \tag{5.1}$$

where p_i is the momentum of particle i in the $\Upsilon(4S)$ rest frame [33]. The $D\ell$ thrust is calculated using all particles associated with the reconstructed $D\ell$ candidate. The quantity $|\cos\theta_{\vec{p}_{signal},\vec{t}}|$ tends to peak at one for continuum (Fig. 5.3); that is, the signal-side track tends to be aligned parallel (or anti-parallel) to the direction of the $D\ell$ thrust.

While the thrust angle can be used in general to reject continuum events, $\tau^+\tau^-$ events have an additional property which allows them to be rejected more efficiently. For a given event, the invariant mass of all groups of three tracks is calculated and the minimum invariant mass that results from this exercise is determined. For events which are the result of $\tau^+\tau^-$ decay, the quantity (M_3^{min}) tends to peak below the τ mass. This quantity is illustrated in Fig. 5.4 for data, background and signal simulation.

Restrictions on $|\cos\theta_{\vec{p},\vec{T}}|$ and M_3^{min} are combined into a single requirement to reject continuum events. An event must either satisfy $|\cos\theta_{\vec{p},\vec{T}}| < 0.9$ or $M_3^{min} > 1.5$ to be considered a signal event. In particular, this two-dimensional cut helps to reduce contamination from τ^+ τ^- events (Fig. 5.5).

5.3 Signal Track Momentum

Single charged particles resulting from true τ decays have a momentum phase space restricted by spin and the presence of neutrinos. This restriction softens the overall momentum spectrum of the leptons, allowing their distinction from primary leptons in semi-leptonic B-decays. The raw momentum distribution after requiring one signal-side track is shown in Fig. 5.6, and is divided according to whether the track is identified as an electron or muon in Fig. 5.7 and Fig. 5.8, respectively.

The spectrum of the τ's lepton daughters is typically soft compared to that of a primary lepton from B decay. Consequently, this variable can be used to separate

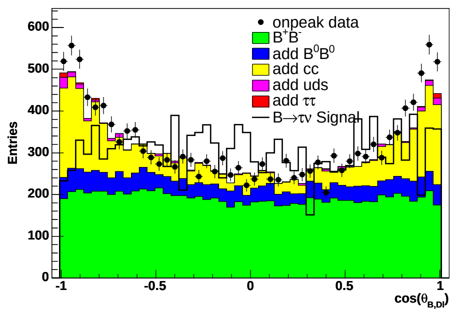

(a) On-resonance data, generic MC and signal MC.

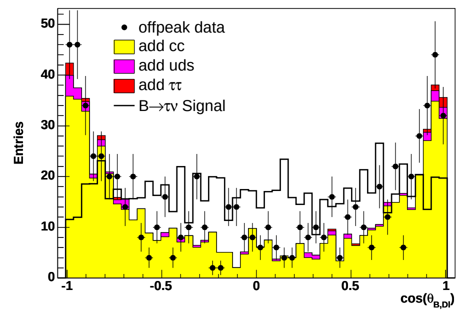

(b) Off-resonance data, continuum MC and signal MC.

Figure 5.3: The cosine of the angle between the signal track and the thrust of the $D\ell$ candidate.

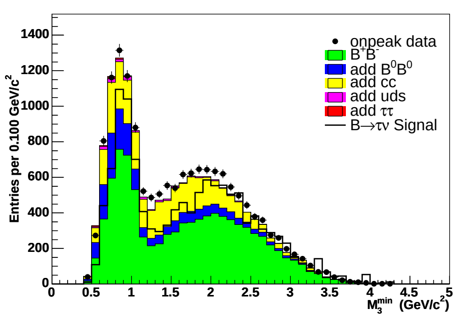

(a) On-resonance data, generic MC and signal MC.

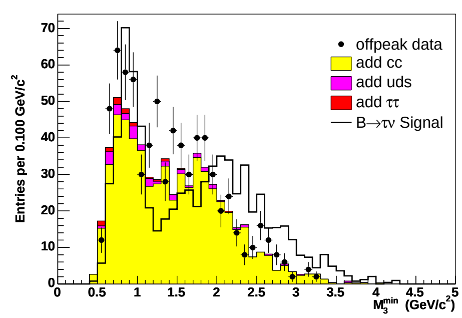

(b) Off-resonance data, continuum MC and signal MC.

Figure 5.4: The minimum invariant mass that can be constructed from any triplet of tracks in the event.

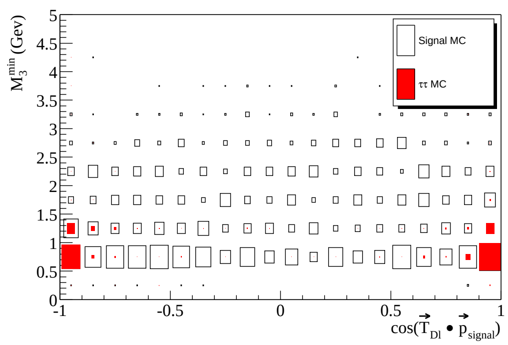

Figure 5.5: A comparison of M_3^{min} vs. $|\cos\theta_{\vec{p},\vec{T}}|$ for τ^+ τ^- events (red,solid) and signal events (black,open).

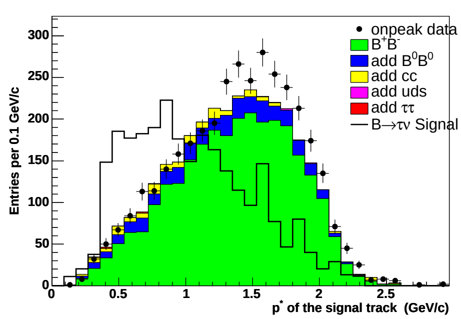

(a) Onpeak Data, Background MC and signal MC.

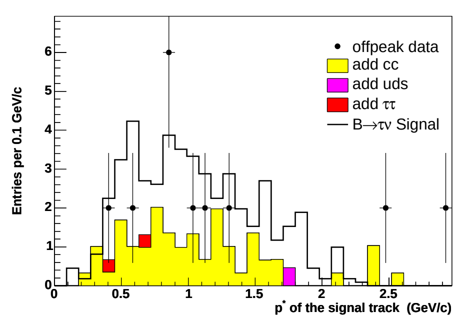

(b) Offpeak Data, Continuum MC and signal MC.

Figure 5.6: p^* of the signal-side track, compared between data and MC.

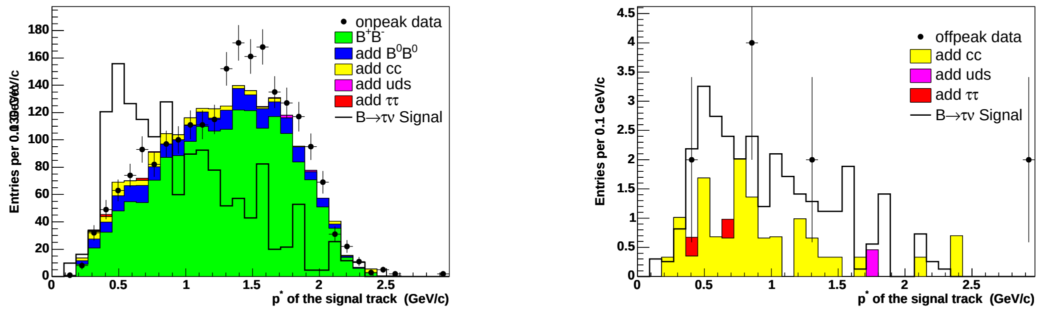

(a) Onpeak Data, Generic MC and signal MC.

(b) Offpeak Data, Continuum MC and signal MC.

Figure 5.7: p^* of the signal-side track for tracks identified as electrons, compared between data and MC.

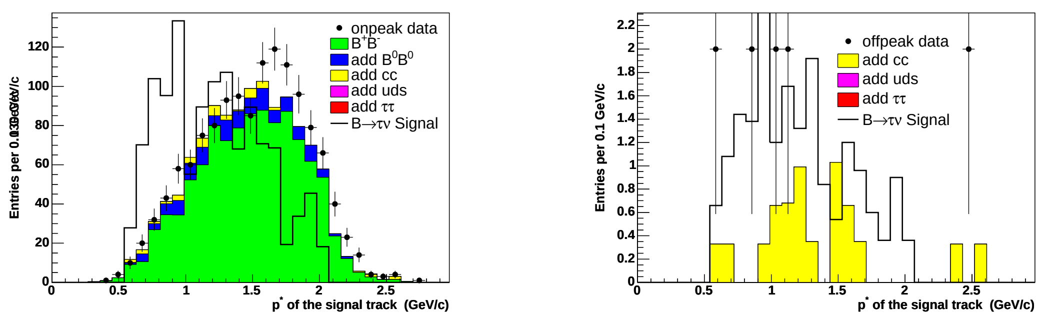

(a) Onpeak Data, Generic MC and signal MC.

(b) Offpeak Data, Continuum MC and signal MC.

Figure 5.8: p^* of the signal-side track for tracks identified as muons, compared between data and MC.

signal from background. However, because the primary background comes from $B \to D\ell\nu$ events where the D meson is "invisible" (decays to K_L^0 or its tracks are not reconstructed) the analysis tends to select soft primary leptons as daughters of the τ. This variable has less power than the neutral energy (discussed in Section 5.4), which tends to contain neutral energy from the "unseen" D meson.

BABAR analyses which attempt to select semi-leptonic B decays ($u\ell\nu$ and $c\ell\nu$-based analyses) (*c.f.* reference [34]) typically select their leptons by requiring that $p^* > 1.1 - 1.8\,\mathrm{GeV/c}$. In figures 5.6-5.8, placing at cut at $1.2\,\mathrm{GeV/c}$ tends to preserve most of the signal ($\sim 70\%$) while removing $\sim 60\%$ of the background, which is dominated by $c\ell\nu$ decays with a small component from $u\ell\nu$.

5.4 Extra Neutral Energy

After applying the restrictions outlined in the previous sections, a final restriction is made using the neutral energy remaining in the calorimeter which is not associated with the $D\ell$ candidate (henceforth denoted E_{extra}). Events from true $B^+ \to \tau^+\nu_\tau$ decay possess little or no extra neutral energy, and such energy is usually the result of "junk" neutrals (such as those from bremsstrahlung or hadronic interactions in the calorimeter) or from neutral energy which results from the $B^- \to D^0\ell^-\overline{\nu}_\ell X$ process but which is not added into the reconstruction (such as the π^0 or photon from D^{*0} decay).

The E_{extra} spectrum is illustrated in Fig. 5.9 for a wide region ($0.0 \leq E_{extra} \leq 3.0\,\mathrm{GeV}$) and a narrower region ($0.0 \leq E_{extra} \leq 1.0\,\mathrm{GeV}$). Signal tends to peak near or at zero, while background processess peak near 2 GeV and fall toward zero (Fig. 5.9 and Fig. 5.10). This quantity possesses a distinct shape for signal and background and is the discriminating variable that will be used in the remainder of this analysis.

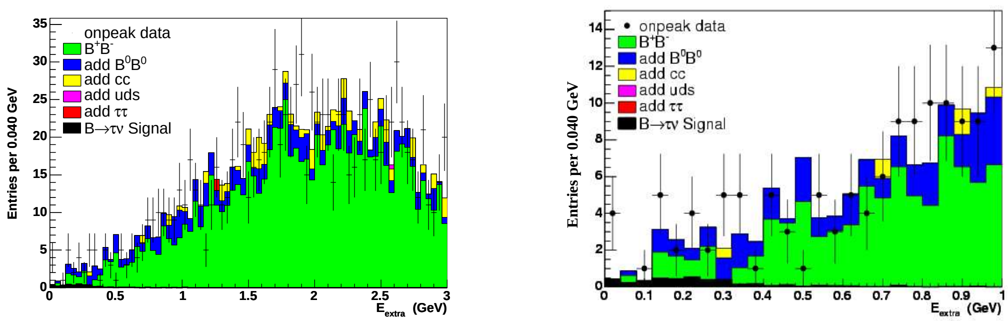

(a) E_{extra} from zero to 3.0 GeV

(b) E_{extra} from zero to 1.0 GeV

Figure 5.9: The neutral energy remaining in the calorimeter (E_{extra}), plotted after making all other cuts in the analysis. The signal simulation is normalized to a branching fraction of 1.0×10^{-4}.

5.4.1 Background Composition

The most significant contributor of background events to this search is $e^+e^- \rightarrow B^+B^-$, followed by $B^0\overline{B}^0$ and finally continuum events. A study of the B^+B^- MC events in the region $E_{extra} < 0.35$ GeV reveals that background events fall into one of several categories:

1. Events with a poorly reconstructed semi-leptonic B-meson decay on the signal side. The lepton is mistaken for a lepton from τ^+ decay while other particles have extremely low momenta (making them hard to detect) or

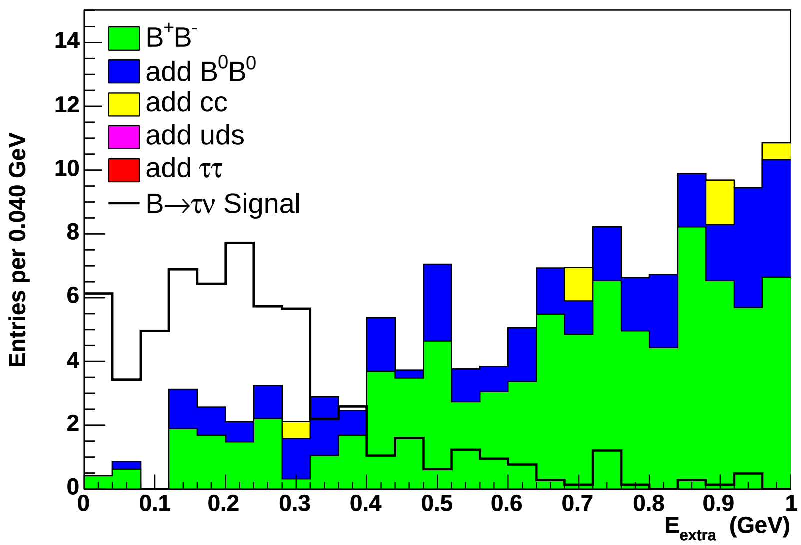

Figure 5.10: E_{extra} shown only for the signal and background Monte Carlo. The signal's "two-peak" structure is apparent.

travel at low angles and miss the tracking system and/or calorimeter. These missing particles mimic the neutrinos.

2. Events with a semi-leptonic B-meson decay where the D^0 meson decays into a K_L^0 The K_L^0 has a low reconstruction efficiency, and therefore a veto on their presence in the detector is ineffective. The energy carried by the K_L^0 mimics that carried away by neutrinos.

In almost all cases, the $B^- \to D^0\ell^-\overline{\nu}_\ell X$ is properly reconstructed and the signal side of the event contains the above features. While many of the events fall into both categories, the composition of the background is found to be 60% from K_L^0 and 40% from lost charged particles. The dominant background processes arise from $b \to c\ell\nu$ transitions (yielding leptons and D-mesons). A smaller fraction

($\sim 10\%$) arise from $b \to u\ell\nu$ transitions, yielding leptons and pions.

The significant cause of background events from $e^+e^- \to B^0\overline{B}^0$ is the loss of the low-momentum charged pion from $D^{*-} \to \overline{D}^0\pi^-$ in $B^0 \to D^{*-}\ell^+\nu$. More particles are lost in the recoiling B^0, which decays semi-leptonically, leading to missing mass. The primary lepton is then picked up as the signal track.

5.4.2 Data/MC Agreement for $p^*_{signal} > 1.2\,\mathrm{GeV/c}$

A check of the data/MC agreement on the signal-side of the analysis is done using the E_{extra} for events which have a signal track momentum (in the $\Upsilon(4S)$ frame) $p^*_{signal} > 1.2\,\mathrm{GeV/c}$. Events in this region comprise a "sideband" dominated by background with which to study the data and simulation. Using the Standard Model branching fraction, only two signal events are expected in this entire region.

As shown in Figure 5.11, the agreeement between data and simulation is good *except* at $0.2\,\mathrm{GeV/c}$. This is one of the regions where signal events are expected to collect (Fig. 5.10). The cause of the disagreement was the subject of a lengthy investigation, which is detailed in Appendix B. The result of the investigation was inconclusive, though the events in this region are expected to be dominantly background.

If the peak is due to an unsimulated background, its nature cannot be determined with existing Monte Carlo samples or with the data available in the peak at $0.2\,\mathrm{GeV}$. The current hypothesis is that this disagreement is due to insufficient modeling either of extra energy from higher-mass D^0 decay or rare $b \to c\ell\nu$ or

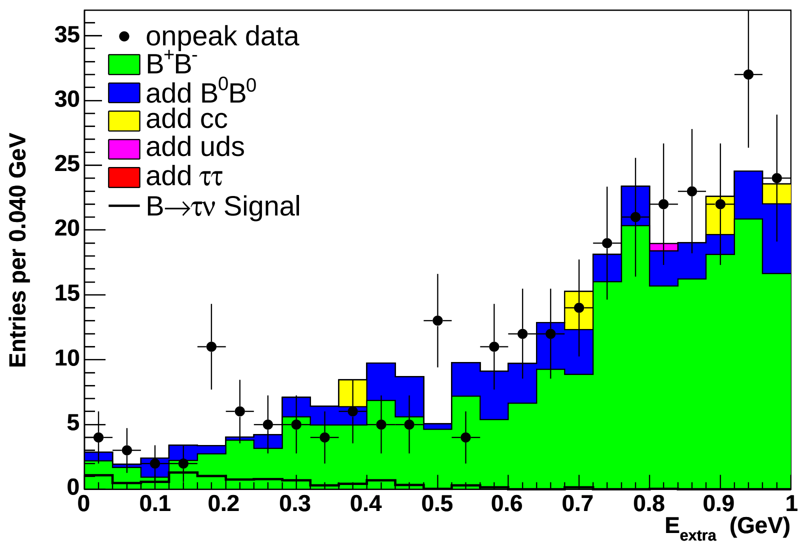

Figure 5.11: E_{extra} for events with a signal track momentum greater than 1.2 GeV/c

$b \to u\ell\nu$ transitions. If the latter is the case, the lepton spectrum from such decays is typically hard (p^* peaking well above 1.2 GeV/c) and few of these events should be left for $p^*_{signal} < 1.2$ GeV/c.

5.5 Signal Efficiency and the Background Estimate

The marginal and cumulative efficiencies of each restriction in the analysis are given in Table 5.1 for simulated signal events. With all selection criteria applied the signal efficiency (ε_s) is $(4.77 \pm 0.35) \times 10^{-4}$, where the uncertainty is purely statistical. For the Standard Model branching fraction (0.97×10^{-4}) and the number of B^+ mesons in the *BABAR* data set (88.9×10^6) $N_s \sim 4.2$ signal events are expected in the data, where

$$N_s = \mathcal{B}(B^+ \to \tau^+ \nu_\tau) \cdot N_{B^+} \cdot \varepsilon_s. \tag{5.2}$$

The marginal and cumulative efficiencies of each restriction in the background simulation (for each species including B^+B^-, $B^0\overline{B}^0$, the light quark continuum (uds), $c\overline{c}$, and $\tau^+\tau^-$) are given in Table 5.2. The expected background yield from simulation is determined to be 123.94 ± 6.90 events.

Since most of the signal events lie below $E_{extra} \approx 0.35\,\mathrm{GeV}$ it is instructive to examine the signal efficiency and background estimation in that region. In this region the signal efficiency is 3.8×10^{-4} and the background estimate is 16.12 ± 2.28 events. This signal efficiency yields an estimate of 3 signal events in our data, yielding a signal-to-background ratio of 1:5 for $E_{extra} < 0.35\,\mathrm{GeV}$.

If a Cousins-Feldman [35] procedure were use to set a limit using a "cut-and-count" approach, the expected nominal limit on the branching fraction would be $\mathcal{B}(B^+ \to \tau^+\nu_\tau) < 3.0 \times 10^{-4}$ at the 90% confidence level. However, this approach is limited by the large uncertainty in the background estimate (see Fig. 5.12). The region which contains most of the signal events is $E_{extra} < 0.35\,\mathrm{GeV}$; the limit is stable throughout the energy spectrum up to a cut at $E_{extra} < 5.0\,\mathrm{GeV}$. Therefore, two areas of interest in the energy spectrum are defined: the *energy sideband*, where $E_{extra} > 0.5\,\mathrm{GeV}$ and the *signal region*, where $E_{extra} < 0.35\,\mathrm{GeV}$. The region in between these two zones is taken as a buffer.

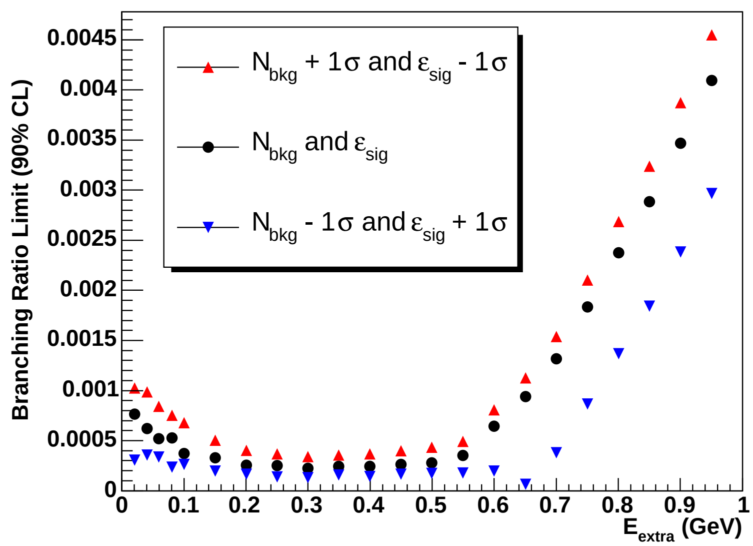

Figure 5.12: The variation in the upper limit that can be set (using the Cousins-Feldman method) versus the cut on the extra neutral energy.

Table 5.1: The marginal and cumulative efficiencies of the cut-based analysis on Signal MC. The signal MC has been normalized to the data luminosity assuming a branching fraction of 1×10^{-4}.

Selection	Number Passing (Cumulative Eff.) (Marginal Eff.)
Generated	8887.042
Semi-leptonic B-meson Reconstruction (Chapter 4)	39.595 ± 0.937 (0.4455%)(69.27%)
One Signal Side Track	32.802 ± 0.858 (0.3691%)(82.84%)
$\tau\tau$ Veto	31.181 ± 0.839 (0.3509%)(95.06%)
$D_{xy} < 0.1\,cm$ if $p_{lab} > 0.6\,GeV$	30.463 ± 0.830 (0.3428%)(97.70%)
Kaon Veto	29.057 ± 0.810 (0.3270%)(95.39%)
Lepton ID	6.707 ± 0.394 (0.0755%)(23.08%)
$p^*_\ell < 1.2\,GeV$	4.370 ± 0.318 (0.0492%)(65.16%)
$E_{extra} < 1.0\,GeV$	4.235 ± 0.314 (0.0477%)(96.91%)

Table 5.2: The effect of the selection criteria as applied to the Generic MC and Onpeak Data.

Selection	Number Passing (Cumulative Eff.) (Marginal Eff.)						
	$B^+\ B^-$	$B^0\ \overline{B}^0$	$c\overline{c}$	uds	$\tau^+\ \tau^-$	Total MC	Onpeak Data
Generator Level	44435168.000	44435154.000	106433399.000	171112594.000	76959665.000	443375980.000	1108551025.000
Semi-leptonic B-meson Reconstruction (Chapter 4)	110262.606 (0.2481%)(59.65%)	38743.255 (0.0872%)(42.29%)	23839.231 (0.0224%)(34.48%)	1698.793 (0.0010%)(27.76%)	79.901 (0.0001%)(20.27%)	174623.786 (0.0394%)(49.59%)	158539.000 (0.0143%)(48.28%)
One Signal Side Track	9479.421 (0.0213%)(8.60%)	1973.303 (0.0044%)(5.09%)	3679.849 (0.0035%)(15.44%)	183.623 (0.0001%)(10.81%)	56.093 (0.0001%)(70.20%)	15372.289 (0.0035%)(8.80%)	16312.000 (0.0015%)(10.29%)
$\tau\tau$ Veto	8948.869 (0.0201%)(94.40%)	1775.848 (0.0040%)(89.99%)	3051.100 (0.0029%)(82.91%)	133.759 (0.0001%)(72.84%)	17.892 (0.0000%)(31.90%)	13927.468 (0.0031%)(90.60%)	14635.000 (0.0013%)(89.72%)
$D_{xy} < 0.1\,cm$ if $p_{lab} > 0.6\,GeV$	8648.401 (0.0195%)(96.64%)	1713.366 (0.0039%)(96.48%)	2933.336 (0.0028%)(96.14%)	124.367 (0.0001%)(92.98%)	16.822 (0.0000%)(94.02%)	13436.293 (0.0030%)(96.47%)	14066.000 (0.0013%)(96.11%)
Kaon Veto	7793.066 (0.0175%)(90.11%)	1575.624 (0.0035%)(91.96%)	2407.162 (0.0023%)(82.06%)	109.098 (0.0001%)(87.72%)	16.822 (0.0000%)(100.00%)	11901.772 (0.0027%)(88.58%)	12379.000 (0.0011%)(88.01%)
Lepton ID	2835.013 (0.0064%)(36.38%)	364.745 (0.0008%)(23.15%)	125.433 (0.0001%)(5.21%)	5.146 (0.0000%)(4.72%)	3.038 (0.0000%)(18.06%)	3333.373 (0.0008%)(28.01%)	3653.000 (0.0003%)(29.51%)
$p^*_\ell < 1.2\,GeV$	983.470 ± 19.229 (0.0022%)(34.69%)	162.672 ± 7.644 (0.0004%)(44.60%)	79.304 ± 9.812 (0.0001%)(63.22%)	1.104 ± 0.781 (0.0000%)(21.46%)	3.038 ± 2.148 (0.0000%)(100.00%)	1229.588 ± 23.015 (0.0003%)(36.89%)	1227.000 ± 35.029 (0.0001%)(33.58%)
$E_{extra} < 1.0\,GeV$	85.680 ± 5.661 (0.0002%)(8.71%)	34.760 ± 3.542 (0.0001%)(21.37%)	3.498 ± 1.746 (0.0000%)(4.41%)	0.000 ± 0.000 (0.0000%)(0.00%)	0.000 ± 0.000 (0.0000%)(0.00%)	123.938 ± 6.903 (0.0000%)(10.08%)	130.000 ± 11.402 (0.0000%)(10.59 %)

Table 5.3: The effect of the selection criteria in continuum MC and offpeak data. The offpeak data has been scaled to the onpeak data luminosity.

Selection	Number Passing (Cumulative Eff.) (Marginal Eff.)				
	$c\bar{c}$	uds	$\tau^+\tau^-$	Total MC	Offpeak Data
Generator Level	106433399.000	171112594.000	76959665.000	354505658.000	117990000.000
Semi-leptonic B-meson Reconstruction (Chapter 4)	23839.231 (0.0224%)(34.48%)	1698.793 (0.0010%)(27.76%)	79.901 (0.0001%)(20.27%)	25617.925 (0.0072%)(33.87%)	26365.000 (0.0223%)(33.38%)
One Signal Side Track	3679.849 (0.0035%)(15.44%)	183.623 (0.0001%)(10.81%)	56.093 (0.0001%)(70.20%)	3919.565 (0.0011%)(15.30%)	4614.900 (0.0039%)(17.50%)
$\tau\tau$ Veto	3051.100 (0.0029%)(82.91%)	133.759 (0.0001%)(72.84%)	17.892 (0.0000%)(31.90%)	3202.751 (0.0009%)(81.71%)	3786.000 (0.0032%)(82.04%)
$D_{xy} < 0.1\,cm$ if $p_{lab} > 0.6\,GeV$	2933.336 (0.0028%)(96.14%)	124.367 (0.0001%)(92.98%)	16.822 (0.0000%)(94.02%)	3074.525 (0.0009%)(96.00%)	3538.000 (0.0030%)(93.45%)
Kaon Veto	2407.162 (0.0023%)(82.06%)	109.098 (0.0001%)(87.72%)	16.822 (0.0000%)(100.00%)	2533.082 (0.0007%)(82.39%)	2871.000 (0.0024%)(81.15%)
Lepton ID	125.433 (0.0001%)(5.21%)	5.146 (0.0000%)(4.72%)	3.038 (0.0000%)(18.06%)	133.616 (0.0000%)(5.27%)	153.830 (0.0001%)(5.36%)
$p^*_\ell < 1.2\,GeV$	79.304 ± 9.812 (0.0001%)(63.22%)	1.104 ± 0.781 (0.0000%)(21.46%)	3.038 ± 2.148 (0.0000%)(100.00%)	83.446 ± 10.075 (0.0000%)(62.45%)	94.844 ± 28.295 (0.0000%)(61.01%)
$E_{extra} < 1.0\,GeV$	3.498 ± 1.746 (0.0000%)(4.41%)	0.000 ± 0.000 (0.0000%)(0.00%)	0.000 ± 0.000 (0.0000%)(0.00%)	3.498 ± 1.746 (0.0000%)(4.19%)	8.531 ± 8.531 (0.0000%)(9.00%)

5.6 The Determination of the Signal Content in Data

The extra neutral energy distributions have distinctive shapes for both signal and background processes. While a traditional cut-and-count analysis can be used to pursue the branching fraction, the large signal-to-background ratio (1:5) and background estimate uncertainty makes this approach impractical. Instead, the use of the shape information in the neutral energy provides a powerful tool to determine the signal and background contributions to the neutral energy spectrum. In the following sections, the models used for signal and background neutral energy are outlined. These models are then combined in an extended likelihood procedure.

The cut on the signal-track momentum (Section 5.3) is removed when constructing the models for signal and background. The neutral energy shape does not depend significantly on the momentum of the signal track. Removing the cut increases the statistical sample size from which the models can be constructed.

5.7 The Model for E_{extra} in Signal Events

The distribution of E_{extra} for signal events is shown in Fig. 5.13. The distribution has two very distinct features: a peak at zero and a separate peak near 0.2 GeV. Studies of the simulation reveal that these peaks are due to two separate phenomena:

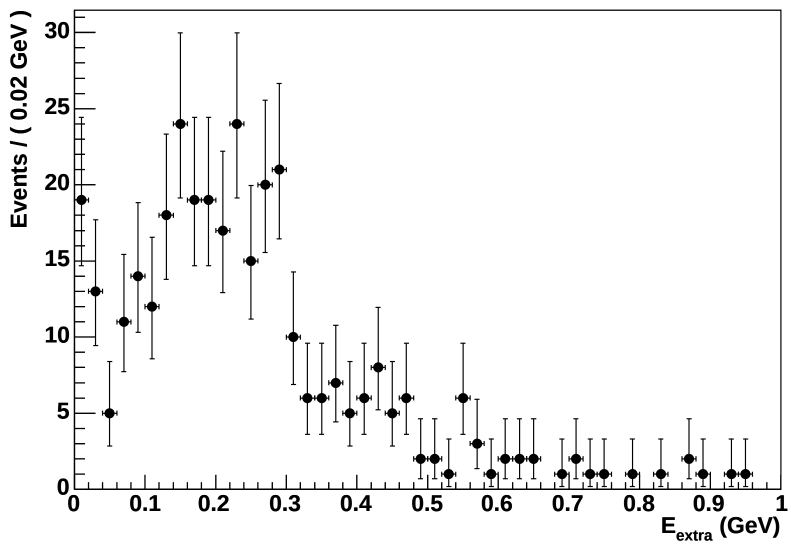

Figure 5.13: The distribution of extra neutral energy for signal events.

1. The peak at zero is the result of events with little or no energy leftover in the EMC. The physics behind this is that the tag B meson decays as $B^- \to D^0\ell^-\nu$. All detectable particles from this tag B are reconstructed, leaving no or very little unassociated neutral energy. These events peak at zero and fall sharply as E_{extra} becomes larger. The E_{extra} spectrum is here mainly due to "junk" neutrals, such as those from bremsstrahlung or hadronic splitoffs (Fig. 5.14(a))

2. The peak near 0.2 GeV is due to the unassociated neutral daughters of D^{*0} decay ($D^{*0} \to D^0\pi^0$ and $D^{*0} \to D^0\gamma$). The neutral daughter (photons either directly from the D^{*0} or from a π^0) tend to have an energy of 0.150 GeV, due to the difference between the mass of the D^{*0} and D^0 mesons. These

photons are mixed with neutral particles from other sources and the peak shifts upward to 0.2 GeV. These events also contain contributions from junk neutrals and form the tails to either side of the peak (Fig. 5.14(b)).

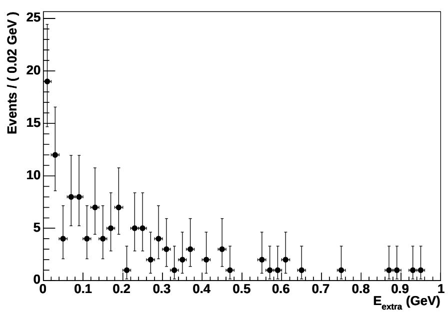

(a) Extra neutral energy from events without a D^{*0} daughter which strikes the calorimeter

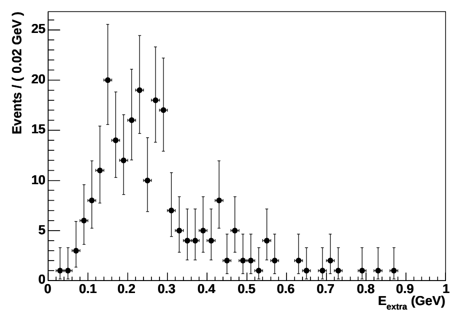

(b) Extra neutral energy from events with a D^{*0} daughter that strikes the calorimeter.

Figure 5.14: Extra neutral energy in the two classes of signal events: those with and without a neutral daughter from D^{*0} decay striking the calorimeter.

This spectrum is modeled in two stages: PDFs describing events with junk neutrals and those with neutrals from D^{*0} decay are constructed and then combined into a single function to describe the E_{extra} shape in signal events. An event is defined as having a neutral from D^{*0} decay if there is a neutral object in the calorimeter which can be matched to a true particle from the simulation which originated from D^{*0} decay. This truth matching is done using a χ^2 method and is not perfectly efficient. The distribution in Fig. 5.14(b) is the result of this definition.

The junk spectrum is modeled with a modified exponential function,

$$f(E_{extra}) = \frac{1}{a_0 + E_{extra}} e^{a_1 E_{extra}} \tag{5.3}$$

where a_0 serves as a cutoff to prevent the fit from blowing up at zero, and where a_1 controls the slope of the exponential. This model accomodates a sharp peak at zero and falls rapidly above zero. The parameters of the fit (a_0 and a_1) of this function to the junk E_{extra} spectrum are given in Table 5.4 and illustrated in Fig. 5.15(a).

The E_{extra} spectrum for events with visible D^{*0} events is modeled using a double-Gaussian (one for the peak near 0.2 GeV and a second for the wide tail to the right of the peak). The parameters of this fit are given in Table 5.5 and illustrated in Fig. 5.15(b).

The combined signal PDF is then determined by adding the junk and D^{*0} PDFs. MINUIT is then used to fit for the fraction that the D^{*0} portion contributes to the total distribution. Fitting for the value of this fraction is a cross-check on the behavior of the fit. This fraction is determined to be $(69.8 \pm 4.4)\%$ by the fit and is in agreement with the actual fraction in the signal simulation sample, $(62.3 \pm 5.6)\%$.

5.7.1 Validation of the Signal Model

The physics of the signal MC shape has been established by a study of the underlying true particles in the MC events. To validate the physics of this shape,

Table 5.4: The parameters for the portion of the signal E_{extra} spectrum caused by "junk" neutrals.

Parameter	Value
Cutoff (a_0)	0.0409 ± 0.0302
Exponent (a_1)	-1.091 ± 0.711

Table 5.5: The parameters for the portion of the signal E_{extra} spectrum caused by neutrals from D^{*0} decay.

Parameter	Value
Mean, Peak Gaussian (m1)	0.2065 ± 0.0083 GeV
Width, Peak Gaussian (s1)	0.0717 ± 0.0074 GeV
Mean, Tail Gaussian (m2)	0.401 ± 0.053 GeV
Width, Tail Gaussian (s2)	0.182 ± 0.026 GeV
Fraction of Fit Occupied by Peak Gaussian	0.658 ± 0.085

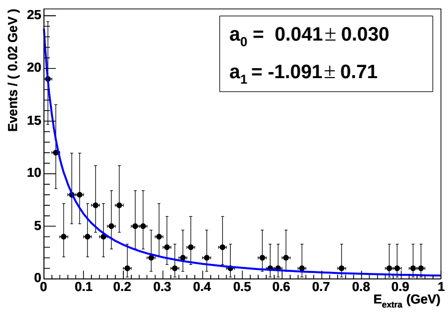

(a) The E_{extra} spectrum for events containing neutrals from sources such as bremsstrahlung or hadronic splitoffs. The blue line is the model used to fit this spectrum.

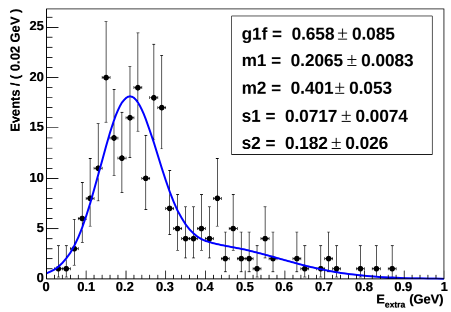

(b) The E_{extra} spectrum for events containing neutrals from D^{*0} decay. The blue line is the model used to fit this spectrum.

Figure 5.15: The distributions of E_{extra} for the two classes of events in the signal MC and the models used to describe each class.

a control sample is contructed using the following topology:

$$B^- \to D^0 \ell^- \overline{\nu}_\ell X \; , \; B^+ \to \overline{D}^{*0} \ell^+ \nu \tag{5.4}$$

The first B-meson is reconstructed as in the search for $B^+ \to \tau^+ \nu_\tau$. Events are then required to contain a second $D\ell$ candidate which does not overlap with the first. If neutral particles exist in the event, they are associated with the second $D\ell$ candidate to determine if the $\overline{D}^0$ is a result of $\overline{D}^{*0}$ decay. The following requirements are applied to the neutral particles and to the $\overline{D}^{*0}$ candidate to determine if they are consistent with above topology (these are derived from *BABAR*'s official $\overline{D}^{*0}$ selection, detailed in [36]).

- $D^{*0} \to D^0 \gamma$

- $0.07 < E^{\gamma}_{cms} < 0.40\,\mathrm{GeV}$
- $LAT_{\gamma} < 0.8$
- Shower energy of the photon $> 0.1\,\mathrm{GeV}$
- CMS angle between the D^0 and γ is < 2.0 radians

- $D^{*0} \rightarrow D^0\pi^0$
  - $0.125 < E^{\pi^0}_{cms} < 0.30\,\mathrm{GeV}$
  - $LAT < 0.8$ (for each photon)
  - Shower energy of the higher-energy photon $> 0.05\,\mathrm{GeV}$
  - Shower energy of the lower-energy photon $> 0.03\,\mathrm{GeV}$
  - CMS angle between the D^0 and π^0 is < 0.8 radians
  - CMS angle between the D^0 and higher-energy photon is < 1.57 radians

- The best candidate is selected as the one whose $M(D^0 - D^{*0})$ is closest to the value obtained by subtracting the PDG values for these quantities.

These events should contain a very similar neutral energy distribution to that expected from signal events for several reasons:

- The semi-leptonic B-meson decay is identical to that used in the signal search. Therefore, there can be a potentially unassociated neutral which is left in the calorimeter.

- The second $D\ell$ has all of its neutrals reclaimed, including those from $\overline{D}^{*0}$ decay. The remaining decay products of the $D\ell$ are all either charged tracks or π^0 which are used to construct the $\overline{D}^0$.

This control sample is developed in both data and MC. The comparison of the E_{extra} spectrum in this sample is illustrated in Fig. 5.16. The agreement in the shape is excellent between data and MC. In addition, the distribution exhibits all the features that are expected of events which have only one unclaimed neutral from the $B^- \rightarrow D^0\ell^-\overline{\nu}_\ell X$ decay. The distribution in data is then fitted using the signal model; only the parameters of the junk model are fixed, since the convergence of the fit is sensitive to the cutoff parameter (a_0) in the junk model. A comparison between the fit parameters in data and in signal MC is given in Table 5.6.

The agreement between the data and signal MC in the expected model parameters is excellent. One interesting possible disagreement is in the total yield of events that contain a D^{*0}. While the fractions in Table 5.6 agree within the statistical uncertainty, there is the possibility that the fractions in data and Monte Carlo may, in fact, be different. This stems from the fact that the existing measurement of the D^{*0} branching fraction still has a $\sim 10\%$ uncertainty. The central value used in at the generator level (taken from the PDG in 2000) could be lower than the true central value, leading to a lower fitted fraction in signal Monte Carlo than in the double-tag control sample.

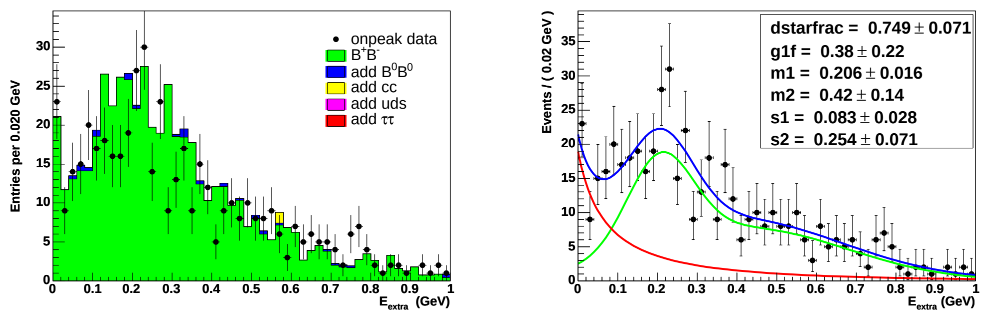

(a) A comparison between the data and MC for E_{extra} in the $B^- \rightarrow D^0\ell^-\overline{\nu}_\ell X, B^+ \rightarrow \overline{D}^{*0}\ell^+\nu$ control sample

(b) The data in the $B^- \rightarrow D^0\ell^-\overline{\nu}_\ell X, B^+ \rightarrow \overline{D}^{*0}\ell^+\nu$ are fit using the signal E_{extra} model.

Figure 5.16: The $B^- \rightarrow D^0\ell^-\overline{\nu}_\ell X, B^+ \rightarrow \overline{D}^{*0}\ell^+\nu$ control sample is used to validate the signal model for E_{extra}.

The uncertainty in the parameters is used in Section 7.3.5 to test the stability of the limit setting procedure.

5.8 The Model for E_{extra} in Background Processes

The distribution of neutral energy for purely background processes is shown in Fig. 5.9. The distribution falls toward zero with no apparent peaking structures in the signal region ($E_{extra} < 0.35\,\mathrm{GeV}$). Several models are tried to fit the spectrum and all are found to be in good agreement with the distribution. These models and their parameters are given in Table 5.7.

The polynomial fit is chosen as the nominal model for the background. After the limit setting procedure is outlined in the next few sections, these other models will be used to study the dependence of the sensitivity on the parameterization.

Table 5.6: A comparison of the parameters of the signal PDF as determined from signal MC and a data control sample of $B^- \to D^0\ell^-\overline{\nu}_\ell X, B^+ \to \overline{D}^{*0}\ell^+\nu$ events.

Fit Parameter	Value in Signal MC	Value in data for the $B^- \to D^0\ell^-\overline{\nu}_\ell X, B^+ \to \overline{D}^{*0}\ell^+\nu$ sample
Peak Gaussian Mean	0.207 ± 0.008	0.206 ± 0.016
Peak Gaussian Width	0.072 ± 0.007	0.083 ± 0.028
Tail Gaussian Mean	0.401 ± 0.053	0.42 ± 0.14
Tail Gaussian Width	0.182 ± 0.026	0.254 ± 0.071
D^{*0} Fraction	0.698 ± 0.044	0.749 ± 0.071

The models used to fit the spectrum are illustrated in Fig. 5.17.

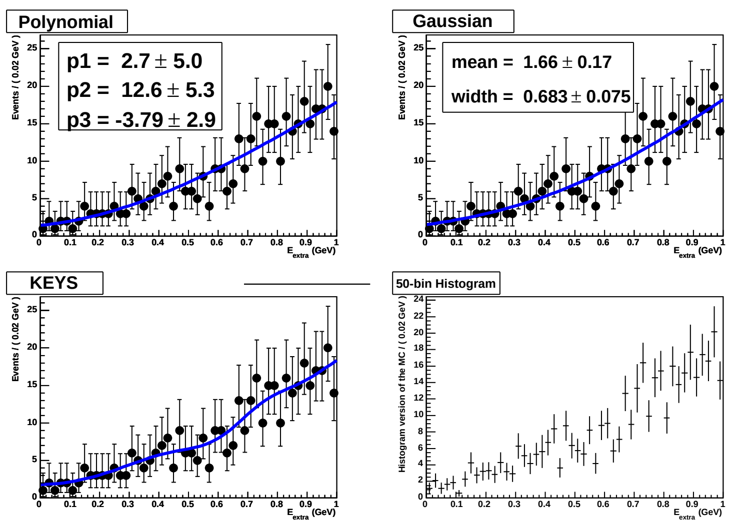

Figure 5.17: Background PDFs from remaining neutral energy distributions in background MC. The fits are performed in the range $[0.0, 1.5]$ but only the range from $[0.0, 1.0]$ is shown.

Table 5.7: Background models and their parameters

Model Type	Parameters
Polynomial	Constant 0 $= 2.7 \pm 5.0$ Constant 1 $= 12.6 \pm 5.3$ Constant 2 $= -3.79 \pm 2.9$
Gaussian	Mean $= 1.66 \pm 0.17$ Width $= 0.683 \pm 0.075$
Histogram	Number of Bins = 50
KEYS [37]	Not Applicable

5.9 The Extended Maximum Likelihood Function

The nominal PDFs from sections 5.7 and 5.8 are combined in a single extended maximum likelihood function with the following form:

$$\mathcal{L}(E_{extra}) = e^{-(\mu_s+\mu_b)} \sum_{i=1}^{n} \left[\mu_s \, F_s(E_{extra,i}) + \mu_b \, F_b(E_{extra,i})\right] \tag{5.5}$$

where μ_s and μ_b are the signal and background yields to be fitted, $F_s(E_{extra,i})$ ($F_b(E_{extra,i})$) is the PDF for signal (background), and n is the number of events in the data sample. The exponential in front of the sum over all events is a Poisson term that handles fluctuations in the number of events in different data samples, and the sum over all events in a given data sample accounts for the contributions of signal and background to a given data sample.

5.9.1 The Fit to Extract the Signal and Background Yields

Toy MC is generated by sampling the signal and background PDFs using the *accept/reject method* [38]. The requested number of events in each sample is equal to the sum of the signal hypothesis and the expected background. The total number of events for each "experiment" is sampled from a Poissonian around the requested number of events. Each sample is then fit using the extended maximum likelihood function to determine if the fit exhibits any bias. For each signal hypothesis, 5000 experiments are generated. The results of the 5000 fits are shown in Fig. 5.18 for several signal hypotheses. Some of the example fits in Fig. 5.18 suggest a small bias which is nonetheless larger than the uncertainty in the fitted mean. Such a small bias (~ 0.2 events) is not a concern to the result of the fit, given the much larger overall width of the fitted yield distribution (~ 10 events).

The results of these tests suggest that the fit exhibits no significant bias and over a large ensemble of experiments will on average fit back the true signal content of the sample.

As a separate test of the fit, two background-only samples are constructed using Monte Carlo data. The samples are taken from GEANT4 simulations of generic background processes with the full *BABAR* detector simulation. The size of each sample is determined using the data luminosity, and preserve the statistical uncertainty associated with the data set size. Each of these experiments is fit using the extended maximum likelihood function to determine the signal and background content of the samples. The results of the fit are given in Table 5.8 and shown in Fig. 5.19. The results of the fits are consistent with their zero signal content.

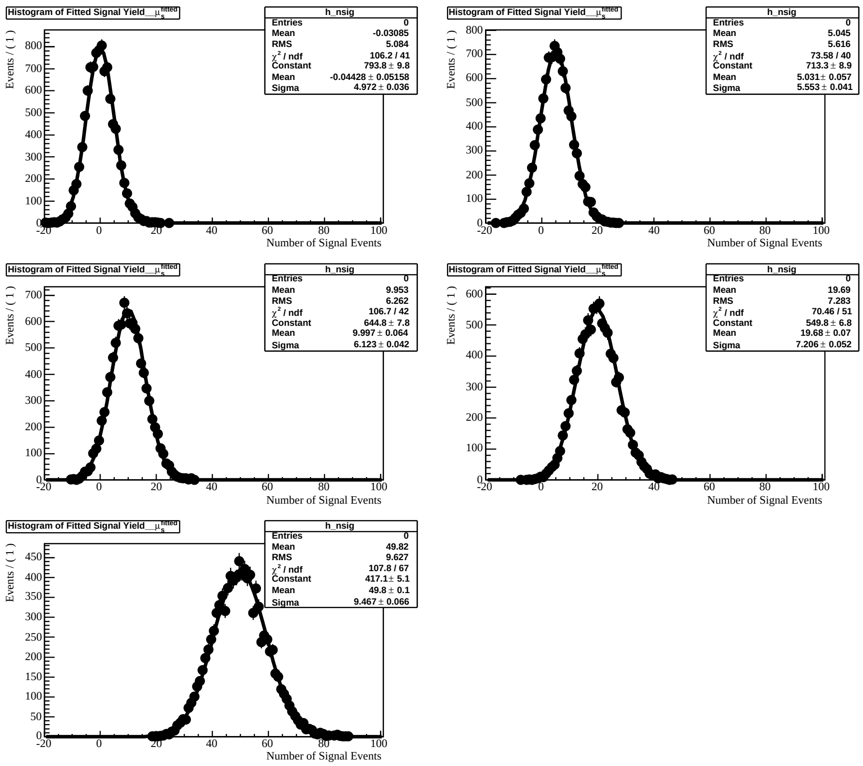

Figure 5.18: The fitted signal yield distribution for a number of input signal hypotheses. The number of signal events input to the toy MC samples is (from left to right, top to bottom), 0.0, 5.0, 10.0, 20.0, and 50.0.

Table 5.8: Two independent GEANT4 MC samples are constructed. The samples contain only background events. The neutral energy in each is fit using the extended maximum likelihood function. The fitted background yields are consistent with the number of background events in the sample, and the fitted signal yields are consistent with 0.0.

GEANT 4 Sample	Fitted Signal Yield	Fitted Background Yield	True Background
1	4.33 ± 5.76	$123.67 + -12.34$	128 ± 11
2	0.22 ± 4.86	$121.78 + -12.05$	122 ± 11

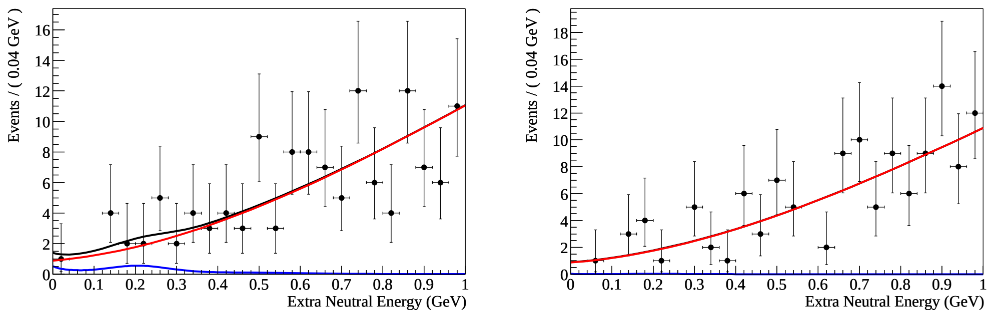

Figure 5.19: Two "experiments" are derived from the `GEANT` MC sample. Each experiment is composed of non-overlapping $B\bar{B}$ MC and overlapping continuum MC due to an insufficient sample of continuum. All cuts used in the analysis are applied to the experiments and the E_{extra} spectrum, shown above for each, is fitted to obtain the signal and background yield in the sample. The fits, also shown above, are both consistent with the background-only composition of the sample.

5.9.2 Background Expectation from Data

Rather than relying entirely on the background simulation to derive the background expectation, an estimate is pursued using the data. All selection criteria are applied to the data. The data in the energy sideband, $0.5 < E_{extra} < 1.0\,\text{GeV}$, is then extrapolated into the signal region ($E_{extra} < 0.5$) using the nominal background model. In addition, the extrapolation is performed using the other models outlined in section 5.8. There are 92.0 ± 9.6 events in the data energy sideband. The results of the extrapolation are shown in Table 5.9.

The background expectation from simulation was 123.94 ± 6.90, which agrees very well with the expectation from the data (119.8 ± 12.5) and Monte Carlo

Table 5.9: The data in the energy sideband is extrapolated into the signal region using several background models.

Background Model	Number of Events in the sideband	Fraction of Background PDF in sideband	Expected Background (MC)	Expected Background (Data)	Expected Background (Data) ($E_{extra} < 0.35\,\mathrm{GeV}$)
3rd-order Polynomial	92.0 ± 9.6	0.768	123.94 ± 6.90	119.8 ± 12.5	14.6 ± 1.5
Gaussian	92.0 ± 9.6	0.767	123.94 ± 6.90	120.0 ± 12.5	15.1 ± 1.6
KEYS	92.0 ± 9.6	0.761	123.94 ± 6.90	120.9 ± 12.6	15.7 ± 1.6
50-Bin Histogram	92.0 ± 9.6	0.758	123.94 ± 6.90	121.4 ± 12.7	15.5 ± 1.6

(123.94 ± 6.90). This method relies on agreement between the background model and the true data background shape for $E_{extra} < 0.5\,\mathrm{GeV}$. Variations in the true vs. expected background level and their effects on the limit setting procedure are explored in section 7.3.1.

5.10 The Fit to Extract the Signal and Background Yields in Data

Having established the models for the signal and background neutral energy contributions, the likelihood fit is applied to the data. All selection criteria outlined in Tables 4.3 and 5.1 are applied to the data. The extra neutral energy spectrum is then fit using the maximum likelihood function (Equation 5.5). The result of the fit is is illustrated in Fig. 5.20.

The fitted signal yield is 14.8 ± 6.3 and the fitted background yield is 115.2 ± 11.8. The background expectation obtained by extrapolating the background in the energy sideband into the signal region is 119.8 ± 12.5, and agrees well with the data. For a Standard Model branching fraction of 0.97×10^{-4}, 4.2 signal events are expected in this sample.

The number of signal events expected from the Standard Model is small. If we assume that the branching fraction is up by one standard deviation from the central value, that yields $\mathcal{B}(B^+ \to \tau^+\nu_\tau)_{SM+1\sigma} = 1.36 \times 10^{-4}$ for an expected number of signal events of 8.4 events. The difference between the number of signal events from the Standard Model central value and the value inflated by 1σ is comparable to the uncertainty in the fit. This analysis is not sensitive enough to say with certainty whether signal is present in the data. Therefore, a limit will be set on the signal content of the data. The next chapter will outline the corrections that need to be applied to the raw signal efficiency obtained in this chapter, along with the uncertainty on those corrections. Chapter 7 discusses the procedure which is used to set a limit on the fitted signal yield.

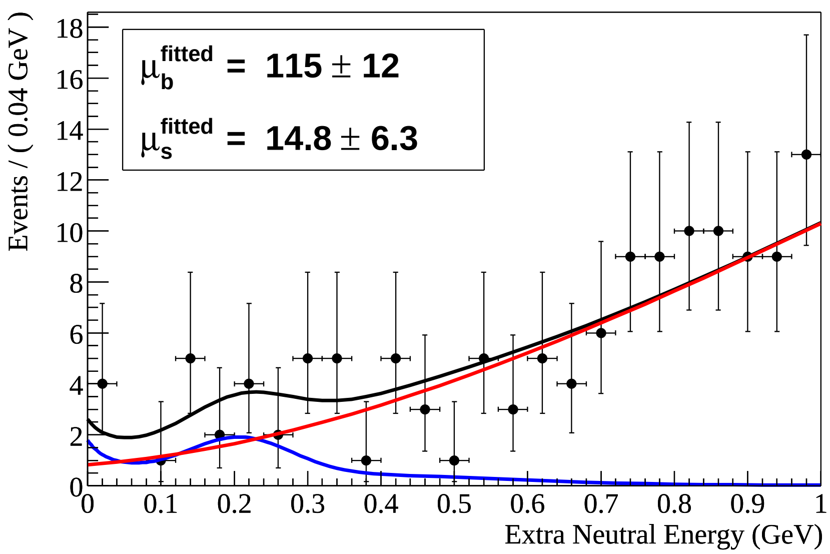

Figure 5.20: The fit of the likelihood function to data, after applying all selection criteria.

Chapter 6

Systematic Corrections and Uncertainties on the Signal Efficiency

Two classes of systematic effects in the analysis are now explored: the stability of the limit setting procedure and the systematic differences between efficiency in the data and the simulation. The major effects of concern to this work are differences between data and Monte Carlo for the following areas:

1. the efficiency with which $B^- \to D^0\ell^-\overline{\nu}_\ell X$ is reconstructed,
2. the modeling of the particle identification efficiency,
3. the modeling of the calorimeter, and
4. the tracking efficiency.

To explore the effects of differences in tag B efficiency the *double-tagged events sample*, outlined in 4.9), will be used. To explore the remaining effects, techniques will be used that have been developed by working groups at *BABAR*.

These techniques are used to correct differences in data and simulation for particle identification and neutral energy.

6.1 Systematic Correction of the Semi-Leptonic B Reconstruction Efficiency

The procedure for determing this systematic correction factor for the semi-leptonic B meson reconstruction efficiency was outlined in section 4.9. The procedure involves comparing the number of single and double-tagged events in data and simulation. From that comparison a correction factor is derived,

$$\varepsilon^{data}_{B^-\to D^0\ell^-\overline{\nu}_\ell X}/\varepsilon^{MC}_{B^-\to D^0\ell^-\overline{\nu}_\ell X} = 0.882 \pm 0.031$$

This correction and its uncertainty are taken to be the systematic correction for the semi-leptonic B meson efficiency. This correction factor contains all possible systematic effects which can cause differences between data and simulation (tracking reconstruction efficiency, particle identification, and calorimeter simulation) in the semi-leptonic B meson.

6.2 Systematic Uncertainty from Particle Identification

The performance of the various particle identification tools may differ when used in data versus in simulation. As a result a systematic correction and an uncertainty on that correction must be applied. This section details the method used to determine this correction to the signal efficiency in this search.

As discussed in Section 3.2.4.1, PID killing is applied to both signal and

Table 6.1: The selection criteria used to generate custom PID tables.

PID Table	Selection Criteria
Muon	`NOT(knnVeryLoose) AND isMuMicroTight`
Electron	`NOT(knnVeryLoose) AND isEMicroVeryTight`

background Monte Carlo to reproduce the data PID efficiency. However, since only the PID tables associated with the true particle type are used (muon tables for muons, etc), if a variety of selections are applied to the same track at analysis time the possible *correlations* between selectors are not reproduced. Since in this search a kaon veto and a lepton acceptance are applied, there may be an effect from a correlation between the two algorithms. Therefore, a custom set of PID tables is generated which contain the selection criteria outlined in Table 6.1.

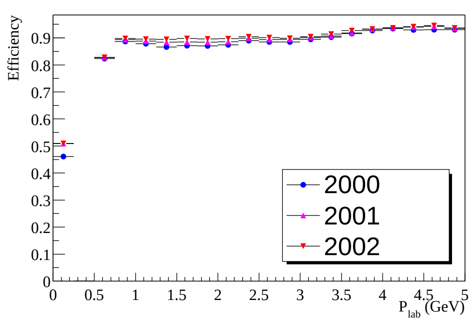

(a) The efficiency of the kaon veto and electron selection as a function of momentum and year.

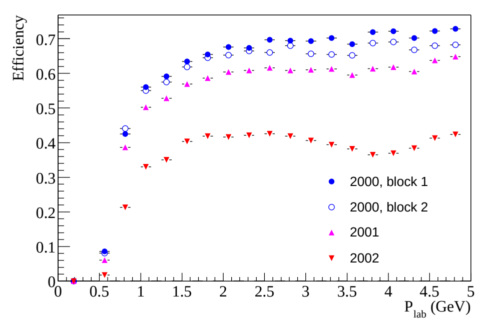

(b) The efficiency of the kaon veto and muon selection as a function of momentum and year.

Figure 6.1: The efficiency of the custom particle identification selection used for the signal track as a function of momentum in the laboratory frame, year and lepton species.

The PID tables are divided into 19 p_{lab} bins of 0.250 GeV except for the first bin, which is 0.5 GeV wide. They are simultaneously binned in 14 θ_{lab} bins and one ϕ_{lab} bin. The momentum dependence of the selectors is the most important consideration; the θ_{lab} dependence is also a factor in some regions of the detector where there are gaps or changes in detector resolution, while in ϕ_{lab} the particle identification is very uniform.

The dependence of the efficiency for muons and electrons for these tables as a function of momentum and year is illustrated in Fig. 6.1. The muon efficiency's time dependence is significant due to the change in performance of the muon system between 1999-2002.

The next step in the procedure is to compare the performance of the PID-killed simulation to that obtained by using these custom PID tables, which take into account any correlation between the kaon and muon/electron selection. This is done as follows:

- Construct a sample of true signal leptons from signal simulation.
- Using the p_{lab}, θ_{lab}, and ϕ_{lab} values for each charged track, determine the corresponding PID weights from the PID table. Sum the weights to obtain the expected efficiency of selecting signal leptons. This yields and effective effiency, denoted ε_{table}.
- In parallel, apply the selection algorithms as they have been corrected in the simulation. This will provide the efficiency of applying the corrected algorithms to true signal leptons. This efficiency is denoted $\varepsilon_{selector}$.

- The ratio of the sum of the PID weights to the efficiency of the particle selector ($\varepsilon_{table}/\varepsilon_{selector}$) is taken as a correction to the efficiency. The uncertainty on this correction is taken as a systematic uncertainty.

A loose set of semi-leptonic B-meson reconstruction criteria are applied to the signal simulation, requiring that

- the event has a best $D\ell$ candidate which passes particle identification quality requirements (See Section 4.6),
- the $\cos\theta_{B,D\ell}$ variable for the $D\ell$ candidate lies between -2.5 and 1.1.

These loose criteria preserve the momentum spectrum of the signal lepton, a critical requirement for the proper use of the PID table on the lepton. After applying a loose semi-leptonic B-meson reconstruction all restrictions associated with the signal lepton are applied *except* the kaon veto and lepton acceptance. After this selection there are 2033 events which pass. There are 431 true muons and 431 true electrons.

6.2.1 PID Correction for Muons

Applying the PID weighting to the 431 true muons yields the results in Table 6.2. The PID tables store the uncertainty in the PID selection for each bin; this error is propagated through the sum of the weights. The total weight for these true muons, properly normalized by the size of the data set in each year, is:

$$\varepsilon^{\mu}_{table} = 0.196 \pm 0.013 \tag{6.1}$$

Table 6.2: The effect of applying PID weighting or the Muon selector and Kaon veto on a sample of true muons from τ decay in $B^+ \to \tau^+ \nu_\tau$ signal Monte Carlo

	Number of True Muons
Unweighted	431
Weighted	84.5
Selected using Muon Selector and Kaon Veto	80.2

The muon selector is also applied to the 431 true muons. The efficiency for muons passing this selector in simulation is:

$$\varepsilon^{\mu}_{selector} = 0.186 \pm 0.023 \tag{6.2}$$

where the uncertainty is statistical. The ratio of these two effiencies is then taken as a correction to the muon selector efficiency in simulation:

$$\varepsilon^{\mu}_{table}/\varepsilon^{\mu}_{selector} = 1.054 \pm 0.148 \tag{6.3}$$

The result is consistent with 1.0, which is expected if the particle identification efficiency has been properly modeled in simulation. The agreement with 1.0 also suggests that there isn't significant correlation between the muon and kaon selectors, a feature which is not reproduced by the particle ID selector corrections used in Monte Carlo.

This above correction is applied to the signal-side efficiency for events with an identified muon. There is no correction for the tag side because PID effects for the tag B are encapsulated in the double-tag correction.

Table 6.3: The effect of applying PID weighting or the Electron selector and Kaon veto on a sample of true electrons from τ decay in $B^+ \to \tau^+ \nu_\tau$ signal Monte Carlo

	Number of True Electrons
Unweighted	431
Weighted	298.3
Selected using Electron Selector and Kaon Veto	309.0

6.2.2 PID Correction for Electrons

Applying the PID weighting to the 431 true electrons yields the results in Table 6.3. The PID tables store the uncertainty in the PID selection for each bin; this error is propagated through the sum of the weights. The total weight for these true electrons, properly normalized by the size of the data set in each year, is:

$$\varepsilon^e_{table} = 0.692 \pm 0.034. \tag{6.4}$$

The electron selector is also applied to the 431 true electrons. The efficiency for electrons passing this selector in simulation is:

$$\varepsilon^e_{selector} = 0.717 \pm 0.053 \tag{6.5}$$

where the uncertainty is statistical. The ratio of these two effiencies is then taken as a correction to the electron selector efficiency in simulation:

$$\varepsilon^e_{table}/\varepsilon^e_{selector} = 0.965 \pm 0.086 \tag{6.6}$$

The result is consistent with 1.0, which is expected if the particle identification efficiency has been properly modeled in simulation. The agreement with 1.0 also suggests that there is not significant correlation between the electron and kaon selectors, a feature which is not reproduced by the particle ID selector corrections used in Monte Carlo.

This above correction is applied to the signal-side efficiency for events with an identified electron. There is no correction for the tag side because PID effects for the tag B are encapsulated in the double-tag correction.

6.2.3 Total Correction for Signal Leptons

The composition of the signal MC after applying all cuts is 68.4% electron and 31.6% muon. The corrections determined in the previous sections are then weighted according to these fractions and summed to determine the final correction. Doing so yields a total PID correction and uncertainty of

$$\varepsilon_{PID}^{Data}/\varepsilon_{PID}^{MC} = 0.987 \pm 0.074. \tag{6.7}$$

The result is consistent with a small expected correction to the particle identification efficiency and an uncertainty on the correction driven by the uncertainty both in the PID tables and the sample size of the signal MC.

6.3 Corrections from Neutral Energy

The use of neutral energy in this search can be affected by systematic differences between the simulation of the calorimeter and its real behavior. The *BABAR*

Neutrals Working Group has investigated [39] the two elements of the neutral simulation which may affect an analysis which uses neutral objects:

- the simulation of isolated photons
- the simulation of π^0s

The possibility that each of these affects the analysis is explored.

6.3.1 Effects from Isolated Photons

The behavior of a single, isolated photon is a modeling issue in the GEANT4 simulation. The *BABAR* Neutrals Working Group has explored the difference in performance of the calorimeter in data and simulation and prescribed the following procedure for assigning systematic uncertainty to decisions involving the use of isolated photons:

- The energy resolution in simulation is better than that in the real calorimeter. Therefore, a gaussian smearing should be applied to the reconstructed energy of isolated neutrals in simulation. The parameters of the smearing are determined from data control samples of $e^+ + e^- \rightarrow \tau^+ + \tau^- \rightarrow e^+\nu_e\overline{\nu}_\tau + h^-\pi^0\nu_\tau$ decays. Here, h^+ is either a π^+ or a K^+. The control samples are developed in data and simulation and the widths of the reconstructed π^0 mass are compared as a function of energy to determine how to smear the photon energy in simulation.
- The calibration parameters applied to the calorimeter in simulation need to be corrected using a polynomial whose dependent is the energy of the

neutral. This leads to a small downward shift of photon energy in the simulation.

Each of these procedures carries with it a systematic uncertainty, evaluated using data control samples and signal MC. Two sources of uncertainty contribute to the overall uncertainty in the use of neutrals in the simulation: uncertainties from sources whose error is correlated with that in the simulation and from sources which are uncorrelated with the neutral simulation. The Neutrals Working Group has determined that the uncertainty from correlated sources is 2.5%, to be summed in quadrature with the uncertainty from uncorrelated sources.

The uncertainty from uncorrelated sources is determined by turning on and off the effects of these sources in the simulation and observing the change in efficiency in signal MC. The effect is illustrated in Table 6.4. The effect itself is entirely isolated to events whose $D\ell$ candidate contains a D^0 decaying into $K^-\pi^+\pi^0$. This suggests that the effect of these sources is mostly isolated to the semi-leptonic B-meson. Therefore, these effects are included in the double-tag correction. Since the effect on the recoil alone is apparently small (judging from events reconstucted in the other D^0 decay modes) the uncertainty is determined to be much less than that from correlated sources. Therefore, the uncertainty from isolated photons is determined to be 2.5%.

The correction factor applied to the signal-side efficiency is therefore 1.000 ± 0.025. This is necessary because a cut is placed at 1 GeV in E_{extra}, and the efficiency of that cut is uncertain due to uncertainty in the modeling of neutral

Table 6.4: The effect of turning on sources of uncorrelated error when applying neutral energy corrections to the signal MC. All selection criteria are applied after changing which corrections are applied in order to observe the effect on the efficiency. The effects are separated into two categories: events with a $D^0 \to K^-\pi^+\pi^0$ and events in the other three modes.

Neutral Corrections Applied	Number of Events Passing all Criteria	
	$D^0 \to K^-\pi^+, K^-\pi^+\pi^-\pi^+\pi^-, K^0_S\pi^+\pi^-$	$D^0 \to K^-\pi^+\pi^0$
Energy Smearing and Rescaling	288	235
Energy Smearing and Rescaling and Sources of Uncorrelated Error	288	222

clusters.

6.3.2 Effects from π^0s

The primary effect of concern from neutral simulation is the change in the E_{extra} spectrum with difference in the data and simulation behavior of the calorimeter. The extra neutral energy is determined only using the most basic calormeter objects, from which higher objects (like π^0) are constructed. Therefore, it is expected that the effect on the recoil side of the event is small due to the simulation of π^0 decay and interaction, since π^0 energy is not a component of the E_{extra} (except in the form of photons which strike the calorimeter; these are handled in the previous section). The reconstructed π^0 candidates are only used in forming D^0 mesons for the semi-leptonic B-meson, so any simulation effects are covered by the double-tag correction.

Although there is no effect expected on the E_{extra} spectrum from uncertainty in π^0 simulation, the procedures suggested by the Neutrals Working Group are here explored for completeness. The working group outlines the following procedure for assessing the uncertainty in the π^0 simulation:

- The efficiency of reconstructing π^0 is higher in simulation than in data. Therefore a procedure is recommended for randomly killing π^0s in an event to better emulate the true efficiency.

This killing procedure has an associated uncertainty, again derived from two possible causes: sources which correlate and which do not correlate with the simulation of π^0s. The uncertainty determined by the working group for correlated sources is 5.0%. When processing the signal simulation with and without uncorrelated sources of error, no change in the overall signal efficiency is found.

Since the π^0 reconstruction is isolated to the $B^- \to D^0\ell^-\overline{\nu}_\ell X$ decay and is therefore covered by the double-tagging procedure, no additional systematic is assigned to the signal efficiency.

6.4 Corrections Due to Tracking Efficiency

The performance of the real tracking system (`SVT` and `DCH`) and its simulation in the Monte Carlo are not necessarily the same. The *BABAR* Tracking Efficiency Task Force has studied the performance of the *BABAR* tracking system and compared its performance in data and simulation [40]. They have determined that a flat systematic uncertainty of 0.008% should be applied for each track in the event.

The correction factor which needs to be applied to each event based on tracking performance is determined by using tracking efficiency correction tables developed by the working group. The momentum and angle of each track in the event is passed through the tables, which results in a probability that the given track would have actually been detected in simulation given its flight direction. Because the tracking simulation can both over- and under-estimate tracking efficiency in different regions, weights can be both less than and greater than one. The weights are multiplied for each track in the event, resulting in an event weight. The event weights are then summed to determine the effective number of events that should have passed based on these corrections.

Since effects from tracking on the $B^- \to D^0\ell^-\overline{\nu}_\ell X$ decay are covered by the double-tagging procedure, the only track that needs to be weighted is the signal-side track. The correction factor determined from applying the tracking efficiency tables to the signal track is 1.009. Therefore the correction to the signal efficiency and its uncertainty is determined to be 1.009 ± 0.008.

6.5 Summary of the Systematic Corrections to the Signal Efficiency

The corrections presented in the previous sections are summarized in Table 6.5. The total correction to the signal efficiency is determined to be 0.878 ± 0.076. Therefore, the corrected signal efficiency is $(4.19 \pm 0.31(stat.) \pm 0.36(syst.)) \times$

Table 6.5: The corrections (and their uncertainties) which are applied to the signal efficiency.

Source	Correction Uncertainty	Correction Factor
Tagging Efficiency	0.031	0.882
Neutrals Systematic (γ)	0.025	1.0
Neutrals Systematic (π^0)	0.0	1.0
Tracking Efficiency	0.008	1.009
Particle Identification on true signal muons	0.148	1.054
Particle Identification on true signal electrons	0.086	0.965
Combined	0.074	0.987
Total Correction to the signal efficiency	0.076	0.878

10^{-4}. These uncertainties are to be folded into the limit setting procedure to obtain a limit setting curve which inherently accounts for uncertainty in the signal efficiency.

Chapter 7

The Limit on the Branching Fraction for $B^+ \to \tau^+ \nu_\tau$

The expected Standard Model yield and the large uncertainty on the fitted signal yield suggest that this analysis does not yet have enough sensitivity to definitively determine the branching fraction. Therefore, a limit will be set on the branching fraction using the fitted signal yield. The method used to set the limit, the *CLs Method*, is a modified frequentist statistical approach which has been developed at CERN for use in the Higgs search [41]. It is well suited for use in the search for a rare process, and takes full advantage of the shape information in the signal and background PDFs to set the limit.

In the following sections, the limit setting procedure and its stability are outlined.

7.1 The CLs Method

The "CLs Method" was developed at CERN for the purpose of setting improved limits on the Higgs mass limit. It is a *modified frequentist approach* that uses an estimator, Q, to construct a confidence level for a given signal hypothesis s (denoted $CL_s(Q_{data})$) given the background expectation, b,

$$CL_s(Q_{data}) \equiv \frac{P(Q_{s+b} < Q_{data})}{P(Q_b < Q_{data})} \tag{7.1}$$

where Q_{data} is the value of the estimator in the data set, Q_{s+b} (Q_b) is the value of the estimator for a given signal and background (background only) hypothesis. The probability that Q_{s+b} is less than Q_{data} for the given hypothesis is denoted $P(Q_{s+b} < Q_{data})$.

The method employs large ensembles of *toy Monte Carlo* for each hypothesis; a toy Monte Carlo is a simulation of an experiment obtained by sampling the likelihood function repeatedly for each hypothesis. This exercise yields a large number of "data" sets, each derived from the likelihood function, which are then used to calculate the confidence level for the hypothesis.

The fitted signal yield, denoted μ_s^{fitted}, is used as the estimator. For each signal hypothesis, μ_s^{hyp}, 5000 toy Monte Carlo data sets are generated, each with the expected background (123.94). A scan is performed over signal hypotheses from $\mu_s^{hyp} = 0$ to $\mu_s^{hyp} = 100$ in steps of 0.2. Each data set in the ensemble is fit with the likelihood function and the distribution of the fitted signal yield for that hypothesis is obtained. The distributions of μ_s^{90} for $\mu_s^{hyp} = 0.0$ and $\mu_s^{hyp} = 4.0$ are shown in Fig. 7.1.

For each hypothesis the confidence level (defined in Equation 7.1) of a particular fitted signal yield is determined as follows,

$$CL(\mu_s^{hyp}, \mu_s^{fitted}) \equiv \frac{\int_{-\infty}^{\mu_s^{fitted}} D_{s+b}(\mu_s'; \mu_s^{hyp}) d\mu_s'}{\int_{-\infty}^{\mu_s^{fitted}} D_b(\mu_s') d\mu_s'}, \tag{7.2}$$

where μ_s' is the fitted signal yield for a given experiment in the toy Monte Carlo ensemble and $D_{s+b}(\mu_s'; \mu_s^{expected})$ ($D_b(\mu_s')$) is the normalized fitted signal yield distribution for the signal hypothesis (null signal hypothesis). Using this formula either of two steps can then be taken to then find the limit on the signal yield at a particular confidence level:

1. Use the value of μ_s^{fitted} obtained from data, or from a test experiment derived from GEANT4 Monte Carlo, and generate a curve relating confidence level and the signal hypothesis.

2. Make the requirement that $CL(\mu_s^{hyp}, \mu_s^{90}) = 1 - 0.90$ and find the point $\mu_s^{fitted} = \mu_s^{90}$ that satisfies this constraint for each signal hypothesis. This generates a relationship between any given fitted signal yield and the 90% confidence limit on the signal content of the data set.

The curve generated from the requirement in the second option is illustrated in Fig. 7.2. Such curves will be used in following sections not only to evaluate systematic effects from possible modifications to the PDFs, but also to obtain the final limit on the signal yield, and thus the branching fraction, in the data. These two options are different methods of using Equation 7.2 to obtain the same confidence limit on the signal yield in a given data set.

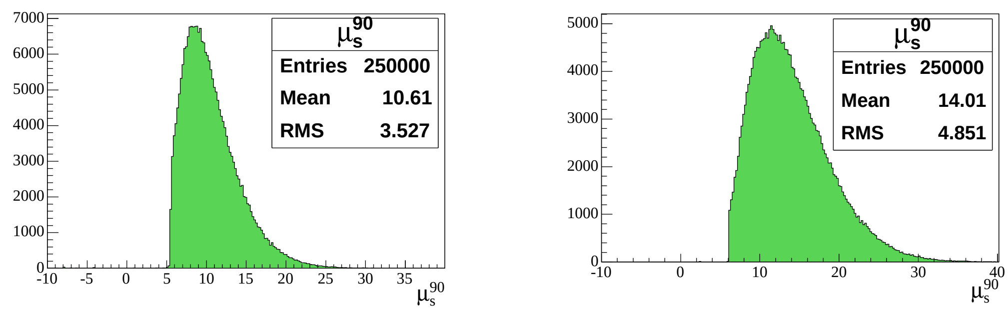

(a) $\mu_s^{hyp} = 0$ (b) $\mu_s^{hyp} = 4$

Figure 7.1: The distribution of μ_s^{90} for the null signal hypothesis (left) and for $\mu_s^{hyp} = 4$ (right), which corresponds to a branching fraction hypothesis of $\mathcal{B}(B^+ \to \tau^+\nu_\tau) = 1.0 \times 10^{-4}$.

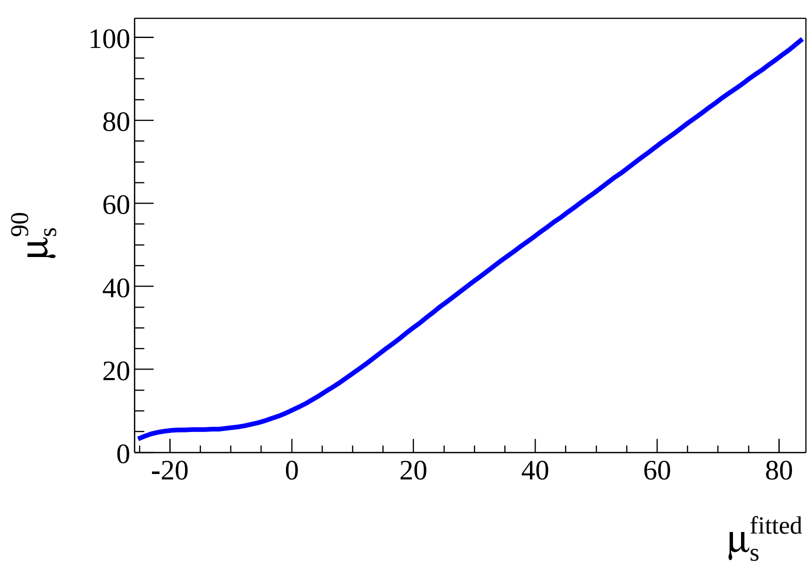

Figure 7.2: The progression of μ_s^{90} is shown as a function of the fitted signal yield (μ_s^{fitted}). This curve is derived from 500 different signal hypotheses between 0.0 and 100.0. Each ensemble of toy MC contains 5000 experiments. The curve is obtained by fitting a polynomial to the resulting points.

7.2 Expected Sensitivity to the Branching Fraction

The CLs method outlined in the previous section is used to determine our nominal sensitivity to the signal content of the data and thus the branching fraction. To do this the likelihood function is used to fit 5000 toy Monte Carlo data sets, each generated using the null signal hypothesis. From this a distribution of the fitted signal yield is obtained, which can then be mapped to a distribution of the 90% confidence limit on the signal yield for this hypothesis. Such a mapping is obtained by applying the curve in Fig. 7.2 to the fitted signal yield from each experiment. The distribution of μ_s^{90} is shown in Fig. 7.3.

The nominal expectation for the limit on the signal yield is defined as the median of the distribution in Fig. 7.3. This point lies at 9.96 signal events. Using the signal efficiency as derived from signal Monte Carlo ($(4.77 \pm 0.35) \times 10^{-4}$) and the number of B^+ mesons collected by BaBar (88.9×10^6) the following branching fraction limit is expected in the absence of signal:

$$\mathcal{B}(B^+ \to \tau^+ \nu_\tau) < 2.3 \times 10^{-4} \text{ at the 90\% confidence level} \quad (7.3)$$

7.3 The Stability of the Limit Setting Procedure

The stability of the limit setting procedure is now explored. A possible weakness of the method is the use of the Monte Carlo simulations of signal and background to derive the forms of the PDFs. It is possible for the data to contain features in the E_{extra} spectrum which are not modeled correctly in the simulation and which resemble features of the signal.

This possibility and its effects are examined as follows:

1. Variations in the background expectation will be explored.

2. Several different choices of background parameterization will be explored.

3. Several control samples will be developed with methods similar to those used to develop the signal sample, but which contain little or no signal (Section 7.3.3).

   - differences in these controls samples in data and Monte Carlo will be used to correct to the nominal PDFs (Section 7.3.4).

   - The corrected PDFs will be used to generate toy Monte Carlo data sets and then fit them with the nominal model. The variation in the limit due to a change in the generator model will be used to determine if assumptions about the E_{extra} spectrum are conservative. (Section 7.3.7).

4. Finally, variation in the signal model will be explored.

7.3.1 Variation in the Limit with Background Expectation

Although the agreement between the background predictions from simulation and data (Section 5.9.2) is excellent, the central values are not in perfect agreement. Therefore, the effect of a variation of the limit with background expectation is explored. For a number of possible background expectations, a limit-setting curve is developed. The curves are compared in Fig. 7.4.

The variation between the curves is not significant, amounting to a less than one event variation around the nominal limit-setting curve. Therefore, the conclusion is that this method is stable against fluctuations in the background expectation.

7.3.2 Variation in Background Parameterization

The choice of background parameterization is explored as a possible source of instability in the limit-setting procedure. Several models are substituted when generating toy Monte Carlo for the procedure, while the fit is always performed with the nominal sample. The other models which are pursued are illustrated in Fig. 5.17: a Gaussian, a KEYS PDF, and a 50-bin histogram. The 3rd-order polynomial is the nominal choice for the background model. Limit-setting curves are obtained from generating with these other models and fitting with the nominal model. The curves are applied to the `GEANT` experiments to determine the variation in the upper limit, shown in Table 7.1.

The change in the limit which can be set is observed to be small compared to the variation in the upper limit fo the null signal hypothesis. In addition, the nominal background model choice is more conservative than others. Therefore, based on these observations the 3rd-order polynomial is maintained as the nominal model.

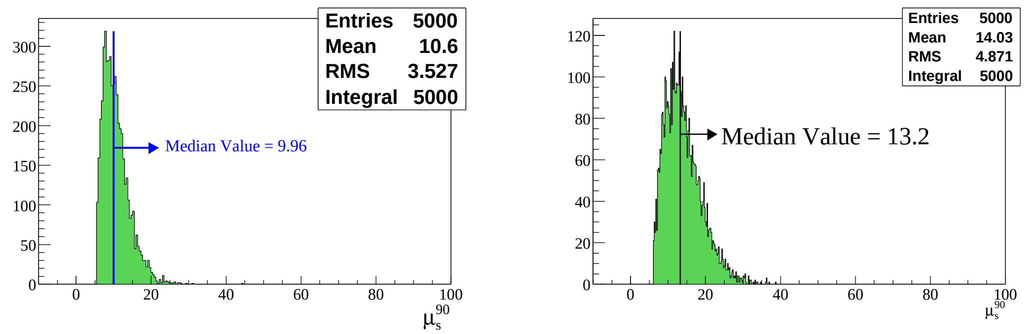

(a) The upper limit variation for the null signal hypothesis.

(b) The upper limit variation for a signal hypothesis of 4.2 events.

Figure 7.3: The upper limit variation for the null signal hypothesis and for the Standard Model signal hypothesis, given the nominal efficiency. The median is taken as the nominal expectation for the upper limit.

Table 7.1: The variation in the limits in the `GEANT` experiments is observed as the toy Monte Carlo generator model is varied for the background shape.

Background Shape	μ_s^{90} Result for `GEANT` MC (first)	μ_s^{90} Result for `GEANT` MC (second)
3rd-order Polynomial	13.5	10.3
Gaussian	13.6	10.4
KEYS	13.6	10.4
50-bin Histogram	13.6	10.4

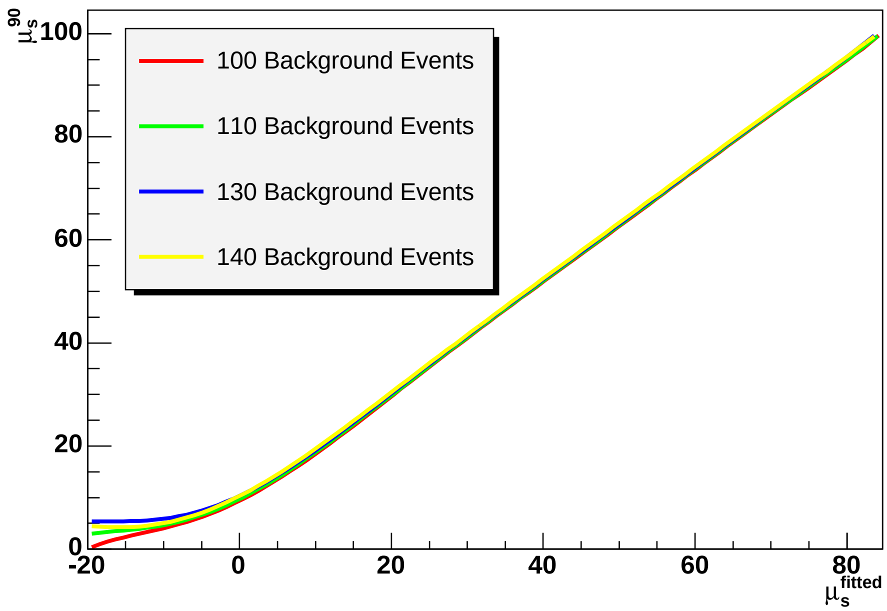

Figure 7.4: The variation of the limit-setting curve is explored as the background expectation changes from that expected with the nominal background model in the data (123.94 events). The change in the curve is small. For the nominal expectation of $\mu_s^{fitted} = 0.0$ assuming there are actually 0.0 signal events in the data, the curve corresponding to 123.94 ± 6.90 expected background events yields $\mu_s^{90} = 9.96$. For a fluctuation of ± 20 background events this amounts to a variation of the value of μ_s^{90} of less than one event.

7.3.3 Control Samples for Systematic Studies

Three control samples are defined for use in the study of the stability of the limit setting procedure as follows:

1. "$B^- \to D^0\ell^-\nu X + B^+ \to Y^+$": one B meson is reconstructed as $B^- \to D^0\ell^-\overline{\nu}_\ell X$ and no restrictions are placed on the recoil of the event. While this sample can potentially contain $B^+ \to \tau^+\nu_\tau$ in the recoil, it contains an

overwhelming amount of background and is useful for studying systematic differences in the E_{extra} spectrum early in the selection criteria.

2. **"$B^- \to D^0\ell^-\overline{\nu}_\ell X$ + two tracks"**: This sample retains the semi-leptonic B-meson but constrains the recoil to possess two tracks. One of the two tracks must then pass all the requirements which are normally placed on the single, signal-side track. All other selection criteria remain the same except that the net charge requirement is changed from $\sum_i q_i = 0$ to $|\sum_i q_i| = 1$.

3. **"$\overline{B}^0 \to D^{*+}\ell^-\nu$ + one remaining track"**: This sample most closely mimics the topology of the signal sample, with one B reconstructed as a neutral semi-leptonic decay and the rest of the event required to contain only one track. This sample contains no signal but can be treated by the analysis selection criteria exactly as signal. The only difference in the selection is the requirement that $|\sum_i q_i| = 1$

The control samples are constructed in background Monte Carlo and in data. In the following sections, comparisons are made for the neutral energy distributions in each sample between data and Monte Carlo.

7.3.3.1 Neutral Energy in $B^- \to D^0\ell^-\nu X\ +\ B^+ \to Y^+$

The neutral energy shape, compared between data and MC, is illustrated in Fig. 7.5a. The distribution is then fitted using a 6th-order polynomial in both data and MC (Fig. 7.5b and Fig. 7.5c, respectively). The ratio of the two functions (Fig. 7.5d) is then taken and will be used to correct the nominal background PDF. The error bars in Fig. 7.5d are derived from the errors in the data and MC histograms, and are therefore uncorrelated. This is a high statistics sample and suggests that a disagreement in the zero energy bin can be expected. The effect of such a disagreement on the stability of the limit is explored below.

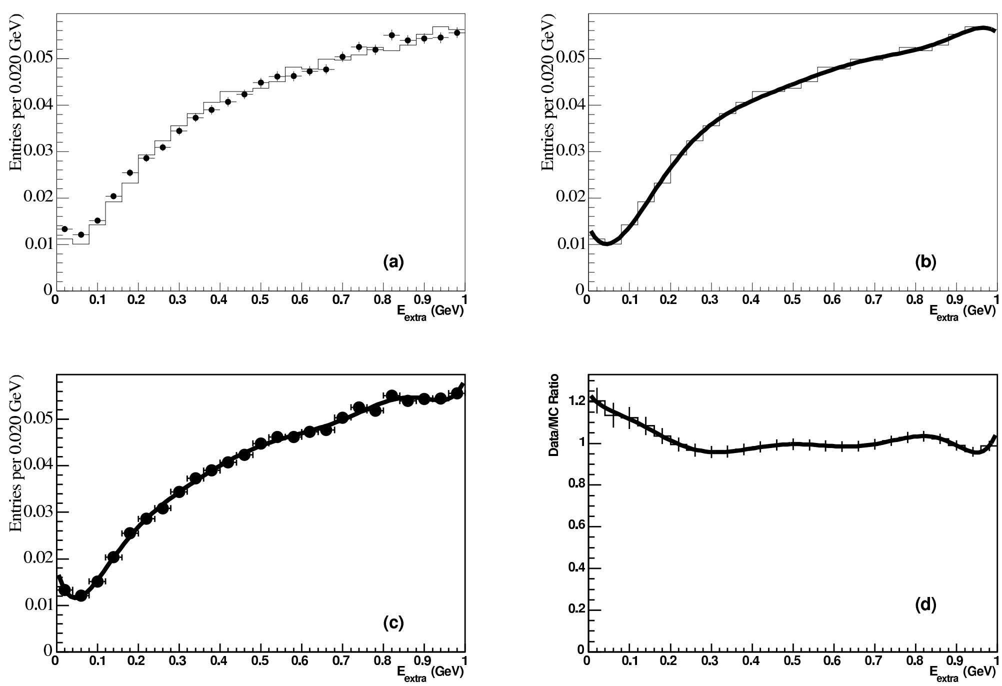

Figure 7.5: The data and MC from the $D\ell\nu X+Y$ control sample. The (a) neutral energy in MC and (b) neutral energy in data exhibit (c) reasonable agreement in the shape of the energy. Polynomials are fit to each distribution and the (d) ratio of the polynomials is taken bin-by-bin to derive a scaling function for the background PDF. The error in each bin of the ratio is determined from the errors in the data and MC histogram bins.

7.3.3.2 Neutral Energy in $B^- \rightarrow D^0\ell^-\overline{\nu}_\ell X$ + two tracks

The neutral energy shape, compared between data and MC, is illustrated in Fig. 7.6a. The distribution is then fitted using a 6th-order polynomial in both data and MC (Fig. 7.6b and Fig. 7.6c, respectively). The ratio of the two functions (Fig. 7.6d) is then taken and will be used to correct the nominal background PDF. The error bars in Fig. 7.6d are derived from the errors in the data and MC histograms, and are therefore uncorrelated. This is a low statistics sample and no significant disagreement is suggested.

7.3.3.3 Neutral Energy in $\overline{B}^0 \rightarrow D^{*+}\ell^-\nu$ + one remaining track

The data and MC from the $D\ell\nu X$ + two remaining track control sample. The neutral energy shape, compared between data and MC, is illustrated in Fig. 7.7a. The distribution is then fitted using a 6th-order polynomial in both data and MC (Fig. 7.7b and Fig. 7.7c, respectively). The ratio of the two functions (Fig. 7.7d) is then taken and will be used to correct the nominal background PDF. The error bars in Fig. 7.7d are derived from the errors in the data and MC histograms, and are therefore uncorrelated. This is a low statistics sample; taken literally, it suggests a large disagreement might exist in the zero-energy region.

7.3.4 Corrections to the PDF Shapes

The difference between the E_{extra} shape in data and MC is used as a correction function for the background PDF. The correction from the highest statistics sample, $B^- \rightarrow D^0\ell^-\nu X + B^+ \rightarrow Y^+$, suggests that a small difference in the

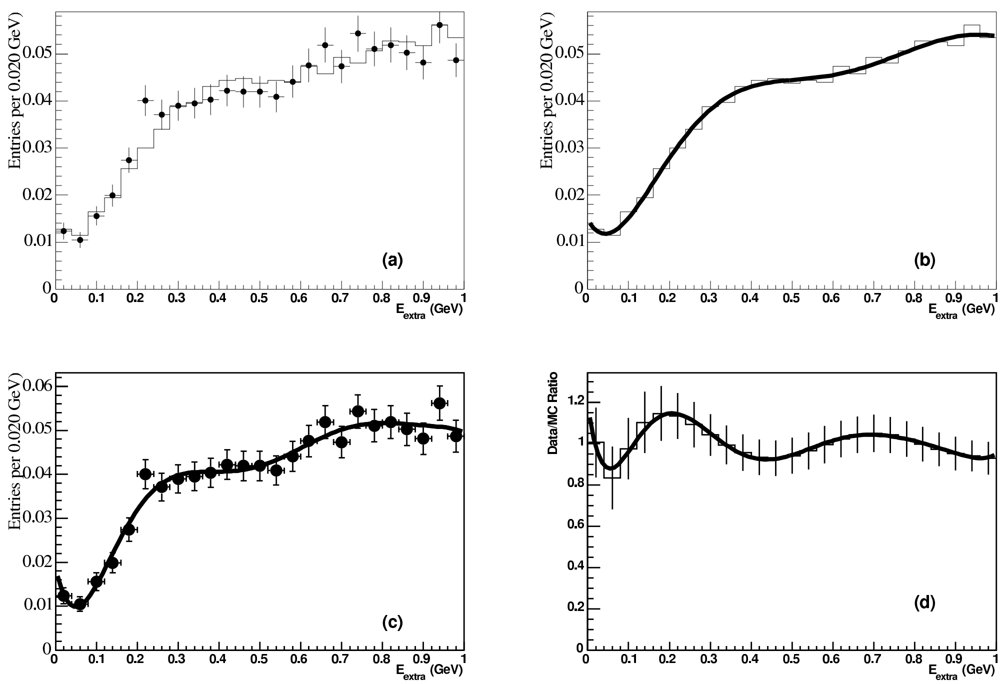

Figure 7.6: The (a) neutral energy in MC and (b) neutral energy in data exhibit (c) reasonable agreement in the shape of the energy. Polynomials are fit to each distribution and the (d) ratio of the polynomials is taken bin-by-bin to derive a scaling function for the background PDF. The error in each bin of the ratio is determined from the errors in the data and MC histogram bins.

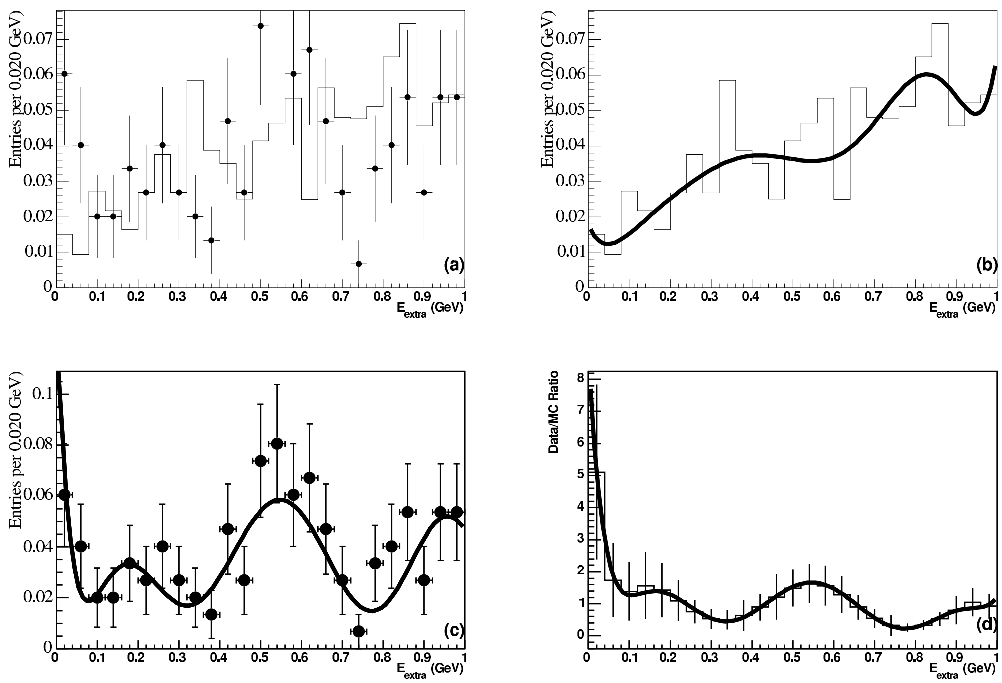

Figure 7.7: The data and MC from the $D^{*+}\ell\nu + 1$ remaining track control sample. The (a) neutral energy in MC and (b) neutral energy in data exhibit (c) reasonable agreement in the shape of the energy. Polynomials are fit to each distribution and the (d) ratio of the polynomials is taken bin-by-bin to derive a scaling function for the background PDF. The error in each bin of the ratio is determined from the errors in the data and MC histogram bins.

Table 7.2: The 90% confidence level limit on the signal yield in the GEANT4, background-only experiments and its variation with the smearing of the background PDF. The smearing is motivated from several control samples

Background PDF Correction Model	90% CL Limit on the Signal Yield GEANT4 Sample 1	GEANT4 Sample 2
None	13.5	10.3
$D\ell\nu X + Y$	12.9	10.0
$D\ell\nu X$ + two tracks	12.6	9.7
$D^{*+}\ell\nu$ + one track	8.2	7.2

neutral energy at zero is expected. The other two samples, with larger statistical uncertainties, suggest the correction could be as high as a factor of two.

The corrected background PDFs are used in conjunction with the nominal signal PDF to generate toy MC for the usual range of signal hypotheses. The toy MC samples are fit using the nominal background and signal PDFs. This allows for an estimate of the change in the limit if nature generates the neutral energy according to a model different from the nominal model. Observing the change in the limit allows us to determine how conservative our nominal background model is.

The results are detailed in Table 7.2.

7.3.5 Variation of the Limit with Changes to the Signal PDF

The double-tag control sample (section 5.7.1) suggests a possible variation in the position of the Gaussian mean used to make the signal PDF. The effect of such a variation on the expected μ_s^{90} result is explored by generating toy Monte

Carlo with the Gaussian mean shifted by $\pm 15\,\mathrm{MeV}$ but fitting with the nominal likelihood function. The results of this variation (table 7.3) suggest that the shift hinted at by the control sample affects the μ_s^{90} expectation at the 3% level, which is not a significant effect. Such a variation would not significantly affect the upper limit expectation.

Table 7.3: The double-tag control sample suggests that we may expect a shift in the mean of the peak from D^{*0} decays at the level of $15\,\mathrm{MeV}$. The effect of this shift is explored by generating toy MC with the shifted gaussian mean in the signal PDF and fitting the experiments with the nominal likelihood function. The change is the upper limit expectation on the signal yield is shown below.

Signal PDF Gaussian Mean Shift (MeV)	μ_s^{90} Result for `GEANT` MC (first)	μ_s^{90} Result for `GEANT` MC (second)
0.0	13.5	10.3
+15.0	13.6	10.3
−15.0	13.5	10.3

7.3.6 Variation in the Limit with Enhancement at $E_{extra} = 0$

Another potential effect may arise from systematic differences between the data and simulation in the background E_{extra} distribution; this effect is illustrated in two of the control samples used to scale the background PDF (Fig. 7.5 and Fig. 7.7). The concern is that such an enhancement in pure background might mimic signal.

To observe the effect of such an enhancement, toy MC is generated using a the nominal background model *scaled* with a factor of 2.0 (5.0) enhancement in the region $E_{extra} < 0.020\,\mathrm{GeV}$. This scaling is at the level of the discrepancy observed in the $B^- \to D^0\ell^-\nu X\ +\ B^+ \to Y^+$ ($\overline{B}^0 \to D^{*+}\ell^-\nu$ + one remaining track) control sample.

A confidence limit curve is generated by fitting the toy MC with the nominal likelihood function. The curve is used on the `GEANT` MC experiments to observe the change in μ_s^{90}. The results are given in table 7.4. Since such an increase in the zero-bin feature results in a less conservative result, the nominal background PDF is selected for use in the final fit.

Table 7.4: The effect of an enhanced zero-bin in the E_{extra} spectrum is examined by generating a confidence limit curve from toy MC with an enhanced zero-bin and fitting with the nominal model. The results suggest that including an enhancement in the background at zero would lead to a less conservative result.

Zero-Bin Enhancement Factor	μ_s^{90} Result for `GEANT` MC (first)	μ_s^{90} Result for `GEANT` MC (second)
1.0	13.5	10.3
2.0	13.0	10.0
5.0	11.8	9.4

7.3.7 Stability of the Sensitivity

The results of the studies from the previous sections are summarized here. After exploring a number of possible differences between the expected E_{extra} features (shape, overall yield of events, etc.) and possibilities in data, the nominal expectation for the background yield and shape are determined to be relatively stable. In cases where the background is made to contain "signal-like" features, the limit that can be set becomes less conservative. Again, this determines that the nominal choices for the limit setting procedure lead to a more conservative limit than many other choices. Therefore, this analysis continues with background and signal parameterizations determined in sections 5.7 and 5.8.

7.4 Incorporation of Systematic Uncertainties into the Limit Setting Procedure

The 9.9% combined systematic and statistical uncertainty determined in chapter 6 needs to be incorporated into the limit setting procedure. In addition, the procedure needs to include the uncertainty on the count of B^+ mesons in the *BABAR* data set (a 1.1% uncertainty). In the procedure outlined in section 7.1, 5000 toy Monte Carlo experiments were generated for each signal hypothesis. If there is no uncertainty in the signal efficiency or B-meson count, then the relationship between a signal hypothesis and a branching fraction is clear:

$$\mathcal{B}(B^+ \to \tau^+\nu_\tau) = \frac{N_{sig}}{N_{B^+} \cdot \varepsilon_{signal}}. \tag{7.4}$$

However, since the efficiency and N_{B^+} have uncertainty, the relationship to the branching fraction is not direct. This uncertainty is incorporated into the limit-setting procedure as follows:

- Instead of generated toy Monte Carlo from a fixed number of events, the number is generated from a branching fraction hypothesis, $\mathcal{B}(B^+ \to \tau^+\nu_\tau)_i$.
- For each of the 5000 toy Monte Carlo experiments generated from this branching fraction hypothesis, the corresponding signal hypothesis is determined by sampling from a Gaussian. Therefore, for the i^{th} branching fraction hypothesis, the signal hypothesis for the j^{th} experiment is defined

by $N^j_{sig,i} = \mathcal{B}(B^+ \to \tau^+\nu_\tau)_i \times \mathcal{G}(\varepsilon_{signal} \cdot N_{B^+}; \Delta(\varepsilon_{signal} \cdot N_{B^+}))$. The Gaussian is centered on the product of the efficiency and the B-meson count and has a width defined by the uncertainty on this product.

- For each signal hypothesis and for the total expected number of background events, toy Monte Carlo is generated from the likelihood function and the neutral energy so generated is fit using the function to extract the signal and background yields.

- The above is repeated for each branching ratio hypothesis to establish a relationship between the fitted signal yield and the 90% confidence level limit on the branching fraction hypothesis.

The relationship between the fitted signal yield and the 90% confidence level limit on the branching fraction hypothesis is illustrated in Fig. 7.8 and compared to the curve which does not have the systematics included. After including systematics into the limit setting procedure, the expected sensitivity to the upper limit is as follows:

$$\mathcal{B}(B^+ \to \tau^+\nu_\tau) < 2.7 \times 10^{-4} \text{ at the 90\% confidence level (expected).} \tag{7.5}$$

7.5 The Branching Fraction Limit for $B^+ \to \tau^+\nu_\tau$

The fit to the data set (Section 5.10) gave the fitted signal yield in the data set ($\mu_s^{fitted} = 14.8 \pm 6.3$). Using this signal yield and the limit setting curve (without including the efficiency systematics) in Fig.7.8, the 90% confidence level

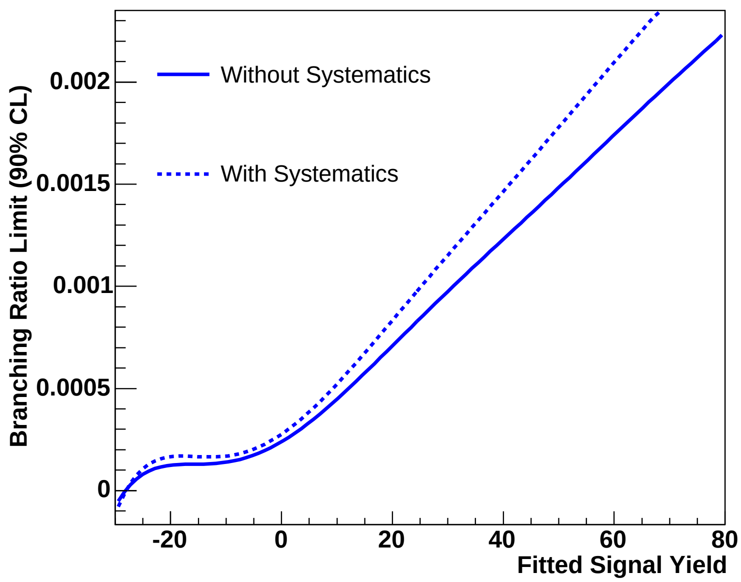

Figure 7.8: Shown is the relationship between μ_s^{fitted} and the branching ratio limit at the 90% CL when systematic uncertainty is and is not included in the upper limit calculation.

limit on the signal content of the data is determined to be

$$\mu_s^{90} = 24.2. \tag{7.6}$$

Inserting this into the branching fraction limit equation yields the limit on the branching fraction:

$$\mathcal{B}(B^+ \to \tau^+ \nu_\tau) < 5.7 \times 10^{-4} \text{ at the 90\% confidence level.} \tag{7.7}$$

After including systematic uncertainty in the limit, the result becomes:

$$\mathcal{B}(B^+ \to \tau^+ \nu_\tau) < 6.7 \times 10^{-4} \text{ at the 90\% confidence level.} \tag{7.8}$$

These results include the systematic correction to the branching fraction and its uncertainty. The limit obtained here is less strict than that obtained by the L3 collaboration, which has the strictest published limit obtained to date on this process. This suggests one (or both) of two possibilities:

- There is a signal in the sample which is contributing to the neutral energy. However, due to the statistical uncertainty it cannot be clearly resolved.
- There is a statistical fluctuation in the background, and/or a contribution to the neutral energy shape from background which is unmodeled.

Chapter 8

Results

8.1 Results on the Data Set

As determined in Chapter 7, section 7.5, the limit on the branching fraction obtained in this analysis using $81.9\,\mathrm{fb}^{-1}$ of *BABAR* data is

$$\mathcal{B}(B^+ \to \tau^+\nu_\tau) < 6.7 \times 10^{-4} \text{ at the 90\% confidence level.} \tag{8.1}$$

This limit is less stringent than the most stringent published limit, $\mathcal{B}(B^+ \to \tau^+\nu_\tau) < 6.7 \times 10^{-4}$ at the 90% confidence level obtained by the L3 collaboration. As outlined in 7.5, the difference between the expected limit (2.7×10^{-4}) and this result in the data could be due to real signal present in the data or a fluctuation or unsimulated feature of the background. Currently, this analysis is limited by the data set size. Since 2002, *BABAR* has collected another $50\,\mathrm{fb}^{-1}$ which in the future can be used to reduce the statistical uncertainty on the conclusions of this work.

8.2 Outlook for the Search for $B^+ \to \tau^+\nu_\tau$

In the present work, the sensitivity of the analysis is limited by the available data. The B-factories, both *BABAR* and Belle, are continuing to accumulate large numbers of B mesons. By the end of 2004 the available *BABAR* data set will be sufficient to put the sensitivity of this analysis within reach of the Standard Model (see Table 8.1. By 2006, *BABAR* will have accumulated $500\,\mathrm{fb}^{-1}$ of data and this analysis will be sensitive to the central value of the Standard Model prediction. The numbers in Table 8.1 assume that no improvements are made to the signal efficiency, so the estimates are conservative. With the current analysis, the expected number of signal events in 2006 (23 events) corresponds to a 3σ (statistical) difference from the background-only hypothesis.

At the present time, *BABAR* pursues two statistically independent searches for $B^+ \to \tau^+\nu_\tau$. The present work documents one of the techniques, while the second approach reconstructs the tag B in purely hadronic final states. The result from the search using hadronic tags yields a limit of $\mathcal{B}(B^+ \to \tau^+\nu_\tau) < 4.2 \times 10^{-4}$ using the same data sample as the present analysis (data from 1999-2002). The expected limit from the hadronic tag method is $\mathcal{B}(B^+ \to \tau^+\nu_\tau) < 3.3 \times 10^{-4}$, which is higher than that from the present work. The combined limit from these two analyses is driven by the hadronic tag analysis, since their result was closer their background expectation than that of the present work.

The Belle experiment has yet to announce any results from a search for $B^+ \to \tau^+\nu_\tau$. Since Belle and *BABAR* are highly complementary experiments,

Table 8.1: The current and projected sensitivities to the upper limit on the branching fraction. The expected upper limit is calculated using the assumption that no signal is observed. The expected limit and the Standard Model prediction both assume that the signal efficiency of this analysis remains unchanged througout the lifetime of *BABAR*.

Period	Luminosity (fb^{-1})	Expected Upper Limit ($\times 10^{-4}$)	Standard Model Signal Prediction (Events)
1999-2002	81.9	2.3	4
1999-2004	200	1.5	9
1999-2006	500	0.93	23

results from such a search at Belle could also be combined with results from *BABAR* to further enhance the sensitivity to the branching fraction.

Given the expected sensitivity increase of this analysis and the external factors mentioned above (other *BABAR* searches, Belle), it is likely that this process will be discovered within the next three years. The results in this work already seem to hint that there is something extremely interesting occurring in the data with the current selection criteria. While this difference from the background-only expectation could be a combination of both a signal and a background source (or a very particular background), this analysis will continue to test not only the limits of the *BABAR* detector but also the limits of the Standard Model of Particle Physics.

Bibliography

[1] S. L. Glashow. *Nucl. Phys.* **A22**, page 579, 1961.

[2] S. Weinberg. *Phys. Rev. Lett.* **19**, page 1264, 1967.

[3] A. Salam. *Elementary Particle Theory.* 1968.

[4] K. Hagiwara et al. Review of Particle Physics. *Physical Review D*, 66:010001+, 2002.

[5] N. Cabibbo. *Phys. Rev. Lett.* **10**, 1963.

[6] M. Kobayashi and T. Maskawa. *Prog. Theor. Phys.* **42**, 1973.

[7] L. Wolfenstein. *Phys. Rev. Lett.* **51**, 1983.

[8] D. Buskulic et al. *Phys. Lett.* **B 343**, page 444, 1995.

[9] P. Abreu et al. *Phys. Lett.* **B 496**, page 43, 2000.

[10] T. E. Browder et al. *Phys. Rev. Lett.* **86**, page 2950, 2001.

[11] M. Acciarri et al. *Phys. Lett.* **B 396**, page 327, 1997.

[12] B. Aubert et al. A study of time-dependent CP-violating asymmetries and flavor oscillations in neutral B decays at the Upsilon(4S). *Phys. Rev.* **D 66**, 2002.

[13] T. Tomura et al. Measurement of the Oscillation Frequency for B0-B0bar Mixing using Hadronic B0 Decays. *Phys. Lett.* **B 542**, 2002.

[14] Matthias Jamin A. J. Buras and Peter H. Weisz. Leading and next-to-leading QCD corrections to ε-parameter and $B\overline{B}$ mixing in the presence of a heavy top quark. *Nucl. Phys.* **B347**, 1990.

[15] Andrzej J. Buras. Flavour dynamics: Cp violation and rare decays. 2001.

[16] W. S. Hou. *Phys. Rev. D* **48**, 1993.

[17] G. Kane. *Perspectives on Supersymmetry.* 1998.

[18] B. Aubert *et al.* The BABAR detector. *Nucl. Instr. and Methods* **A479**, 2002.

[19] PEP-II - An Asymmetric B Factory, Conceptual Design Report, 1993.

[20] F. Sauli. Priciples of operation of multiwire proportional and drift chambers. *CERN-77-09*, 1977.

[21] Plastic Streamer Tubes and Their Applications in High-Energy Physics. *Nucl. Instr. and Methods A* **217**, 1983.

[22] S. Spanier. *BABAR Analysis Document 116, Kaon Selection at BABAR*, 2000.

[23] A. Drescher. *Nucl. Instr. and Methods* **A391**, page 464, 1985.

[24] R. Sinkus and T. Voss. *Nucl. Instr. and Methods* **A391**, page 360, 1997.

[25] The *BABAR* Simulation Production Group. *Generating Monte Carlo Events with* `GenFwkInt`. http://www.slac.stanford.edu/BFROOT/www/Physics/Tools/generators/GenFwkInt/GenFwkInt.html.

[26] The *BABAR* Simulation Production Group. *BOGUS: BABAR Object-oriented Geant4-based Unified Simulation.* http://www.slac.stanford.edu/BFROOT/www/Computing/Offline/Simulation/web/bogus-guide.html.

[27] S.Agostinelli *et al.* Geant4 - a simulation toolkit. *SLAC-PUB-9350*. Submitted to Nucl. Instr. Meth. A.

[28] P. F. Harrison and H. R. Quinn [BABAR Collaboration]. *The BaBar physics book: Physics at an asymmetric B factory.* 1998. SLAC-R-0504.

[29] B. Aubert et al. A Search for $B^+ \to \tau^+\nu$ Recoiling Against a Fully Reconstructed B. *hep-ex/0304030*, 2003.

[30] P. Jackson. *BABAR Analysis Document 537, Tagging using* $B \to D\ell\nu X$ *decays*, 2003.

[31] C. Touramanis et al. *BABAR Analysis Document 20, Reconstruction of* π^0 *in BABAR*, 2000.

[32] G. C. Fox and S. Wolfram. *Phys. Rev. Lett.* **41**, 1978.

[33] G. Blaylock and K. Flood. *BABAR Analysis Document 305, Thrust Calculation at BABAR*, 2001.

[34] B. Aubert et al. Measurement of the Inclusive Charmless Semi-Leptonic Branching Ratio of B Mesons and Determination of $|V_{ub}|$. *hep-ex/0307062*, 2003.

[35] G. J. Feldman and R. D. Cousins. *Phys. Rev.* **D 57**, 1998.

[36] C. Cheng, Stanford University. *A Measurement of the Lifetime and Mixing Frequency of neutral B mesons with semileptonic decays in the BABAR Detector*, 2002.

[37] K.S. Cranmer. Kernel estimation in high-energy physics. *Comput. Phys. Commun.*, 136:198–207, 2001.

[38] D.E. Groom et al. Review of Particle Physics. *The European Physical Journal*, C15:1+, 2000.

[39] F. Bellini, S. Brunet, and F. Di Lodovico. *BABAR Analysis Document 378, Comparison between Monte Carlo and Data of the pi0 detection and reconstruction efficiency using tau 1-on-1 decays*, 2003.

[40] M. Bona, G. Cavoto, C. Dallapiccola, S. Grancagnolo, E. Varnes, S. R. Wagner, and L.Zhang. *Report of the Tracking Efficiency Task Force*, 2002.

[41] A. L. Read. Modified frequentist analysis of search results (the CL_s method). *CERN-OPEN-2000-205*, 2000.

Appendix A

Data/Monte Carlo Agreement and Four-Fermion Events

Very early in the analysis, after building lists of $D\ell$ candidates but before event refinement begins (see Section 4.5) there are disagreements between data and Monte Carlo simulations. The discrepancy is most apparent in comparing the off-peak data with the continuum Monte Carlo ($e^+e^- \to u\overline{u}, d\overline{d}, c\overline{c}, s\overline{s}, \tau^+\tau^-$). The disrepancy between data and simulation exists at large R_2^{all} (Fig. A.1) and low missing mass (Fig. A.2). The data has typically a different shape than simulation, manifesting as an under-prediction of the yield by the Monte Carlo.

The disagreement was determined to be most prominent in events with exactly four charged tracks. The tracks were either all electrons or were a pair of electrons and a pair of pions. The distributions of R_2^{all} and missing mass for the case where there are four charged tracks (with either electrons or electrons and pions) and when there are not four tracks are shown in Fig. A.3 and A.4.

The remaining disagreement in the missing mass (Fig. A.4) is a shift in the

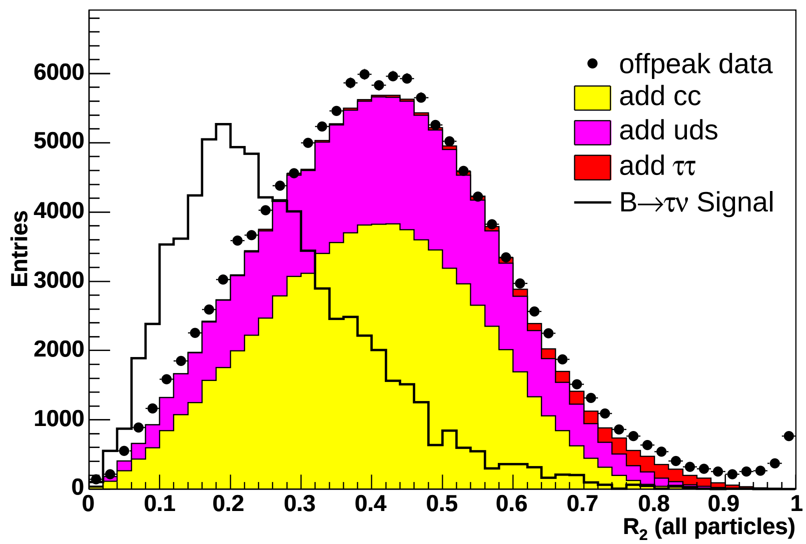

Figure A.1: The ratio of the second to the zeroth Fox-Wolfram moment calculated using all charged tracks and neutrals, denoted R_2^{all}. The offpeak data (dots) and continuum Monte Carlo (solid histograms) are used to make the comparison. The signal Monte Carlo is also shown (white histogram). The data disagrees with the Monte Carlo above 0.9.

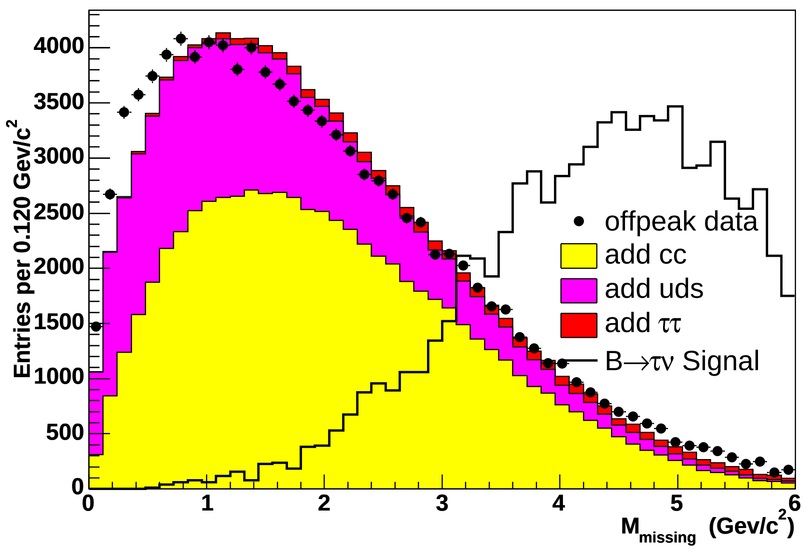

Figure A.2: The missing mass. The offpeak data (dots) and continuum Monte Carlo (solid histograms) are used to make the comparison. The signal Monte Carlo is also shown (white histogram). The data disagrees with the continuum Monte Carlo below 1.0 GeV/c^2.

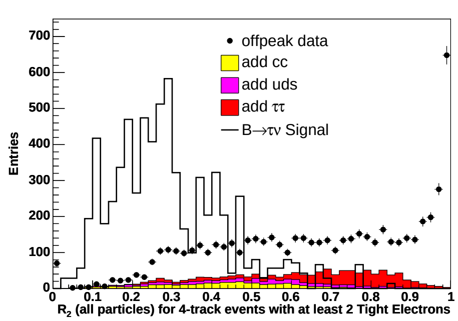

(a) Events with four tracks which are either electrons or electrons and pions

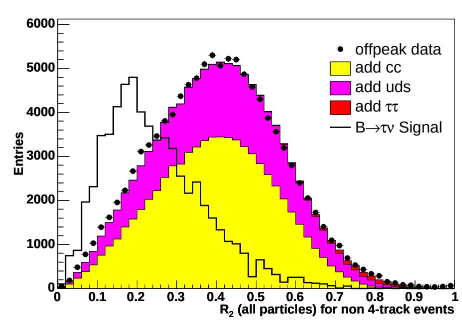

(b) Events with any number of tracks except four

Figure A.3: A comparison of R_2^{all} for events with four tracks (identified either as electrons or electrons and pions, left) and events with any number of tracks except four (right). The disagreement between offpeak data (dots) and continuum Monte Carlo (solid histogram) exists in the four-track events.

distribution, but the overall shape agrees very well after removing the events with four well-identified electrons or electrons and pions.

These events are most likely due to four-fermion processes. The Feynman diagram for this process is shown in Fig. A.5. These events are explicitly un-simulated in the *BABAR* Monte Carlo because of the difficultly in simulating their cross-section for very low momentum transfers. Given the information above, the following restrictions are placed on the data (and Monte Carlo) to remove these events:

$$R_2^{all} < 0.9 \text{ and } M_{missing} > 1.0\,\mathrm{GeV/c^2}. \tag{A.1}$$

These cuts preserve all the signal while removing the disagreement between data and Monte Carlo. This disagreement is also removed automatically by the restic-tions on the $D\ell$ candidate. However, the above cuts are used to remove the disagreement at a very early stage of the analysis.

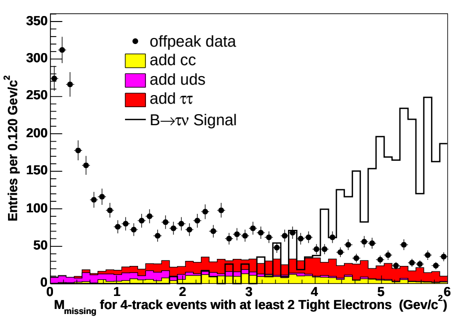

(a) Events with four tracks which are either electrons or electrons and pions

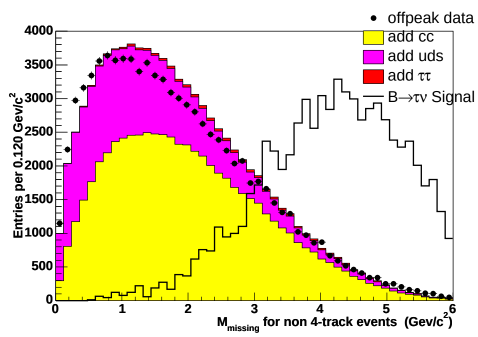

(b) Events with any number of tracks except four

Figure A.4: A comparison of missing mass for events with four tracks (identified either as electrons or electrons and pions, left) and events with any number of tracks except four (right). The disagreement between offpeak data (dots) and continuum Monte Carlo (solid histogram) exists in the four-track events.

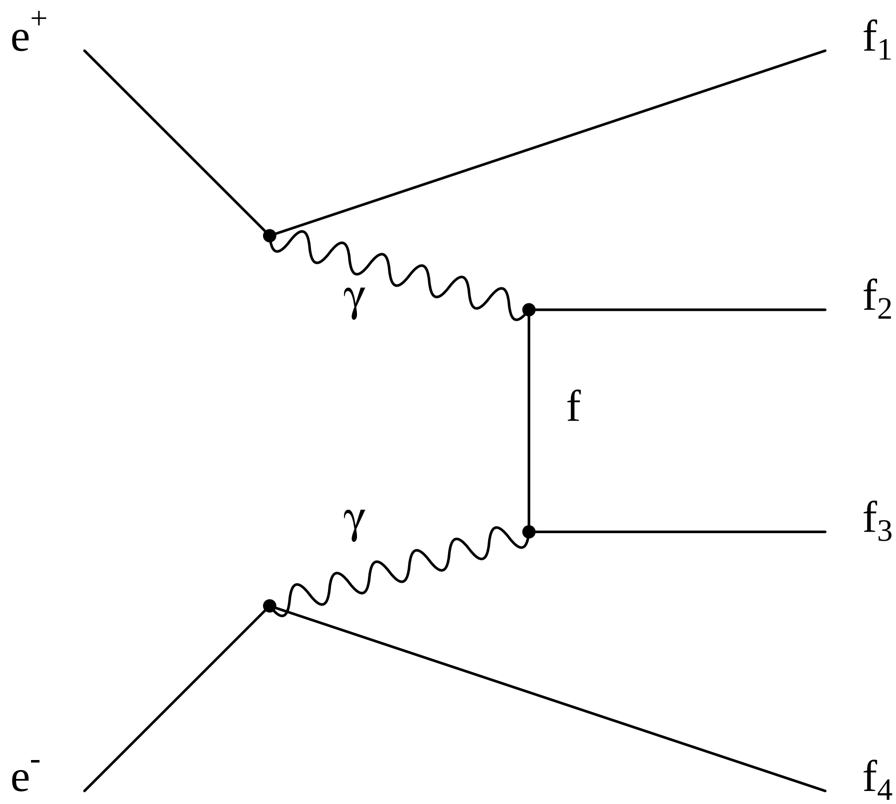

Figure A.5: One of many Feynman diagrams representing four-fermion processes. This is one example of how to produce these final states at an electron-positron collider, through the intermediate exchange and conversion of photons.

Appendix B

Study of the Data/MC Disagreement in E_{extra} for $p^*_{signal} > 1.2\,\mathrm{GeV/c}$

As discussed in Section 5.4.2, there is a disagreement between data and simulation in the shape of the E_{extra} distribution for $p^* > 1.2\,\mathrm{GeV/c}$. The data in this region should be highly incompatible with signal events. This appendix details the studies which were performed in an attempt to understand the disagreement. While its source is not clear, it appears to have a correlation with the momentum of the tau's lepton daugter in the center-of-mass frame (p^*_ℓ).

Figure B.1 shows the neutral energy distribution for $p^* > 1.2\,\mathrm{GeV/c}$. Of immediate note is the apparent (though not highly significant) disagreement between the data (black dots) and the simulation (stacked histogram) at 0.2 GeV, a region where signal events are expected to populate. Otherwise, the agreement appears to be quite good between the distributions.

Upon closer inspection of this distribution, the disagreement at 0.2 GeV appeared to be less consistent with signal than with a background which was not

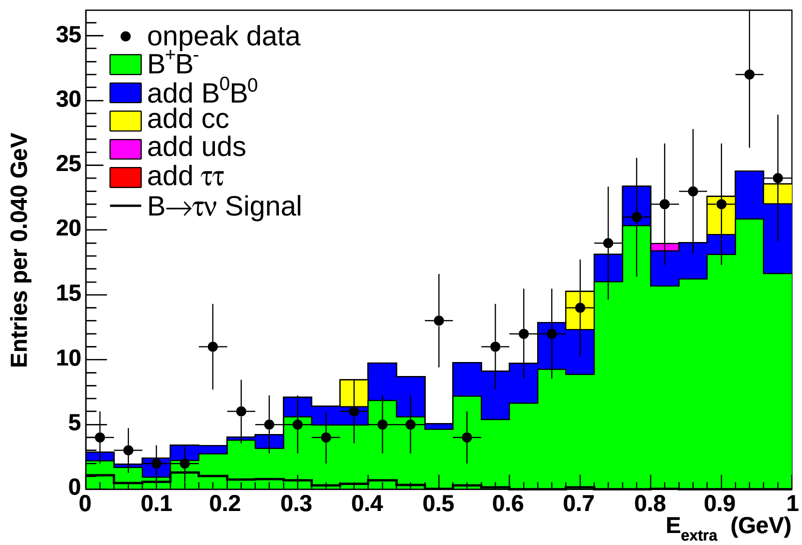

Figure B.1: The extra neutral energy for high signal track momentum ($p^*_{signal} > 1.2\,\mathrm{GeV/c}$).

simulated in the Monte Carlo. In particular, plotting the neutral energy for events with $p^*_\ell > 1.2\,\mathrm{GeV}/c$ (background-like) and $p^*_\ell < 1.2\,\mathrm{GeV}/c$ (signal-like) reveals that about 70% of the peak region ($0.15 < E_{extra} < 0.25\,\mathrm{GeV}$) lies above 1.2 GeV while only 35% of the signal (dominantly electrons) lies above 1.2 GeV.

B.1 Studying the Events in the Peak at 0.2 GeV

Several studies were performed to illuminate the potential source or sources of events which may pile at 0.2 GeV. These included:

- Studying detector/data effects, such as clustering in the calorimeter or in time (run number).
- Studying specific known contributions to the background to determing if

any collect specifically at 0.2 GeV (for instance, by depositing a photon or π^0 with a specific energy).

- Studying the events using the WIRED event display [1] in an attempt to identify interesting features.

B.1.1 Searching for Detector Effects

To study whether or not these events are consistent with a detector effect (such as a region in the EMT which is repeatedly triggering due to and EMC data acquisition problem), the events in the peak region for $p^*_\ell > 1.2\,\mathrm{GeV}/c$ are plotted as a function of run number and theta and phi in the calorimeter. Figures B.2-B.3 show the distributions of these variables for these events. No obvious clustering occurs, either as a function of time or position in the calorimeter.

In addition to looking for very specific effects in the EMC, an attempt was also made to artificially over-kill photons from π^0 decay, for π^0s from D^{*0}, ρ^0 and B decay. As a first test, one out of every two truth-matched photons from π^0 decay from these decays were killed, just to see if a peak could be made to appear in the Monte Carlo. Figure B.4 shows the distribution of the neutral energy before and after performing this killing procedure. No peak appears in the distribution.

Finally, an attempt is made to determine if the disagreement is due to a flaw inherent in the *BABAR* software used to reconstruct the event information. *BABAR* does systematic updates of its core analysis software. Updates are indi-

[1] http://www.slac.stanford.edu/BFROOT/www/Computing/Graphics/Wired/index.html

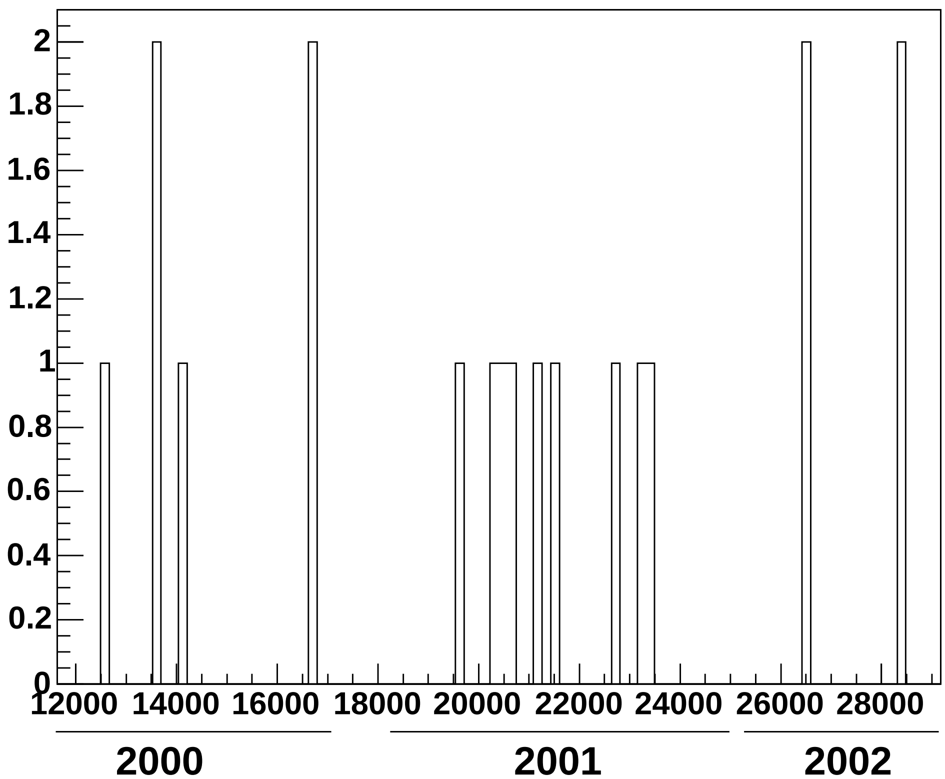

Figure B.2: The events in the peak at 0.2 GeV in E_{extra} as a function of run number. The horizontal lines under the x-axis indicates the time periods occupied by data run periods.

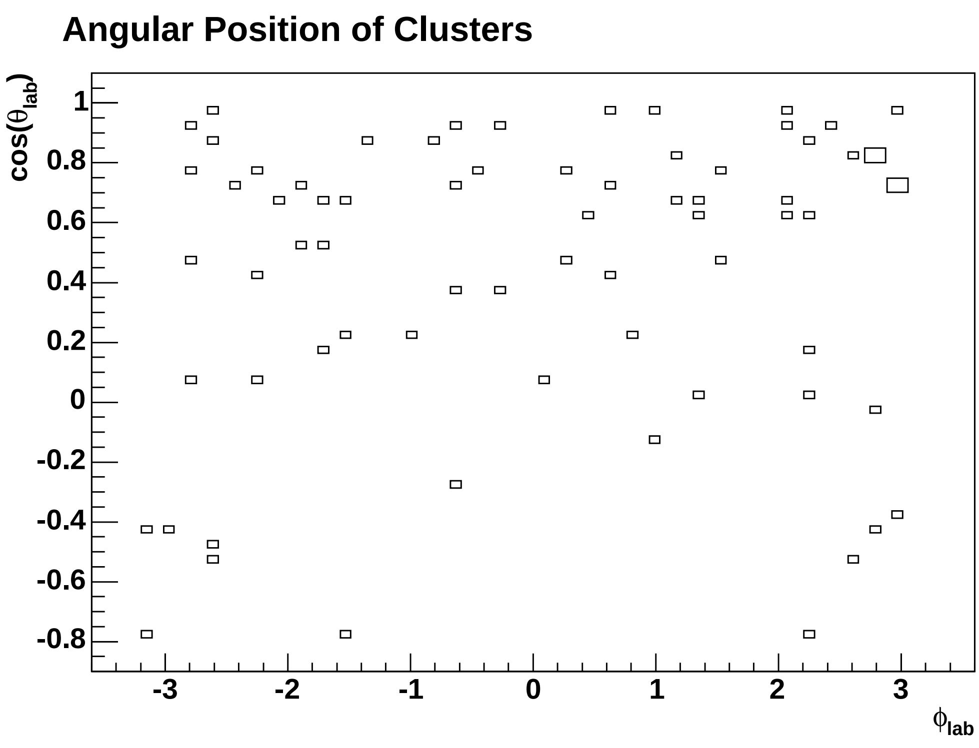

Figure B.3: The events in the peak at 0.2 GeV in E_{extra} as a function of EMC θ and ϕ.

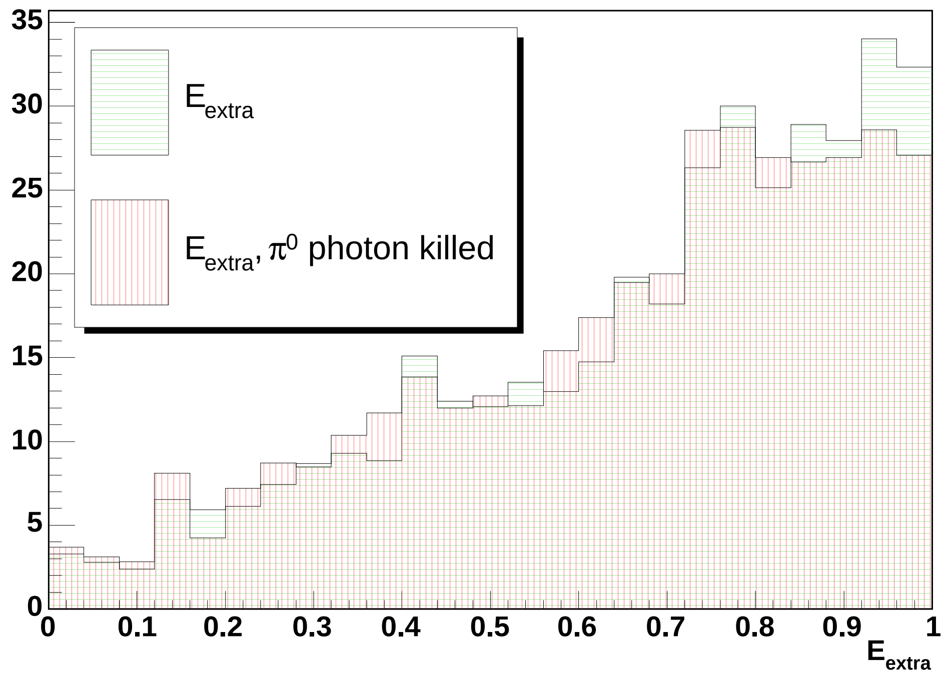

Figure B.4: The neutral energy distribution in the MC before and after killing one out of every two truth-matched photons from π^0s from D^{*0}, ρ^0 and B decay.

cated by a series of numbers, such as 10.0.0, which indicates, in order, a major change to the software (10), a minor change to the software (0), and a bugfix (0). Coupled to these updates (releases) *BABAR* reprocesses all of its data and Monte Carlo simulations. This is done to take advantage of significant improvements in tracking, etc. The software release used to generate all results in the present work is the 10.X series. At the time of the writing of this thesis, *BABAR*'s recommended stable release is the 12.X series.

In an attempt to see if the peak is connected to the `10.X` software series processing of the data the events that pass all cuts in the data are processed in the `12.X`. Figure B.5 shows the comparison between the data as processed with 10.X and 12.X series software. While many events that originally passes the selection no longer pass, most of the peak events survive. In addition, the peak structure is left intact. This suggests that the peak is not an artifact of the features of the 10.X series processing.

B.1.2 Study of Specific Background Channels

The dominant background source for this analysis is any process which produces a real lepton and missing energy, either in the form of lost charged particles or long-lived neutrals (in particular, K_L^0). The most dominant physical process producing backgrounds is the transition $b \to c\ell\nu$. The next most dominant transition is $b \to u\ell\nu$. Since many *BABAR* analyses study these specific transitions (either exclusively or inclusively), there are large samples of avsailable MC for investigating these backgrounds.

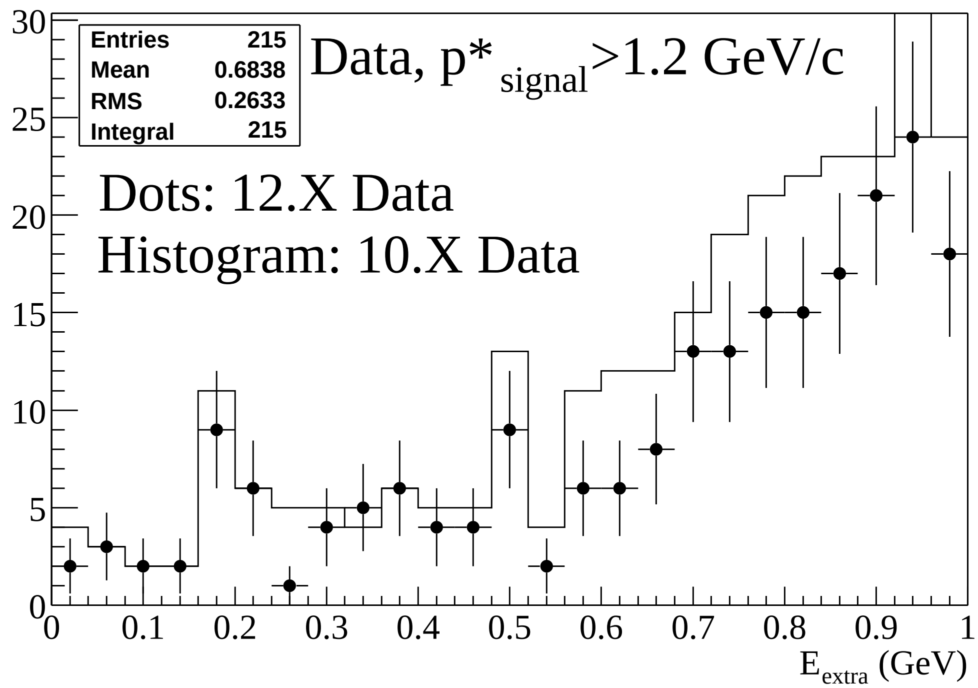

Figure B.5: The neutral energy distribution in the data, processed with 10.X series software (current analysis) and processes with 12.X series software.

A list of modes which were processed using `BToDlnuXUser` and then all selection criteria are listed below. All available SP4 events in each mode were processed and the neutral energy distribution studied. The primary obstacle encountered in this study is the sheer rejection efficiency which the cuts in the analysis yield. In most cases, few or no events passes all the selection cuts. In the discussion that follows, only modes that produced at least 10 raw events (which can then be scaled by selection efficiency and PDG branching fraction to obtain yields in $81.9\,\mathrm{fb}^{-1}$ of data) are discussed. In general, there is no single process (or any combination of processes) which yields a discernable peak at $0.2\,\mathrm{GeV}$ in the MC.

```
Species                       Year          # Gen.          # Passing
(Mode Number)
------------------------------------------------------------------

B0->X,B0->D*+lnu              2000          4000            0
(982)                         2001          36000           2
                              2002          12000           0


B0->X,B0->D*+lnu,D0->KPi      2000          0
(1122)                        2001          68000           2
                              2002          80000           5


B0->X,B0->D*+lnu              2000          1022000         19
(phase space only)            2001          1174000         24
```

(4104)	2002	352000	6
B+->X,B- -> D10lnu	2000	0	
(3141)	2001	0	
	2002	20000	0
B+->X,B- -> D20lnu,D20->D*0	2000	0	
(3143)	2001	16000	0
	2002	21000	0
B+->X,B- -> D20*lnu	2000	0	
(1638)	2001	21000	0
	2002	21000	0
B+->X,B->D*0lnu(D0->K3Pi)	2000	0	
(1324)	2001	20000	1
	2002	21000	1
B+->X,B->D*0lnu(D0->KPi)	2000	0	
(1322)	2001	82000	10
	2002	76000	4

B+->X,B->D*0lnu(D0->KPiPi0)	2000	0	
(1323)	2001	37000	3
	2002	19000	0
B+->X,B- -> omegalnu	2000	88000	7
(3079)	2001	144000	6
	2002	60000	4
B+->X,B- -> pi0 lnu	2000	132000	39
(3498)	2001	168000	52
	2002	100000	25
B+->X,B- -> rho0 lnu	2000	86000	1
(3077)	2001	144000	3
	2002	60000	0

None of the above modes yields an E_{extra} distribution which is consistent with a significant peak at 0.2 GeV. However, in almost all cases the statistics available to study the E_{extra} distribution for a particular mode are limited. In the case of $B^- \to \pi^0 \ell \nu$, although many tens of events pass the branching fraction is so small ($0.018\% \pm 0.006\%$) that these events scale down to a handful (~ 3 events). These few events are not enough to create the peak seen in the data.

In the case of the $c\ell\nu$ transitions, the branching fractions are typically so large (i.e. $D^{*+}\ell\nu$) that these specific samples yield far fewer events than the MC used throughout the present work to compare to data.

The results of this study are inconclusive. Although the samples listed above represent hundreds of total hours of Monte Carlo generation, there was simply insufficient available Monte Carlo events to determine whether any one was responsible for the peak in data. Summing them together also did not produce enough data to make this determination.

B.1.3 WIRED Study of the Peak Events

The WIRED event display has been used to look at the data events that fall in the peak region. This section will discuss the observations made during this study. One important qualificatio needs to be made immediately: no criteria have ever been developed to scan events by by using WIRED. The observations noted below are merely those of one of the author.

The events studied live in the neutral energy peak in data ($0.15 < E_{extra} < 0.25$) and have a signal track momentum (in the center-of-mass frame) greater than 1.2 GeV/c. The events are listed in Table B.1 according to *BABAR* timestamp and run number.

After scanning the events in WIRED, the following conclusions are drawn. Of the 19 events, five appear to have a pattern of hits in the DCH consistent with a track. However, no track has been fit to these hits, suggesting the progentior of the hits was a low momentum charged particle (less than 150 MeV/c of transverse momentum). Six events appear to have activity in the IFR which is not associated

Table B.1: The timestamps and run numbers of the events lying in the region of data/MC disagreement in E_{extra} for $p^*_{signal} > 1.2\,\mathrm{GeV/c}$.

Event	Timestamp	Run Number
1	193c04/5264fcd7	16645
2	194de3/1656818f	16762
3	159583/32d543f	12522
4	16b714/47b879c3	13526
5	16bb71/92c57aaf	13548
6	174681/7297daa7	14200
7	1ca7e2/27dd6c43	19665
8	1d4df5/b5d48063	20378
9	1d5772/9f6c912f	20417
10	1d8e48/fb82736f	20648
11	1df867/52334c07	21100
12	1f8213/a3cc481b	22770
13	1e62da/7b6f48f3	21530
14	1fde09/116ebccf	23188
15	1ff7ef/7a0d5633	23326
16	23d15a/dfdf3c73	28333
17	23d76d/79e77c7b	28355
18	2256ea/74c01cdf	26468
19	226d25/64adfd37	26566

with any charged track, suggesting there could be K_L^0s in the event. One of the six events also has an unreconstructed track (is one of the aforementioned five events). Finally, nine of the 19 events have no distinctive features and appear to meet the selection criteria in this analysis flawlessly.

The above results do not point to one particular culprit. The five events with unreconstructed tracks could be mis-reconstructed $e^+e^- \to B^0\overline{B}^0$ events, but no obvious culprit modes were identified in the previous section.

B.2 Current Conclusions

There is currently no definitive explanation for the events in these peak. They appear to be inconsistent with signal events. However, there is no single piece of evidence which points to a background which can explain the peak. This feature, while it appears to live dominantly above 1.2 GeV/c in signal-track momentum, may tail into the lower momentum region if due to a physical background with a momentum spectrum. This feature must be studied more carefully using the latest *BABAR* MC samples which are meant to parallel data taken in 2003 and beyond.